Focused Ultrasound-Induced Cavitation Renders Cancer Cells Susceptible to Radiation Therapy, Hyperthermia and Testosterone Treatment

Dissertation

zur Erlangung des akademischen Grades

Dr. rer. med.

an der Medizinischen Fakultät

der Universität Leipzig

eingereicht von: M.Sc. Shaonan Hu

Geburtsdatum / Geburtsort: 01.01.1988 / Shanxi, China

angefertigt an Innovationszentrum für Computer-assistierte Chirurgie (ICCAS) an der Medizinischen Fakultät der Universität Leipzig

Betreuer: Prof. Dr. Andreas Melzer

Beschluss über die Verleihung des Doktorgrads vom: 22.02.2022

TABLE OF CONTENTS

TABLE OF CONTENTS

TABLE OF CONTENTS

TABLE OF CONTENTS

1 Abbreviations

AR	Androgen receptor
ARA-70	Androgen receptor-associated protein 70
AR-DHT	Androgen receptor-dihydrotestosterone complex
ARE	Androgen response element
AR-T	Androgen receptor-testosterone complex
c	The speed of sound in the medium
CREB	Cyclic adenosine monophosphate response element-binding protein
CBP	CREB-binding protein
Cdk	Cyclin-dependent kinase
bNED	Median no evidence of disease
CO_2	Carbon dioxide
CRPC	Castration-resistant prostate cancer
Cyto-c	Cytochrome c
DAPI	4′,6-diamidino-2-phenylindole
DHT	Dihydrotestosterone
DMEM	Dulbecco's Modified Eagle Medium
DMSO	Dimethyl sulfoxide
DNA	Deoxyribonucleic acid
ECACC	European Collection of Authenticated Cell Cultures
EDTA	Ethylenediaminetetraacetic acid
e.g.	exempli gratia (for example)
EHS	Engelbreth-holm-swarm
ESR	Electron-spin-resonance
et al.	et alia (and others)
EU	European Union
f	Frequency of applied transducer
f_0	Fundamental frequency

Abbreviations

FBS	Fetal bovine serum
FDA	Food and Drug Administration
FFT	Fast Fourier transformation
FOH	Fiber-optic hydrophone
FSC	Forward-scattered light
FUS	Focused ultrasound
FUS-Cav	FUS shot with cavitation
× g	gravitation
h	hour
HCL	Hydrochloric acid
HEPES	4-(2-Hydroxyethyl)-piperazine-1-ethanesulfonic acid
HIFU	High-intensity focused ultrasound
hsp	Heat shock protein
HT	Hyperthermia
HTA	2-hydroxyterephthalic acid
I	Time-varying acoustic intensity
i.e.	id est (in other words)
ICCAS	Innovation Center Computer Assisted Surgery
IMSaT	Institute for Medical Science and Technology
I_{TP}	Temporal-peak acoustic intensity
MBs	Microbubbles
MEM	Minimum Essential Medium
M (f)	Frequency response of the FOH
min	minute
MI	Mechanical index
MMPs	Matrix metalloproteinases
MMP-2	Matrix metalloproteinase 2
MMP-9	Matrix metalloproteinase 9
MR	Magnetic resonance

Abbreviations

MR-ARFI	Magnetic resonance acoustic radiation force impulse imaging
MRE	Magnetic resonance elastography
MRgFUS	Magnetic resonance-guided focused ultrasound
MRI	Magnetic resonance imaging
mRNA	Messenger ribonucleic acid
MS/s	Mega-samples per second
NaOH	Sodium hydroxide
NY	New York
·OH	Hydroxyl radical
OS	Overall survival
p	Time-varying acoustic pressure
P	Phosphorylation
PARP	Polyadenosine diphosphate ribose polymerase
PBS	Phosphate-buffered saline
PCD	Passive cavitation detection
PCI	Passive cavitation imaging
PE	Plating efficiency
Pen-strep	Penicillin and streptomycin
PI	Propidium iodide
PI3K/AKT	Phosphatidylinositol-3-kinase/serine-threonine kinase
PNP	Temporal-peak negative pressure
PRF	Proton resonance frequency
PSA	Prostate-specific antigen
RMS	Root mean square
RMS voltage$_t$	Cavitation level of one sonication segment for 1.6 ms
RT	Radiation therapy
SD	Standard deviation
SEM	Standard error of the mean
SF	Survival fraction

Abbreviations

SP-1	Specificity protein 1
SRC-1	Steroid receptor co-activator 1
SRD5A	5α-reductase
SRD5A1	5α-reductase type I
SRD5A2	5α-reductase type II
SRD5A3	5α-reductase type III
SSC	Side-scattered light
t	Time for each sonication segment (1.6 ms)
T	Testosterone
T	One period of sonication duration (2.9 s)
TA	Terephthalic acid
UK	United Kingdom
US-ARFI	Ultrasound acoustic radiation force impulse imaging
USgFUS	Ultrasound-guided focused ultrasound
USA	The United States of America
V	Measured voltage with the hydrophone
Vpp	Peak-to-peak output voltage
WST-1	Tetrazolium salt
ρ	The density of the acoustic medium

2 Summary

Focused ultrasound (FUS) is a less-invasive medical technique with the potential to improve the treatment outcome of many diseases by utilizing acoustic transducers to generate and concentrate the multiple intersecting ultrasonic waves on a targeted site in the body. The bio-effects induced by FUS are mostly classified into thermal and mechanical effects (mainly focus on cavitation effect). Cavitation is capable of disrupting tumor vasculature and cell membranes. Numerous studies reported that cavitation-induced sonoporation could provoke multiple anti-proliferative effects on cancer cells, including cell-cycle arrest, cell apoptosis, and clonogenicity suppression. Therefore, the combination of FUS-induced cavitation and other treatment modalities like radiation therapy is of great interest, but research in this field is inadequate.

A special high-throughput FUS system was used for cancer cell treatment with a customized 1.467 MHz single focused transducer. Characterization of acoustic behavior of gas-filled cavities was performed via a fiber-optic hydrophone (FOH) system and chemical terephthalic acid method helped to define the acoustic parameters, which could lead to occurrence of cavitation at the bottom of 96-well cell culture plates where cancer cells were located. Cavitation occurs at and above the acoustic intensity of 344 W/ cm^2 for the 1.467 MHz transducer. The short- and long-term effects of FUS-induced cavitation and adjuvant effects to radiation therapy, standard hyperthermia and testosterone treatment (only for prostate cancer) were investigated comprehensively at the cellular and molecular levels in human prostate cancer (PC-3 and LNCap), glioblastoma (T98G) and head and neck (FaDu) cells *in vitro*.

The long-term additive effects of short FUS shots (with or without cavitation) to radiation therapy (RT) or hyperthermia (HT) were displayed by significantly reduced clonogenic survival in PC-3, T98G and FaDu cells compared to single treatments. The combination treatment of short FUS with cavitation (FUS-Cav) and RT led to a comparable radio-sensitization effect to HT at 45 °C for 30 min and showed a significant reduction in treatment duration, especially for PC-3 cells. The short-term additive effects of short FUS shots to RT or HT are manifested in reducing the potential of cells to invade and decreased metabolic activity. The induction of sonoporation by FUS-Cav was supposed to be the mechanism of cancer cell sensitization to other therapies at the cellular level. The dramatic decline of 5α-reductase type III (SRD5A3) level induced by combination treatment with FUS-Cav and HT is presumed as the underlying mechanism of additive effects of FUS-Cav to HT at the molecular level.

Besides, testosterone solutions with normal physiological levels were discovered to inhibit the long-term metabolic activity of androgen-dependent prostate cancer cells LNCap *in vitro*, while short FUS shots displayed a long-term additive effect to the testosterone treatment. The presented multilevel study demonstrates that short FUS shots using FUS-induced cavitation carry the potential to sensitize cancer cells to other cancer treatment modalities precisely and less-invasively, providing a promising adjuvant therapy to cancer treatments in the future.

3 Introduction

As a part of the male reproductive system, the prostate is located directly below the bladder and in front of the rectum. The urethra connecting with bladder and seminal vesicle is throughout the center of prostate gland (Figure 1). Almost all prostate cancer primarily originates from the prostate gland cells (i.e. the cells secreting the alkaline fluid), which is named as adenocarcinoma. Other types of cancer that originate from prostate are rare, including sarcomas, transitional cell carcinomas, small cell carcinomas and neuroendocrine tumors.

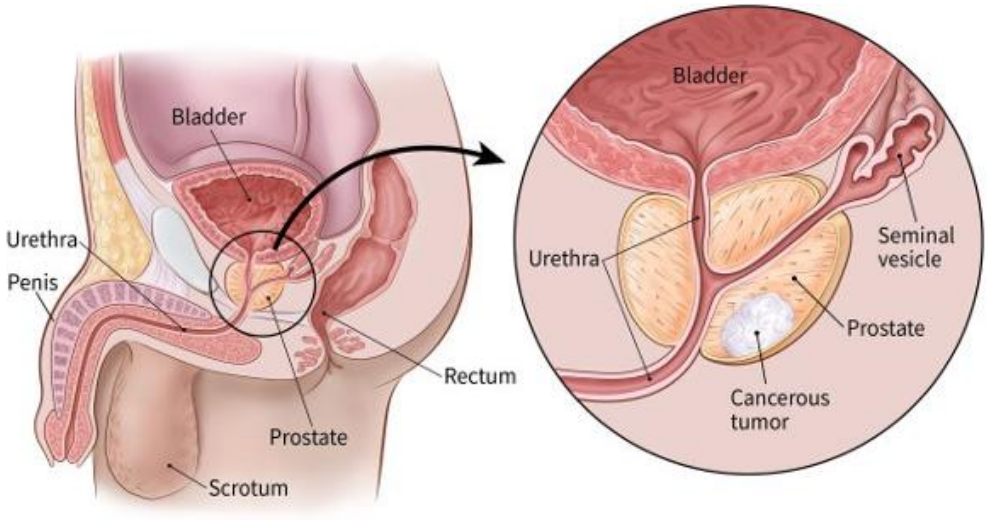

Figure 1: Schematic for the prostate gland anatomy. The prostate is located in front of the rectum, below the bladder and seminal vesicle. The urethra connecting with the bladder and seminal vesicle is throughout the whole prostate gland. Adapted from American Cancer Society (https://www.cancer.org/cancer/prostate-cancer/about/what-is-prostate-cancer.html).

Prostate cancer is the second most common cancer occurring in men. Approximately 1,270,000 new cases were diagnosed worldwide in 2018 (Rawla, 2019). The incidence rate of prostate cancer varies across regions and populations (Figure 2). Age, race and family inheritance are the primary factors in the morbidity and mortality of prostate cancer. Due to differences in environmental, social, and genetic factors, an increasing trend of prostate cancer incidence is estimated, with more than two million new cases in the world until 2040 (Rawla, 2019). Most early-stage prostate cancers present as asymptomatic, which require only active surveillance and will not harm patients as quickly as other cancers like pancreatic cancer and esophageal cancer (Rawla, 2019). When prostate cancer cells become aggressive and break away from the

prostate tumor, metastatic prostate cancer occurs. In theory, prostate cancer cells can travel to any other body area via the lymphatic system or blood flow. In most cases, the destination of prostate cancer metastasis is the lymph nodes or bones, and it can also metastasize to the lungs, liver or brain (Guo et al., 2018). The treatment of prostate cancer is currently facing enormous challenges because when it progresses into the metastatic type, the metastatic prostate cancer becomes incurable even if it is identified promptly, which is the leading reason for death from prostate cancer. So the development of new strategies to inhibit the prostate cancer cells' potential to invade and improve less-invasive treatment outcomes of patients with metastatic disease are the grand challenges in prostate cancer (Crea et al., 2014; Gorchakov, Kulemzin, Kochneva, & Taranin, 2020).

As a primary less-invasive treatment for local prostate cancer, radiation therapy has the limitations of radiation resistance generated on cancer cells and the complications caused by high radiation doses (Murray & Tree, 2019). The cavitation induced by ultrasound is usually used for the targeted delivery of therapeutic molecules due to its enhancement effects on the vasculature and cell membrane permeability (Y. Wang et al., 2013; Zolochevska et al., 2011). Furthermore, several studies reported anti-proliferative effects on cancer cells (e.g. cell apoptosis, cell-cycle arrest and clonogenicity suppression) caused by cavitation-induced sonoporation (X. Chen et al., 2013; Karshafian et al., 2010; D. L. Miller & Dou, 2009; Zhong et al., 2011), making it be a potential less-invasive adjuvant therapy to sensitize cancer cells to other treatment modalities. Accordingly, the combination of FUS-induced cavitation and other treatment modalities is an attractive direction to improve the therapeutic outcome and minimize adverse effects for the current prostate cancer treatment.

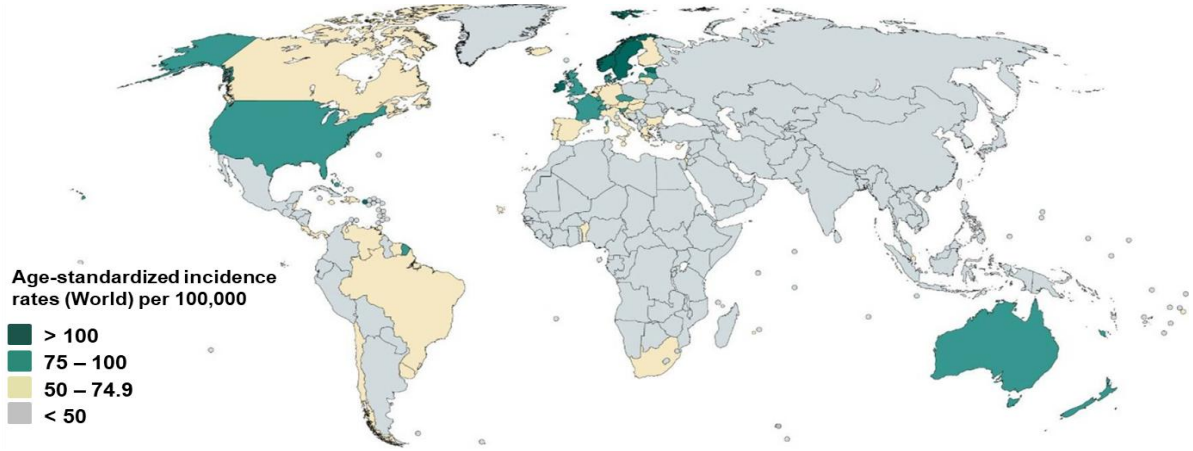

Figure 2: Statistics of prostate cancer morbidity worldwide in 2018. The incidence of prostate cancer

varies considerably worldwide. The highest age-standardized incidence (ASR) was in Oceania (79.1 years per 100,000 people) and North America (73.7), followed by Europe (62.1). However, developing countries in Africa and Asia had low ASRs (26.6 and 11.5, respectively). Adapted from (Rawla, 2019).

4 Medical and technical background

4.1 The biological basis of prostate cancer treatment

4.1.1 Androgen receptor: an essential signaling pathway for progression of prostate cancer

The androgen receptor (AR) signaling pathway plays a unique role in the development, functionality, and homeostasis of the prostate (Lonergan & Tindall, 2011). The conventional functions of the AR signaling pathway include modulation of lipid and protein biosynthesis and coordination of cell division, differentiation, proliferation and apoptosis (Meehan & Sadar, 2003). Both testosterone (T) and dihydrotestosterone (DHT) can bind to the AR to activate the AR signaling pathway. The dissociation rate of the AR-DHT complex is much lower than the AR-T complex. Therefore, DHT is regarded as the primary ligand for binding with the AR due to the more stable AR-DHT complex (Y. Wu et al., 2013). The binding of DHT to the AR promotes the dissociation of heat-shock proteins, and thereafter the AR-DHT complex is transferred into the cell nucleus to bind with androgen response elements and more other complex response elements (Figure 3). By this time, the AR is trans-activated by the co-activators located on the deoxyribonucleic acid (DNA) to modulate the transcription and expression of corresponding genes. Using various techniques, 146 to 517 genes and 44 proteins regulated by AR signaling pathway have been detected in human prostate cancer cells (Meehan & Sadar, 2003). The AR signaling pathway is crucial to the initiation and development of prostate cancer. Maintaining of AR protein and activation of AR signaling pathway are in every stage of prostate cancer, even after androgen deprivation therapy (Y. Wu et al., 2013).

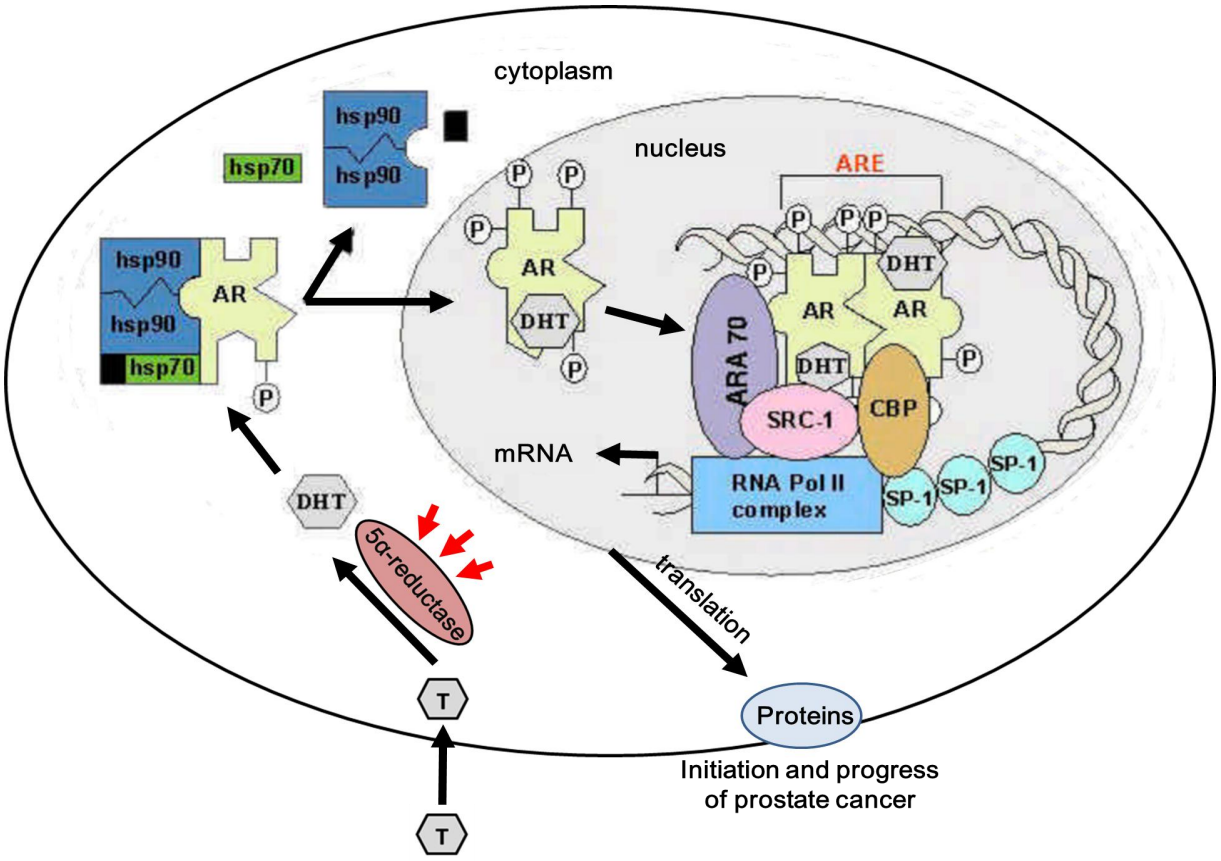

Figure 3: Schema for the illustration of the AR signaling pathway. Testosterone is converted to DHT by the catalyzation of intracellular 5α-reductase (highlight with red arrows). DHT as a primary ligand binds with AR to form AR-DHT complex, promoting the dissociation of heat-shock proteins. Afterwards, the AR-DHT complex is transferred to the cell nucleus and binds with androgen response elements and more other response elements located on DNA to modulate the transcription and expression of corresponding genes. T: testosterone, DHT: dihydrotestosterone, AR: androgen receptor, hsp: heat shock protein, P: phosphorylation, ARE: androgen response element, CBP: CREB binding protein, CREB: Cyclic adenosine monophosphate response element-binding protein, ARA-70: androgen receptor-associated protein 70, SRC-1: steroid receptor co-activator 1, SP-1: specificity protein 1. Adapted from (Meehan & Sadar, 2003).

4.1.2 5α-reductase: a promising therapeutic target for prostate cancer therapy

As mentioned above, the AR signaling pathway is indispensable for normal prostate development and function but also crucial for the initiation and progression of prostate cancer. DHT is responsible for activating the AR and generated from testosterone (T) by the enzyme 5α-reductase (SRD5A) (highlight with red arrows in Figure 3), playing a vital role in the AR signaling pathway (J. Li et al., 2011). Three isozymes of 5α-reductase have been identified inside the human body till now. Type I 5α-reductase (SRD5A1) predominantly functions in the growth and differentiation of skin and liver, while type II

(SRD5A2) is primarily expressed in the prostate (W. Chen et al., 1998; Thigpen et al., 1993). Type III (SRD5A3) is the novel type reported in 2008, which was discovered to be correlated with DHT generation and AR activation in castration-resistant prostate cancer (CRPC) cells. Immunofluorescence is a widely used technique (the principle is shown in Figure 4) to visualize the distribution of SRD5A in cytoplasm, and quantify the SRD5A level via flow cytometry.

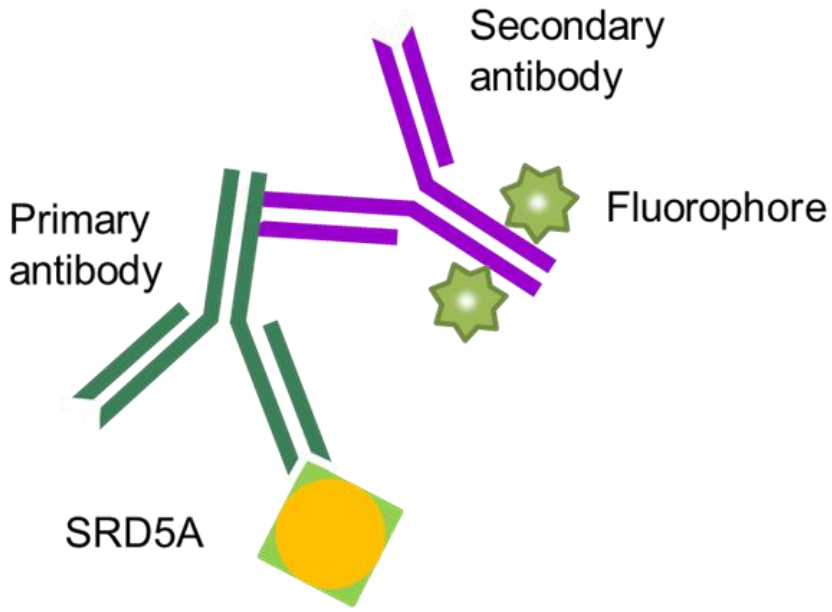

Figure 4: Schematic drawing to illustrate the principle of immunofluorescence. The primary antibody binds specifically to the SRD5A proteins. A secondary fluorophore-coupled antibody, specifically binds to the primary antibody, is used to visualize the distribution of SRD5A proteins. Adapted from (https://ibidi.com/content/364-the-principle-of-immunofluorescence-assays).

Suppression of the enzymatic activity of SRD5A was reported to be a promising alternative for CRPC therapy (Uemura et al., 2008). To delineate the separate roles of SRD5A1, SRD5A2 and SRD5A3, Jin L et al. (J. Li et al., 2009) examined their mRNA levels in prostate tissue samples from men with benign prostate hypertrophy, prostate cancer and no prostate disease. The results showed that SRD5A2 was the predominant form of 5α-reductase in healthy prostate and benign prostate diseases. SRD5A1 and SRD5A3 were the primary isozymes in the prostate cancer cells. Goldenberg et al. (Goldenberg et al., 2009) reported that the suppression of SRD5A might exhibit great benefit in the reduction of prostate cancer morbidity and CRPC therapy. The immunostaining of SRD5A3 is generally presented in malignant prostate tissues while relatively infrequent in benign tissues, suggesting that SRD5A3 is a potential biomarker of malignant prostate tumors (Godoy et al., 2011). Azuma et al. (Azuma, Matayoshi, Sato, & Nagase, 2018)

assessed the effectiveness of dutasteride, the inhibitor of SRD5A, in the CRPC treatment. The decrease of the prostate-specific antigen (PSA) in 41 % of patients following treatment indicated that the suppression of SRD5A with dutasteride was efficacious against CRPC in individual patients, suggesting that targeting the SRD5A protein might be a promising option in CRPC treatment (Azuma, Matayoshi, Sato, & Nagase, 2018). However, in the report of Hirshburg et al. (Hirshburg, Kelsey, Therrien, Gavino, & Reichenberg, 2016), SRD5A inhibitors (i.e. dutasteride or finasteride) could induce depression and sexual dysfunction including decreased libido and erectile dysfunction, and even increase the possibility of high-grade cancer. To sum up, SRD5A is an important gatekeeper for the activation of the AR signaling pathway and needs to be investigated in novel prostate cancer treatment strategies.

4.1.3 Testosterone: duality effects in prostate cancer development

Testosterone is the primary male sex hormone in the body regulating the formation of male secondary sexual characteristics (including beard, body hair, prominentia laryngea, muscle and sperm). Testosterone activates the AR signaling pathway after being converted to DHT by 5α-reductase catalyzing, which is essential for the growth and development of the prostate (Figure 3). Testosterone is also discussed to be responsible for initiation and development of prostate cancer, thus limiting the number of testosterone in the body is one strategy in the treatment of prostate cancer. The reduction of testosterone concentration in testicles using surgery or drugs (i.e. castration) is named androgen deprivation therapy. In the 1940s, androgen deprivation therapy was reported by Huggins and Hodges for the first time to suppress metastatic prostate cancer (Huggins & Hodges, 1941). Some *in vitro* studies proposed the androgen hypothesis that high testosterone concentration might raise prostate cancer morbidity, whereas low testosterone concentration was protective (Michaud, Billups, & Partin, 2015). Over the past decades, researchers have reviewed the correlation between serum testosterone concentration and cancer progression in diagnosis and clinical therapy outcomes. In the study of Hashimoto et al. (Hashimoto et al., 2019), AR targeted therapy was more efficient for patients with a serum testosterone concentration ≥ 50 ng/L compared to patients with serum concentration < 50 ng/L. Serum testosterone level was considered as a useful biomarker of aggressive prostate cancer (Barqawi & Crawford, 2006), and it could provide a basis for the selection of AR targeted treatment. However, due to the conflicting study of design, definitions and methodologies, the role of serum testosterone level was controversially discussed in the diagnosis and treatment of prostate

cancer (Klap, Schmid, & Loughlin, 2015). The fundamental and clinical research in recent years has allowed people to realize the complexity and duality of testosterone in prostate cancer development. Several *in vitro* studies demonstrated that the development of prostate cancer cells required only low testosterone levels, and extremely low levels of testosterone resulted in the slow growth of prostate cancer cells. However, the proliferation of prostate cancer cells was hindered at the normal physiological level of male testosterone (Song & Khera, 2014). In clinical practice, some researchers found that testosterone replacement therapy never enhanced prostate cancer risk, it even reduced the risk of highly aggressive prostate cancer (Barqawi & Crawford, 2006). There were studies demonstrating that men with lower testosterone levels (e.g. older people) had a higher risk of getting prostate cancer and more aggressive prostate cancer (Hoffman, DeWolf, & Morgentaler, 2000). Several papers also suggested that testosterone might benefit prostate cancer by developing a less aggressive phenotype (Lane, Stephenson, Magi-Galluzzi, Lakin, & Klein, 2008). Research about the effects of treatment with various testosterone levels is essential to identify the duality effects of testosterone promoting or suppressing prostate cancer initiation and development.

4.2 Advantages and disadvantages of current clinical treatments of prostate cancer

Recent studies have made significant headway in the characterization of disease risks and the development of treatment options. Regarding the clinical treatments of prostate cancer, they can be divided into i) local treatments and ii) systemic treatments. Local treatments, including radical prostatectomy, radiation therapy, cryotherapy, and HIFU ablation, mainly target localized prostate cancer without metastasis, whereas systemic treatment (hormone therapy, chemotherapy, and immunotherapy) targets metastatic prostate cancer (Pignot et al., 2018). Table 1 demonstrates the characteristics, advantages and disadvantages of above clinical treatments of prostate cancer. The risk stratification of cancer patients is improved with the advancement of diagnosis and treatment, and clinicians are allowed to formulate therapy options based on cancer progression and preference of patients. For instance, age is an essential factor to be considered in the selection of prostate cancer therapy compared with other cancers. The clinicians need to balance the influence of treatment on life quality along with cancer control. In this context, surgery is recommended for young men, and radiation therapy is more suitable for older people due to no hospitalization and less-invasiveness (Krasnow et al., 2018).

Table 1: Characteristics of current clinical treatment for different stages of prostate cancer

Treatment option	Applicability	Advantages	Disadvantages	Reference
Radical prostatectomy	Localized early prostate cancer	High eradication probability Low treatment cost Ease of recurrence detection	Invasive therapy Possible bleeding or infection in surgery The complications such as urinary incontinence and sexual dysfunction	(Bianco, Scardino, & Eastham, 2005; Engel et al., 2010; Punnen et al., 2013)
Radiation therapy	Localized prostate cancer	Less-invasive therapy; Ease for long-term disease control High safety and efficiency Applicable for combination with radical prostatectomy or hormone therapy	Radio-resistance induced failure of radiation therapy High radiation dose induced adverse effects such as incontinence and bowel problems	(Murray & Tree, 2019)
High-intensity focused ultrasound	Small, localized prostate tumors	Less-invasive therapy Precise target on tumors with MRI with minimized harm on surrounding tissues Very low rate of complications Allows repeated procedure	Not feasible for all localized prostate tumors (e.g. massive or multiple tumors) Ultrasonic energy loss due to the absorption by other organs/tissues	(Aus, 2006; van Velthoven et al., 2016)
Cryotherapy	Localized prostate cancer	Minimally invasive A short treatment course Fast recovery Minimal anesthesia Fewer adverse effects and low cost	May affect neighbor healthy tissue Adverse effects such as incontinence and other urinary or bowel problems	(Aus, 2006; Petrova, Brecht, Motamedi, Oraevsky, & Ermilov, 2018)
Hormone therapy	Locally advanced or metastatic prostate cancer	Lower toxicity High therapeutic response Applicable for combination with radiation therapy or radical prostatectomy	Possible bleeding or infection in surgery Potential adverse effects including heart disease and erectile dysfunction May recur in all patients	(Shelley et al., 2009)

Chemotherapy	Metastatic and advanced prostate cancer	Only first-line treatment for metastatic castration-resistant or advanced metastatic stage Applicable for combination with hormone therapy or radical prostatectomy	Systemic toxicity induced adverse effects such as nausea, vomiting, diarrhea, and hair loss	(Gravis et al., 2017; Quinn, Sandler, Horvath, Goldkorn, & Eastham, 2017)
Immunotherapy	Metastatic and advanced prostate cancer	Novel alternative treatment for patients with advanced or castration-resistant prostate cancer Low toxic Great potential to support other therapies	Have not achieved excited clinically relevant outcomes yet	(Anassi & Ndefo, 2011)

4.3 Basics of focused ultrasound (FUS)

FUS utilizes acoustic transducers to generate and concentrate the multiple intersecting ultrasonic waves on the targeted disease site less-invasively. FUS transducers are generally made of piezoelectric ceramics. A single FUS transducer with a spherical piezoceramic bowl only has a fixed focused spot, which is not applicable in the clinic. Phased array multi-element transducers are widely used in clinical HIFU devices, with the advantages of adjusting the location of focal spots via beam forming. Acoustic intensity (W/cm^2) provides information about the acoustic power of FUS waves per unit area. Temporal-peak acoustic intensity is the maximum instantaneous intensity in a FUS period, is generally regarded as a key parameter in FUS dosimetry (Barnett & Kossoff, 1984). In the clinic, the techniques of magnetic resonance (MR) or ultrasound (US) imaging are used to guide the FUS waves to target the diseased tissue precisely, ensuring the effectiveness of FUS treatment. The mechanism of FUS for medical applications is based on thermal and mechanical effects (Gourevich et al., 2013). In current clinical practice, HIFU-induced thermal ablation (at temperature above 55 °C) of the targeted tissue has been approved for the clinical treatment of uterine myomas, bone metastasis-related pain, essential tremor and Parkinson's disease. Since 2015, HIFU system has been approved by FDA for prostate tissue ablation. Currently, multiple medical applications of FUS are still in the research phase, and various clinical trials are undergoing. More biological and physical understanding is required for the investigation of FUS application in cancer therapy.

4.3.1 Medical application of FUS-induced thermal effects

Acoustic waves are concentrated in a focus spot to generate thermal effects on the tumors precisely while minimizing harm to the surrounding healthy tissues. Various temperatures and treatment durations will lead to different therapeutic effects for tumors (Figure 5). Current research is bent on the thermal ablation of tumors and the innate immune response induced by thermal ablation, as well as the combinatory treatment of local hyperthermia with radiation therapy or chemotherapy.

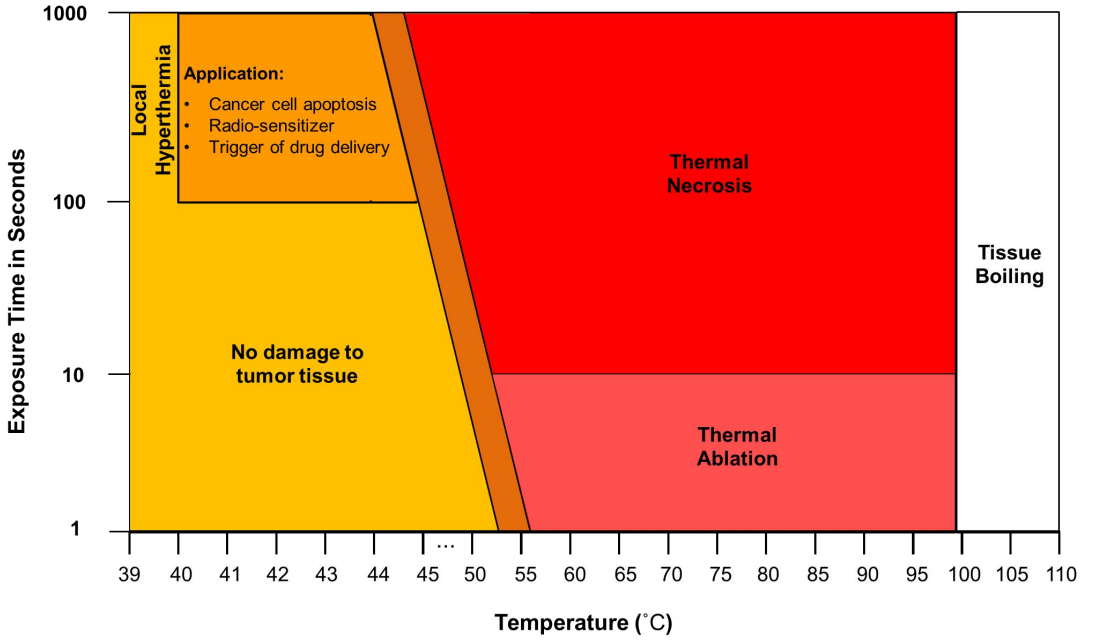

Figure 5: Schematic reveals the relation of treatment duration and temperature with therapeutic effects for tumor tissues. The treatment of 40 – 45 ˚C within 10 s has no damage to tumor tissue, but the treatment of above 100 s will cause local hyperthermia, which is applied to induce apoptosis (Saliev, Feril, Nabi, & Melzer, 2013), radio-sensitization of cancer cells (Peeken et al., 2017) and trigger the drug delivery (Thanou & Gedroyc, 2013). The treatment of thermal ablation is 55 – 100 ˚C for approximately 10 s, and the temperature range for more than 10 s will lead to thermal necrosis of tumor tissue. Above 100 ˚C for any duration will result in tissue boiling. Adapted from Focused Ultrasound Foundation (https://www.fusfoundation.org/mechanisms-of-action/thermal-ablation).

4.3.1.1 High-intensity focused ultrasound (HIFU) induced thermal ablation

FUS utilizes acoustic waves to target and generate intense heat (over 55°C) for induction of tissue necrosis under magnetic resonance imaging (MRI) guidance. Clinical research on HIFU ablation for localized prostate cancer began in the 1990s. There have now been three FUS manufacturers approved by the FDA

in the US for the ablation of prostate tumor – SonaCare Medical (Charlotte, USA), EDAP-TMS (Lyon, France), and Profound Medical (Mississauga, Canada), approximately 40,000 prostate cancer patients have been treated with HIFU till 2017 (Chaussy & Thüroff, 2017). HIFU is a less-invasive therapeutic modality for the treatment of small, localized prostate tumors because the heating spot generated by HIFU is small and can be positioned precisely inside target region (Beerlage et al., 1999). The less-invasiveness of HIFU ablation allows repeated procedure, secondary radical treatment, short hospital stay and a very low rate of complications. However, it is not feasible for all localized prostate cancer, such as massive or multiple tumors (Marien, Gill, Ukimura, Betrouni, & Villers, 2014). The ultrasonic energy is attenuated with the increased propagation distance, and the heat can be absorbed by the blood flow, any bone or gas barrier. For the treatment of deep tumors or tumors with barriers along the acoustic beam path, it is important to find a way to increase the efficiency of HIFU ablation and minimize damages to surrounding normal tissue (Zhang et al., 2019). Van Velthoven et al. (van Velthoven et al., 2016) reported the mid-term oncologic and functional results of primary HIFU hemi-ablation in 50 patients with localized prostate cancer. The biochemical recurrence, five-year actuarial metastases-free survival, cancer-specific survival, and overall survival rates after HIFU ablation were 36 %, 93 %, 100 %, and 87 %, respectively. The progression-free survival after HIFU ablation was 63 – 87 %, and negative postoperative biopsies were seen in 82 – 94 % of patients in the studies of median follow-up ranged from 12 – 24 months (Aus, 2006).

4.3.1.2 Hyperthermia: an alternative heating strategy to sensitize cancer cells for radiation therapy and chemotherapy

Hyperthermia (HT) refers to the generation of heat at the tumor site to 40 – 45 ˚C for tens of minutes (max. 60 min) to induce cancer death (M. Hurwitz & Stauffer, 2014). HT technology can be classified into whole body HT, localized HT and regional HT, which are regularly employed to treat solid tumors in deep tissue (Peeken, Vaupel, & Combs, 2017). The current HT techniques include electromagnetic-HT techniques such as radiofrequency and microwave, ultrasound-induced HT and novel magnetic nanoparticle heating. Compared to other techniques, FUS-induced HT shows a benefit of sufficient tissue penetration and allowance of beam focusing and shaping for both superficial and deep HT treatment. The HT caused by FUS has also been reported to induce cancer cell apoptosis (Saliev, Feril, Nabi, & Melzer, 2013). MRI allows the performance of less-invasive temperature monitoring inside the tumor. Application of HT may

induce changes in the tumor microenvironment, DNA repair damage of tumor cells, and stimulation of immune responses, which is used as adjuvant therapy to support radiation therapy or chemotherapy (Peeken et al., 2017). However, high absorption of bone and the penetration through air-containing tissue (e.g. gastrointestinal and respiratory tract) is still challenging in clinical applications. In the report of M. D. Hurwitz et al. (M. D. Hurwitz et al., 2005), patients with locally advanced prostate cancer received treatments of ultrasound-induced HT plus radiation therapy, the cancer-free survival rate was significantly enhanced to 84 % compared to the rate of 64 % of patients who underwent short-term androgen-suppression. Algan et al. (Algan et al., 2000) reported external beam radiation combined with transrectal ultrasound HT was conducted in 26 patients with locally advanced prostate carcinoma, the median overall survival (OS) and median no evidence of disease (bNED) survival were 88 and 38 months, respectively, and the 5-year OS and 5-year bNED survival were 73 % and 35 %. Zhu et al. (Zhu et al., 2019) summarized clinical applications of ultrasound-induced HT for prostate cancer treatment, indicating that FUS-induced HT is a practical adjuvant approach to radiation therapy for improvement of tumor control rates. Although promising clinical results have been reported, different HT and radiation therapy sequences, radiation dose, time intervals, and thermal dose are crucial for the establishment of efficient treatment strategies. The interactions between FUS-induced HT and radiation therapy still need to be understood, as well as the biological mechanisms.

4.3.1.3 FUS-induced hyperthermia triggered drug delivery with thermo-sensitive drug carriers

Hyperthermia (HT) is revealed to improve drug release from thermo-sensitive drug carriers into solid tumors, potentially overcoming the drug delivery barriers in the tumor microenvironment, thus controlled and targeted release of active drug is feasible. Many studies focused on varieties of thermo-sensitive drug carriers, including liposomes, nanoparticles and cyclodextrins, activation of drug release *in vitro* and *in vivo* were reported. The *in vivo* experiments showed that the combination of HIFU exposures and thermo-sensitive liposomes resulted in significantly rapid delivery and higher concentration of doxorubicin within tumors compared with liposomes alone (Dromi et al., 2007). Later the Magnetic resonance (MR)-imageable thermo-sensitive liposomes were developed to monitor and control the drug release from liposomes in real-time (Negussie et al., 2011). MR-guided focused ultrasound is a proven technique to generate HT for image-guided drug delivery. However, more types of thermo-sensitive carriers such as

polymers need to be further developed, and further basic studies are required to illuminate the physiological mechanism for enhancement of drug delivery efficiency by FUS-induced HT (Thanou & Gedroyc, 2013).

4.3.2 Medical application of FUS-induced mechanical/cavitation effects

FUS-induced mechanical effects involve acoustic streaming as well as the interaction between acoustic pressure and vapor-filled bubbles. As one of the most crucial mechanical effects, cavitation is the linear or nonlinear oscillation of small vapor-filled cavities in the effects of expansion and compression cycles traveling through a medium in an acoustic field (Figure 6A) (Zahra Izadifar, Babyn, & Chapman, 2019). Stable oscillations of small vapor-filled cavities (i.e. stable cavitation (Figure 6B)) at low acoustic pressures induce micro-streaming around cavitation nuclei, and increase mass transmission through micromixing and convection (Wiggins & Ottino, 2004). This effect is named stable cavitation, which is applied for the induction of cell sonoporation and support drug delivery. At high acoustic pressures, the small-sized vapor-filled cavities will expand rapidly over a few acoustic cycles and collapse violently. The phenomenon is termed inertial cavitation (Figure 6C), during which the generation of shock waves and liquid microjets are applied for histotripsy and induction of anti-vascular effects. In order to utilize the bio-effects of cavitation preferably, the detection of cavitation is incredibly essential. Although diverse methods have been developed to detect cavitation, few clinical trials are involved. The various potential bio-effects of cavitation have been established for cancer treatment *in vitro* or in animal models, but the clinical detection and application of cavitation are still the most vital challenge.

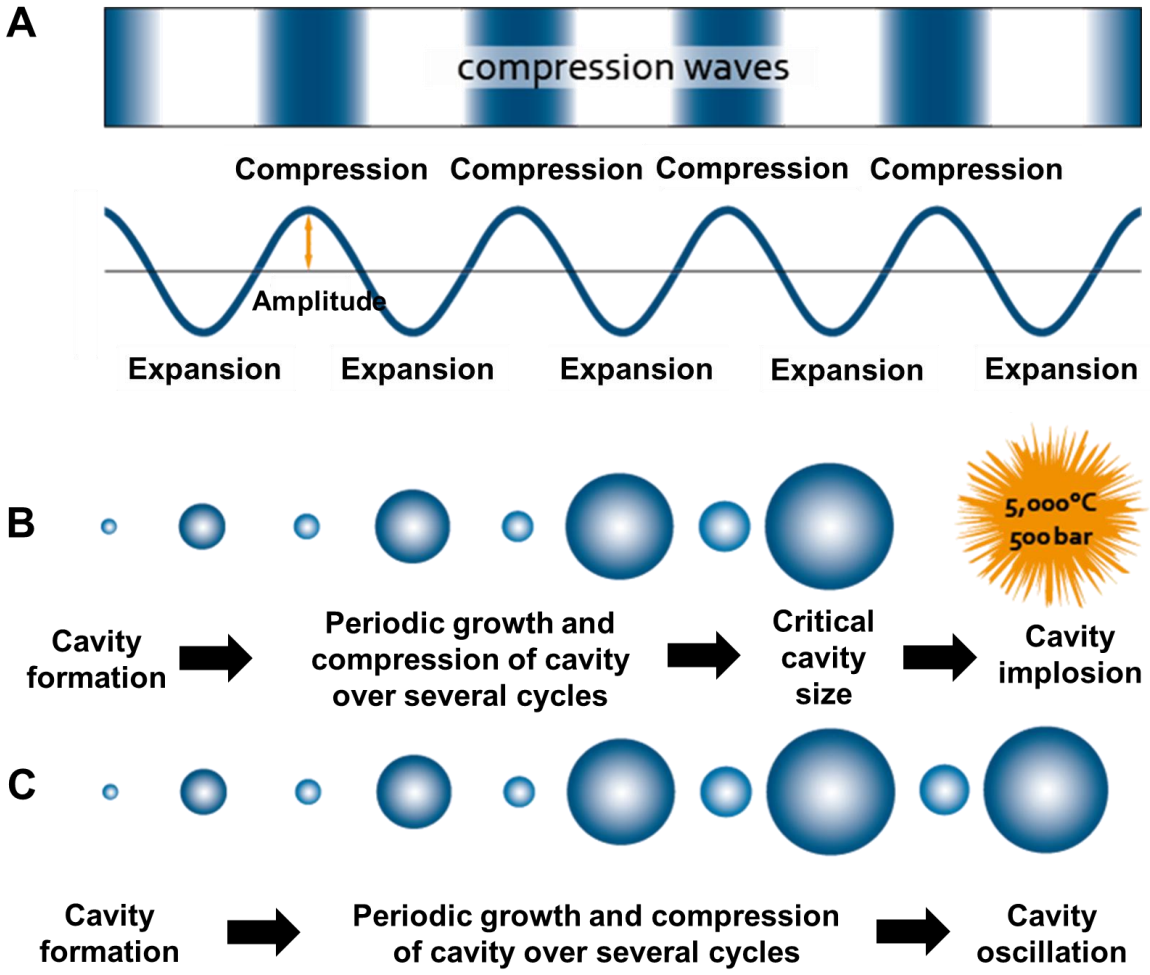

Figure 6: Schematic diagram shows cavitation occurrence in the acoustic field. (A) The expansion and compression cycles are traveling through a medium in an acoustic field. (B) Inertial cavitation: the size of the small vapor-filled cavity increases with the ultrasonic expansion cycle until it reaches the critical cavity size and then implodes violently. (C) Stable cavitation: the small vapor-filled cavity does not implode violently but oscillates in a stable state for multiple cycles. Adapted from (Zahra Izadifar et al., 2019).

4.3.2.1 Cell sonoporation for drug delivery

Cell membranes generally prevent extracellular molecules such as toxic chemotherapeutic drugs or genes from penetrating and functioning in cells. Enhancement of cellular drug uptake is the main obstacle in research. FUS-induced stable cavitation can induce sonoporation (Figure 7A), and the temporary enhancement of the cell membrane permeability achieves effective targeted drug delivery (Figure 7B). Stable cavitation depends mainly on acoustic intensity but not on temperature. With the presence of ultrasound contrast agents (e.g. microbubbles (MBs)), the cavitation threshold is decreased, and only lower

acoustic intensities are required for induction of sonoporation. Conversely, higher acoustic intensities are required for induction of drug release from thermo-sensitive carriers. Accordingly, low-intensity ultrasound is able to trigger targeted drug release from MBs-based drug delivery (F. T. Yu, Chen, Wang, Qin, & Villanueva, 2016). In clinical practice, ultrasound triggered drug delivery via sonoporation is expected to enable the local release in tumor site and reduce the system toxicity. In the study of Y. Wang et al. (Y. Wang et al., 2013), the combination of sonoporation and chemotherapeutic drug mitoxantrone HCl significantly enhanced the chemotherapeutic efficacy compared to the single chemotherapy in prostate cancer cell line DU145. Additionally, FUS-induced sonoporation is a good option for the delivery of genes. For example, Zolochevska et al. (Zolochevska et al., 2011) reported that the sonoporation enhanced a 60- to 200-fold delivery efficiency of Interleukin-27 in gene expression, thus improve the accumulation of effector cells in the tumors and reduce tumor growth in prostate cancer xenograft models. These results are potentially relevant to the development of novel therapies that sonoporation can be performed as a more effective tool to enhance the delivery efficiency of drugs or genes.

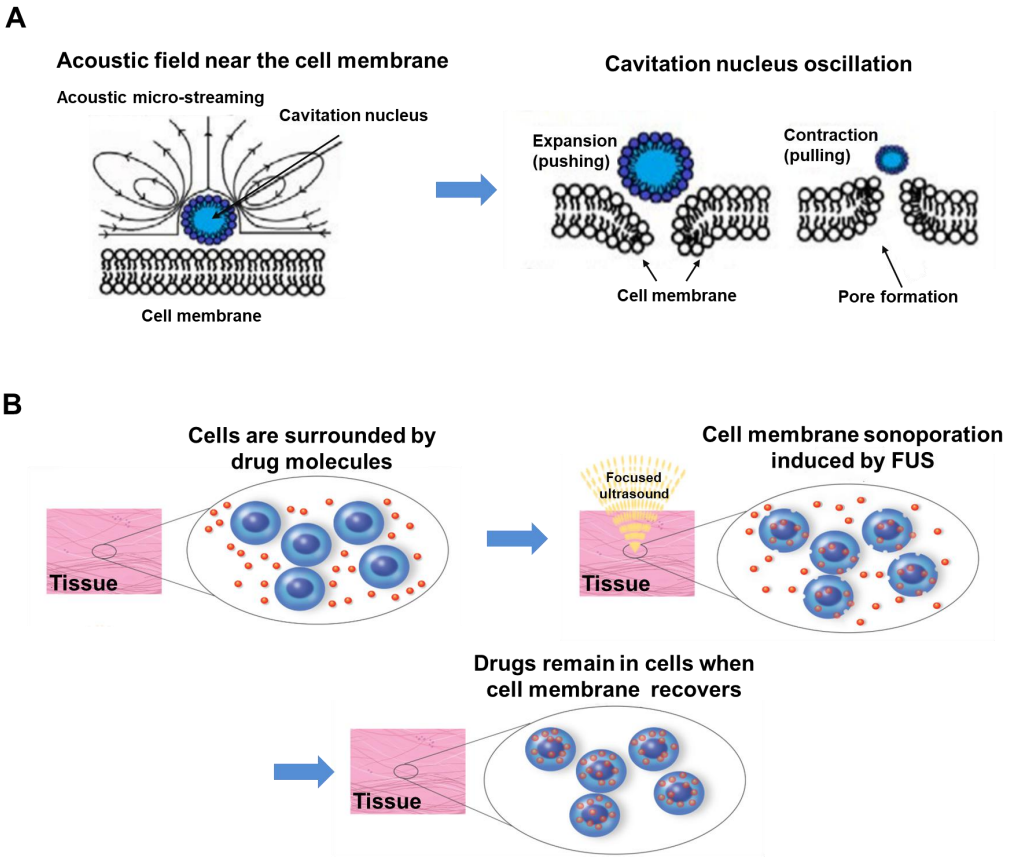

Figure 7: Schematic diagram demonstrates targeted drug delivery triggered by FUS-induced sonoporation. (A) Schematic illustration of sonoporation: stable cavitation initiated by acoustic micro-stream creates reversible pores of cell membranes. (B) FUS-induced sonoporation allows penetration of drugs into cells to function before cell membrane recovers. Adapted from Focused Ultrasound Foundation (https://www.fusfoundation.org/mechanisms-of-action/sonoporation) and (https://www.labcyte.com/media/pdf/POS-Sonoporation-Cell-Transfection-Blauw kamp.pdf).

4.3.2.2 Sonoporation induced anti-proliferative effects for cancer cells

Within a short time after ultrasound exposure, sonoporated cells are able to reseal the cell membrane via repair of the disrupted site with intracellular vesicles, which is unarguably crucial to the survival of sonoporated cells (Hassan, Campbell, & Kondo, 2010). However, the self-repairing of cell membrane does not inevitably signify that sonoporation has no impact on cell lone-term survival. In fact, there are numerous papers reporting the anti-proliferative effects of sonoporation or cavitation on cancer cells (Feril & Kondo, 2004; D. L. Miller & Dou, 2009; Zhong et al., 2011; Karshafian et al., 2010; X. Chen et al., 2013; Saliev, Feril, Nabi, & Melzer, 2013). Saliev et al. (Saliev, Feril, Nabi, & Melzer, 2013) considered that FUS-induced cavitation could be an alternative for the induction of cancer cell apoptosis. Miller et al.

(D. L. Miller & Dou, 2009) discovered sonoporation-induced apoptosis in human leukemia-derived cells. Zhong et al. (Zhong et al., 2011) published that the sonoporation-induced apoptosis of human leukemia cells was associated with the decreased expression of polyadenosine diphosphate ribose polymerase (PARP) protein, which is a pro-apoptotic marker correlated to impairment of DNA repair functionality. It was also found that sonoporation disturbed the expression of a variety of checkpoint proteins such as cyclin and Cdk (cyclin-dependent kinase) that play a vital role in cell-cycle progression, thereby inducing cell-cycle arrest in human leukemia-derived cells. Karshafian et al. (Karshafian et al., 2010) reported sonoporation led to a significant decline in the long-term clonogenic survival fraction of mouse fibrosarcoma cells. Moreover, sonoporation was also reported to prolong the DNA-synthesis time in breast cancer cells, indicating a delay in cancer cell-cycle progression. These characteristics are cellular stress response performance, implying that sonoporation constituted pressure to breast cancer cells (X. Chen et al., 2013).

4.3.2.3 Histotripsy

Histotripsy refers to tissue destruction via inertial cavitation and other mechanical effects of ultrasound, a less-invasive strategy for many disorders like benign prostatic hyperplasia, malignant tumors, congenital heart defects, and deep vein thrombosis. The advantage of histotripsy compared to thermal ablation is that the destroyed tissue residue can be reabsorbed by neighboring tissue or excreted out by body orifices (Schade et al., 2012). The feasibility of histotripsy was assessed in the treatment of prostate tumors in the canine model, suggesting the histotripsy-based tissue destruction was a promising approach for the treatment of prostate cancer (Schade et al., 2012). Xu et al. (Z. Xu, Owens, Gordon, Cain, & Ludomirsky, 2010) successfully achieved atrial septal defects with histotripsy less-invasively in a live canine model under real-time ultrasound image guidance, demonstrating that histotripsy had good potential to become a valuable tool in the clinic. In the latest research, the first histotripsy trial in humans for liver cancer therapy was published with the utilization of the HistoSonics (Michigan, USA) robotic positioned histotripsy system for the destruction of primary and metastatic liver tumor (Frisbie, 2020).

4.3.2.4 Anti-vascular and anti-metastatic effects

Networks of tightly connected endothelial cells mainly limit drug delivery across the walls of blood vessels. The cavitation effects induced by FUS can reversibly interrupt these tight junctions to increase the

permeability of the blood vessels, and the drug can penetrate blood vessels and enter the target tissues. Moreover, the anti-vascular effects induced by cavitation were applied as an adjuvant to radiation therapy. As mentioned above, with the presence of MBs, lower acoustic energy is required for induction of cavitation, thereby reducing the risk of blood vessel damage (Tung, Vlachos, Feshitan, Borden, & Konofagou, 2011). Daecher et al. (Daecher et al., 2017) described that a combination of cavitation effects induced by FUS with MBs resulted in apoptosis of vascular endothelial cells and improved the tumor sensitivity to radiation therapy. The mice treated with radiation therapy at 2 Gy combined with ultrasound-triggered MBs reduced the vascular permeability in 24 hours, the changes of blood flow at the tumor site synergistically enhanced the effects of radiation therapy (Kwok et al., 2013). Additionally, cavitation was reported to induce anti-metastatic activity in prostate cancer PC-3 cell line. Wei et al. (Wei, Bai, Wang, & Hu, 2014) discovered that the PC-3 cell reproduction ability, the level of cell invasion were suppressed 12 – 24 h after the 30 s cavitation treatment induced by the ultrasound (continuous mode) mediated MBs, and the molecular mechanism was investigated as the down-regulation of two metastatic-related proteins, matrix metalloproteinase (MMP)-2 and MMP-9. Cavitation was considered as a promising treatment regime to inhibit the invasion and migration of prostate cancer. Further clinical trials are expected to explore the outcomes and mechanisms of FUS-induced cavitation as a radio-sensitizer or anti-metastatic approach for cancer therapy.

4.3.3 The state of art of cavitation detection in medical application

In order to precisely control cavitation events within the acoustic field, detection and mapping of cavitation events are necessary. Over the past decades, multiple approaches have been explored for the detection and monitoring of cavitation, mainly include sonoluminescence, sonochemistry, passive cavitation detection (PCD), active cavitation detection (ACD), high-speed photography, laser scattering technique and synchrotron X-ray imaging technique (Zahra Izadifar et al., 2019). Each of these techniques carries specific advantages and disadvantages for cavitation measurement, and the specific details are presented below. Most published studies detecting cavitation are from *in vitro* experiments, and the achievement of controllable cavitation in the clinic still faces grand challenges. One difficulty for cavitation detection *in vivo* is associated with the attenuation of acoustic wave propagation induced by the inhomogeneous properties of tissue influencing the behavior of *in-situ* cavitation bubbles and the detection of cavitation

signals simultaneously (Zahra Izadifar et al., 2019).

4.3.3.1 Sonoluminescence and sonochemistry

The cavitation occurrence would induce a series of physical and chemical responses that can be used to indicate cavitation amount indirectly, known as sonoluminescence and sonochemistry. These methods are closely associated with the detection of different features of cavitation, mainly including cavitation-induced light emissions (sonoluminescence) and free radicals' production (sonochemistry) (Matula, Hilmo, Bailey, & Crum, 2002). Sonoluminescence refers to a pulse of visible light emission from violently cavitation bubbles collapse. In addition, the collapse of cavitation bubbles further generates extremely high local temperatures, high-speed fluid jets as well as high pressures. In a large scale of *in vitro* studies, detection of light intensity of sonoluminescence with a photomultiplier tube was used to quantify cavitation dose (Cochran & Prausnitz, 2001). Inertial cavitation generates high temperatures and high pressures, leading to the breakdown of water and other molecules to produce free hydroxyl radicals. Quantification of the produced free hydroxyl radicals has been used to evaluate inertial cavitation activity (Shanei & Shanei, 2017). In the early research of sonochemistry, free radicals generated by inertial cavitation were detected using the electron-spin-resonance (ESR) spin-trap method, which efficiently measured the short-term amount of free hydroxyl radicals. ESR signal intensity measured by the ESR spectrometer was used to indicate inertial cavitation activity (P. Li, Takahashi, & Chiba, 2009). However, the availability of ESR is restricted in only a few specialized laboratories. A chemical trap terephthalic acid (TA) is generally applied as the hydroxyl radical scavenger. In this method, the TA solution at a concentration of 2 mM is used as a dosimetric solution to react with free hydroxyl radicals generated by cavitation-induced water sonolysis. The fluorescent product 2-hydroxyterephthalic acid (HTA) can be quantified using fluorescence spectroscopy at excitation and emission wavelengths of 310 and 425 nm, and the detected fluorescence value can indirectly represent the inertial cavitation dose (Shanei & Shanei, 2017). Although sonoluminescence and sonochemistry allow quantitative measurement of cavitation at high efficiency and low cost, the insufficient feasibility of *in vivo* systems, indirectness of measurement and inability in real-time measurement are the main limitations of these methods for cavitation measurement (Atchley et al., 1988).

4.3.3.2 Passive cavitation detection

Special listening transducers or hydrophones (i.e. passive cavitation detectors) are used for passive records of acoustic emissions and detection of cavitation activity. Stable cavitation is indicated by sub-harmonic and ultra-harmonic emissions associated with bubble oscillations. Broadband acoustic emissions represent inertial cavitation, which is associated with bubble collapse (Hoerig, Serrone, Burgess, Zuccarello, & Mast, 2014). As the most commonly used approach for the determination and control of cavitation in the biomedical field, PCD technology is able to perform digital simulation precisely for cavitation events caused by ultrasound and has good clinical applicability.

Lo et al. (Lo et al., 2014) utilized a needle hydrophone to measure and control the cavitation events that occurred in a 24-well plate. The results showed that accurate, stable and repeatable cavitation levels could be obtained using the hydrophone method. In contrast to the needle hydrophone, the fiber-optic hydrophone (FOH) with a thin optic fiber sensor was able to be located inside the 96-well plate, allowing low interference to the acoustic field and more accurate determination of cavitation dose for the limited space (Bull, Civale, Rivens, & ter Haar, 2011). A lot of prior researches manifested that PCD technique could also be utilized to determine the cavitation activity within *ex vivo* tissues or tissue mimicking phantom, and FOH sensor showed an advantage of ease of positioning within the tissues or phantom and higher spatial sensitivity to cavitation occurring within samples (Bull, Civale, Rivens, & ter Haar, 2011; Lai, Wu, Chen, & Li, 2006; Maxwell, Cain, Hall, Fowlkes, & Xu, 2013; Morris, Hurrell, Shaw, Zhang, & Beard, 2009). The PCD technique was also reported to determine the cavitation activity precisely *in vivo*. For example, cavitation activity in the prostate tumor growing subcutaneously in the thigh of male rats was accurately determined by FOH (Huber, Debus, Peschke, Hahn, & Lorenz, 1994). The inertial cavitation was assessed precisely by a PCD system in the rabbit auricular vessels (Hwang, Tu, Brayman, Matula, & Crum, 2006). Although position-dependent changes in cavitation activity cannot be detected by single-element passive cavitation detectors, multi-element detectors such as ultrasound arrays can be potentially applied for the detection of 2D-resolved cavitation activity. Salgaonkar et al. (Salgaonkar, Datta, Holland, & Mast, 2009) utilized a 192-element array to create real-time passive cavitation images in phosphate-buffered saline (PBS) solution sonicated with ultrasound at 520 kHz. The cavitation clouds developed in the PBS sample were continuously detected by passive cavitation images and B-mode images.

They additionally created passive cavitation images using broadband noise in bovine liver sonicated with 2.2 MHz ultrasound. Passive cavitation imaging (PCI) can be potentially applied to directly visualize the ultrasound-induced cavitation that occurred in tissues in clinical trials. Cavitation is unexpected in many ultrasound-ablation therapies, and PCI system is utilized to monitor the broadband emissions to avoid inertial cavitation-induced inadvertent tissue injury. Such PCI detection is available in clinical ultrasound systems ExAblate (Insightec, Haifa, Israel) and Sonalleve (Profound Medical, Mississauga, Canada). Currently, PCI is the rare clinically applicable technique that can precisely detect cavitation events and provide real-time information about the bubble oscillation mode and strength (Gyongy & Coussios, 2010). Even the PCI technique cannot realize the visualization of the bubble oscillation in real-time, it provides valuable information that is helpful for analysis of the environmental dynamics in the cavitation field (Cleveland, Sapozhnikov, Bailey, & Crum, 2000).

4.3.3.3 Active cavitation detection

ACD employs a transducer to transmit interrogating pulses in the cavitation fields, and the other transducers pick up echoes from oscillating cavitation bubbles located in the acoustic field for the characterization of cavitation activities. How to distinguish the cavitation bubbles from tissues is the most crucial question in the process. Compared with PCI, active cavitation imaging (ACI) can obtain images of both stable and inertial cavitation, and the spatial resolution is higher than PCI (Alvarez et al., 2020). B-mode imaging is one of the most commonly accepted ACI technologies, which establish cavitation bubble-related hyperechoic regions in the image. Different from passive cavitation detection methods, most of the ACI studies are performed in animal experiments. For instance, a passive detection utilizing coincident signals from orthogonal receivers combined with an active detection utilizing echo B-mode ultrasound was used for cavitation monitoring during shock-wave lithotripsy in a pig kidney (Holland et al., 1996).

4.3.3.4 High-speed sequential photography of cavitation dynamics

In order to observe the behavior of cavitation, a high-speed camera with a frame rate of several million frames per second is the most direct approach to investigate its dynamics (Tinne et al., 2010). Ibsen et al. (Ibsen et al., 2011) utilized the combination of fluorescence microscopy and high-speed photography to

obtain the images of the unique drug delivery carrier (i.e. fluorescent-labeled MBs with loaded drugs) interacting with ultrasound waves. The technique of high-speed camera enables visualization of cavitation dynamics. However, it is limited in the *in vivo* system due to low practicality, restricted field of view and depth of field (Zahra Izadifar et al., 2019).

4.3.3.5 Laser scattering technique

A laser beam irradiates the oscillation bubbles, and a photo detector receives the scattered light from the bubble. The technique is named as laser scattering technique. For a single oscillating bubble, the scattered light amplitude will vary with the change of bubble radius. Therefore the parameters related to the oscillating bubble dynamics are obtained to analyze the cavitation activity (Burdin, Tsochatzidis, Guiraud, Wilhelm, & Delmas, 1999). This technique provides an exact determination of oscillating bubble dynamics, but only small-size bubbles are allowed, and the quantification of bubble clouds or non-spherical bubbles is not feasible (Maeda & Colonius, 2019).

4.3.3.6 Synchrotron X-ray imaging technique

Synchrotron X-ray imaging is another novel technique to investigate the cavitated bubble dynamics. This technique utilizes a bright and collimated X-ray beam to irradiate the cavitation field, where the cavitated bubbles will scatter the X-rays (Zahra Izadifar et al., 2019). Analyzer-based imaging and X-ray phase-contrast imaging display good potential for visualization of cavitated bubbles behavior. X-ray imaging technology is capable of imaging the characteristic structure of the gas-liquid interface in cavitated bubbles to realize the visualization of cavitation dynamics in an optically opaque material such as tissue. The technique has the advantage of visualizing the cavitated bubbles' dynamics without interference to the acoustic field (Z. Izadifar, Belev, Izadifar, Izadifar, & Chapman, 2014).

4.3.3.7 MRI techniques

MRI is an imaging technology based on the physical principle of nuclear magnetic resonance, which can map the structure of human tissues or organs. The HIFU devices employ the MRI technique to guide the high-intensity FUS wave, allowing the focal spot of FUS to be positioned inside the target region precisely in the body. Besides, MRI technique was reported to detect cavitation during the FUS ablation. Due to the

good linearity and temperature dependence, proton resonance frequency (PRF) shift MR thermometry is widely used in MRI-guided HIFU by measuring the phase change resulting from temperature-induced PRF shift (Rieke & Butts Pauly, 2008). During MRI-guided FUS ablation, cavitation-induced thermal effect leads to the drastic phase shift in the PRF sequences, demonstrating that cavitation can be reliably detected by the thermal-induced PRF phase shift (Kopechek et al., 2014). Accordingly, the technique of PRF shift MR thermometry is an inappropriate method for the study of the cavitation effect separated from the thermal effect.

Magnetic resonance elastography (MRE) is a fast-developing technology for quantitatively evaluating the mechanical characteristics of tissue. With the MRE technique, shear waves in the targeted tissue are generated by a mechanical vibrator, and the MR acquisition sequence is able to measure the propagation and velocity of induced shear waves to map the elastograms reflecting the tissue stiffness quantitatively (Mariappan, Glaser, & Ehman, 2010). FUS was investigated as a method to create mechanical vibration for multiple elasticity imaging approaches including MRE (Mariappan, Glaser, & Ehman, 2010). Acoustic radiation force impulse (ARFI) imaging utilizes FUS transducers to send the short-duration focused acoustic impulses into the small volume tissue, and the shear waves generated from the tissue response to the focused acoustic impulses are monitored to acquire information regarding the tissue structure and stiffness. The tissue response includes the localized displacements of the examined tissue. These displacements can be monitored spatially and temporally using ultrasound (US-ARFI) or MR (MR-ARFI). The magnitudes of these displacements are inversely proportional to tissue stiffness (Cafarelli et al., 2018; Nightingale, Soo, Nightingale, & Trahey, 2002). Similar to MRE, MR-ARFI technique encodes the slight displacements of tissue into the MRI phase signal by using motion-sensitizing gradients (Vappou, Bour, Marquet, Ozenne, & Quesson, 2018). MR-ARFI has also been reported to detect the cavitation-induced thermal effects via displacement images, thus determining the occurrence of cavitation indirectly (Elbes et al., 2014). Besides, Peng et al. (Peng et al., 2017) utilized the turbo spin-echo-based sequence to monitor the changes of MR signal caused by cavitation-induced flow turbulence in a tissue mimicking phantom. To sum up, MRI techniques detect the cavitation-induced physical responses (e.g. thermal effects or flow turbulence) to monitor the occurrence of cavitation. MRI can be used to guide the FUS waves for precisely anatomical targeting but is not able to directly detect the cavitation (Zahra Izadifar et al., 2019). Moreover, the assessment and quantification for the cavitation intensity by the MRI techniques have not been clarified.

5 Aims of the thesis

Cell sonoporation caused by FUS-induced cavitation is capable of inducing multiple anti-proliferative effects for various cancer cells, mainly including cell apoptosis, cell-cycle arrest and clonogenicity suppression. We hypothesize that FUS-induced cavitation can enhance the effects of radiation therapy, hyperthermia and testosterone treatment by interrupting the cancer cell membrane and changing the AR signaling pathway of the prostate cancer cells, with the potential to be a promising adjuvant therapy in the management of cancerous disease. In order to establish a fast, efficient and less-invasive adjuvant therapy for cancer treatments, the therapeutic effects of a single short cavitation treatment and the combination with other therapies are necessary to be clarified. (1) Detailed characterization of the *in vitro* FUS system and definition of the optimal parameters for induction of cavitation are the prerequisite for studying the therapeutic effects of FUS-induced cavitation in cancer treatments. To distinguish between effects of (2) single FUS-induced cavitation on cancer cells and (3) the adjuvant effects to other treatment modalities (e.g. radiation therapy and hyperthermia), the long-term effects of FUS (i.e. short FUS shots with or without cavitation) on cancer cells were determined via cell clonogenic survival after treatment with single FUS and FUS in combination regimes; the FUS-induced short-term effects were assessed by evaluating cell potential to invade and cell metabolic activity post single FUS and combination of FUS and radiation therapy or hyperthermia treatment, and thus give evidence about the suppression of long-term and short-term survival of cancer cells and potential mechanism in inhibition of cell invasion. (4) The sonoporation effect caused by cavitation was investigated to clarify the biophysical mechanism of FUS-induced therapeutic effects. (5) The effects of FUS at the molecular level were investigated by measuring the changes of 5α-reductase type I and type III levels in AR signaling pathway for prostate cancer cells. (6) Finally, in order to investigate the effects of the combination of testosterone treatment and FUS on prostate cancer cells, the long-term metabolic activity was evaluated after the single and combinatory regimes.

6 Materials and methods

6.1 Materials

6.1.1 Devices

The experiments in this study were performed with the devices listed in Tables 2 and 3.

Table 2: List of FUS device components, FUS device was developed at IMSaT (University of Dundee) and modified by us at ICCAS (University of Leipzig)

FUS device components	Manufacture and place of origin	Specification
Adjustable heater	Hydor, Salisbury, UK	ETH200
Custom interchangeable transducers	Institute for Medical Science and Technology (IMSaT), Dundee, UK	0.487 MHz; 1.142 MHz; 1.467 MHz
Custom transducer holder	IMSaT, Dundee, UK	Polyamide block
Linear stage	VELMEX Inc., Bloomfield, NY, USA	XSlide™ Assembly
Motor controller	VELMEX Inc., Bloomfield, NY, USA	VXM
RF power amplifier	Electronics and Innovation, Rochester, NY, USA	A075
Self-priming water pump	Lei Te Co., Ltd., Guangdong, China	LET-775
Stepper motor	STEPPERONINE, NY, USA	NEMA17
Water bath	Perspex International, Lancashire, UK	Perspex® compartment (14 × 10.5 × 6 cm^3)
Waveform signal generator	Agilent Technologies, Edinburgh, UK	33120 A

Table 3: List of devices and software

Equipment and software	Manufacture and place of origin	Specification
Attune NxT flow cytometer	Invitrogen by Thermo Fisher, Darmstadt, Germany	Attune NxT Acoustic Focusing Cytometer
Clean bench	Kojair Tech Oy, Mänttä-Vilppula, Finland	Bio Wizard Silver Line Biosafety cabinet
Centrifuge	Hettich, East Westphalia, Germany	ROTINA 420R
Flake ice machine	BREMA Ice Makers, Villa Cortese, Italy	Ice Makers ™ GB902AX
FOH system	Precision Acoustics, Dorchester, UK	FOH system66
Image J	An open platform developed by Wayne Rasband, USA	IJ 1.46r
Incubator	Thermo Fisher Scientific, Darmstadt, Germany	Hera cell 240
Inverted Microscope	Carl Zeiss microscopy GmbH, Jena, Germany	Axio Observer
LabVIEW	National Instruments, Austin, Texas, USA	Version 16.0
Laboratory refrigerator	Philipp Kirsch GmbH, Willstätt, Germany	– 20 ℃
Laboratory analytical balance	Sartorius, Göttingen, Germany	ME254S
MATLAB	The MathWorks, Portola Valley, California, USA	R2017a
Microliter centrifuge	Heraeus, Hanau, Germany	24 place, 13000 RPM
Microplate reader	BioTek Instruments, Inc., Bad	SYNERGY H1

	friedrichshall, Germany	
Milli-Q ® Reference water purification system	Merck Millipore, Darmstadt, Germany	C79625, type 1 ultrapure water
Oscilloscope	Pico Technology, St Neots, UK	PicoScope 5243B
Stand refrigerator	Siemens, Munich, Germany	2 – 11 °C
Thermal camera	Optris GmbH, Berlin, Germany	Optris PI450
Thermocouples	Pico Technology, St Neots, UK	Type T, PTFF-insulated Cu-Constantan, 0.076 mm wire diameters
Thermocouple data logger	Pico Technology, St Neots, UK	TC-08
Ultra-Low temperature freezer	SANYO, Osaka, Japan	– 150 °C
Vertical standing autoclave	SysTec, Naunhof, Germany	SYSTEC V series
Water bath	GFL, Burgwedel, Germany	40 L
X-ray machine	XStrahl, Camberley, UK	XStrahl 200

6.1.2 Chemicals and reagents

All chemicals and reagents used in the study are listed in Table 4.

Table 4: List of applied chemicals and reagents

Reagent	Manufacture and place of origin	Specification
Acetone	Sigma-Aldrich, Munich, Germany	ACS grade, ≥ 99.5 %
Acetonitrile	Carl Roth, Karlsruhe, Germany	ROTISOLV ® HPLC Ultra Gradient Grade
Anti-SRD5A1 antibody produced in rabbit	Sigma-Aldrich, Munich, Germany	Unconjugated, polyclonal, 100 µL
Anti-SRD5A3 antibody produced in rabbit	Sigma-Aldrich, Munich, Germany	Unconjugated, polyclonal, 100 µL

Anti-Rabbit IgG (H+L), F(ab')2 Fragment (Alexa Fluor® 594 Conjugate)	Cell Signaling Technology, Danvers, Massachusetts, USA	250 µL
Attune ™ Bleach	Invitrogen by Thermo Fisher, Darmstadt, Germany	15 mL, For use with Attune NxT Acoustic Focusing Cytometer
Attune ™ Focusing fluid (1×)	Invitrogen by Thermo Fisher, Darmstadt, Germany	1000 mL, for use with Attune NxT Acoustic Focusing Cytometer
Attune ™ Performance measurement beads	Invitrogen by Thermo Fisher, Darmstadt, Germany	3 mL, for use with Attune NxT Acoustic Focusing Cytometer
Attune ™ Shutdown solution (1×)	Invitrogen by Thermo Fisher, Darmstadt, Germany	250 mL, for use with Attune NxT Acoustic Focusing Cytometer
Attune ™ Wash solution	Invitrogen by Thermo Fisher, Darmstadt, Germany	250 mL, for use with Attune NxT Acoustic Focusing Cytometer
Cell-Based propidium iodide solution	Cayman Chemical, Ann Arbor, Michigan, USA	1 mg/mL in PBS, pH 7.4, 250 µL per via
CellMask™ green plasma membrane stain	Thermo Fisher Scientific, Darmstadt, Germany	100 µL
Cell proliferation reagent WST-1	Carl Roth, Karlsruhe, Germany	25 mL
Crystal violet	Sigma-Aldrich, Munich, Germany	100 g, for microscopy
Dimethyl sulfoxide (DMSO)	Carl Roth, Karlsruhe, Germany	≥99.5 %, BioScience Grade, for molecular biology, 100 mL
Dulbecco's Modified Eagle Medium (DMEM)	Gibco® by Life Technologies, Darmstadt, Germany	500 mL, [+] 4.5 g/L D-Glucose, [+] L-Glutamine,

		[+] Pyruvate
Ethanol	Carl Roth, Karlsruhe, Germany	≥99.8 %, denatured, 2.5 L
Fetal bovine serum (FBS)	Gibco® by Life Technologies, Darmstadt, Germany	Origin from Brazil, 500 mL
Formaldehyde solution	Carl Roth, Karlsruhe, Germany	30 %, low in methanol, 1 L
Ham's F-12K (Kaighn's)-Medium	Gibco® by Life Technologies, Darmstadt, Germany	500 mL, [+] L-Glutamine
HEPES	Biochrom, Berlin, Germany	1 M
Matrigel® basement membrane matrix	Corning, New York, USA	Extracted from the Engelbreth-Holm-Swarm (EHS) mouse sarcoma
MEM non-essential amino acids	Sigma-Aldrich, Munich, Germany	100 ×
Methanol	Carl Roth, Karlsruhe, Germany	ROTISOLV ® HPLC Ultra Gradient Grade
Penicillin and streptomycin (Pen-strep)	Sigma-Aldrich, Munich, Germany	100 mL, contain 10,000 units penicillin and 10 mg streptomycin/mL
Phosphate-buffered saline (PBS) tablet	Sigma-Aldrich, Munich, Germany	100 tablets
Phosphate-buffered saline (PBS)	Biozym (Lonza), Hessisch Oldendorf, Germany	Without Ca ++, Mg ++, and phenol red, sterilized, 500 mL
Poly-L-Lysine	Sigma-Aldrich, Munich, Germany	0.01 %, 50 mL
RPMI Medium 1640 (1×)	Gibco® by Life Technologies, Darmstadt, Germany	500 mL, [+] L-Glutamine
Sodium hydroxide (NaOH)	Sigma-Aldrich, Munich, Germany	Pellets, ≥ 98 %, 100 G

Sodium pyruvate	Sigma-Aldrich, Munich, Germany	100 mM
Terephthalic acid (TA)	Sigma-Aldrich, Munich, Germany	Powder, ⩾ 98 %, 5 G
Testosterone solution	Merck KGaA, Darmstadt, Germany	1.0 mg/mL in acetonitrile, ampule of 1 mL
Triton ® X 100	Carl Roth, Karlsruhe, Germany	250 mL
Trypan blue solution	Sigma-Aldrich, Munich, Germany	50 mL, 0.4 % for microscopy
Trypsin/EDTA(10 ×)	Biozym (Lonza), Hessisch Oldendorf, Germany	1,700,000 U\L trypsin, 2g/L Versene® (EDTA), Porcine parvovirus and mycoplasma tested, 100 mL
Water bath protection agent	Julabo, Seelbach, Germany	Aqua Stabil protective agent
2-Hydroxyterephthalic acid (HTA)	Sigma-Aldrich, Munich, Germany	Powder, ⩾ 97 %, 1 G
4′,6-diamidino-2-phenylindole (DAPI)	Thermo Fisher Scientific, Darmstadt, Germany	Mounting Solution
2-Propanol	Carl Roth, Karlsruhe, Germany	≥99.8 %, 1 L

6.1.3 Consumables

All consumables used in the study are listed in Table 5.

Table 5: List of applied consumables

Consumables	Manufacture and place of origin	Specification
Alcoholic rapid disinfectant	Bacillol, Hamburg, Germany	Bacillol ® AF, 500 mL
Autoclave bags	VWR International, Dresden, Germany	Temperature-resistant polypropylene, 61 cm × 91.4 cm
Beakers	VWR International, Dresden,	Borosilicate 3.3 glass, with

	Germany	spout, 250 mL, 500 mL, 1000 mL
Cell culture flasks	Greiner bio-one, Stonehouse, UK	T25: 50 mL, 25 cm^2, T75: 250 mL,75 cm^2, T175: 550 mL, 175 cm^2, sterile
Cell culture microplates, 96-well, PS, transparent	Greiner bio-one, Stonehouse, UK	F-bottom (chimney shape), CELL STAR®, TC, sterile
Cell culture multiwell plates, 6 well, PS, transparent	Greiner bio-one, Stonehouse, UK	CELL STAR®, TC, sterile, 9.6 cm^2 of growth area, single packed
Cryogenic tubes	TPP Techno Plastic Products AG, Trasadingen, Switzerland	1.5 mL
DESCOSEPT sensitive rapid disinfectant	Dr. Schumacher, Malsfeld-Beiseförth, Germany	1 L
Disposable gloves	Carl Roth, Karlsruhe, Germany	ROTIPROTECT ® Nitril eco, size: M
Disposable weighing pans	VWR International, Dresden, Germany	Flat bottom, 25 mm × 38 mm
Flow cytometry tubes	SARSTEDT AG & Co. KG, Nümbrecht, Germany	5 mL
Freezer container	Thermo Fisher Scientific, Darmstadt, Germany	Capacity: 18 (1.0 to 2.0 mL tubes)
Hemocytometer	Paul Marienfeld GmbH & Co. KG, Lauda-Koenigshofen, Germany	Non-disposable, 0.0025 mm^2
Hemocytometer coverslips	Thermo Fisher Scientific, Darmstadt, Germany	20 × 26 × 0.4 mm
Kimtech Science™ precision	Kimberly-Clark Professional,	1 box of 280 wipes

wipes	Koblenz, Germany	
Laboratory bottles	VWR International, Dresden, Germany	Borosilicate glass 3.3, 50 mL, 100 mL, 250 mL, 1000 mL
Measuring Cylinders	VWR International, Dresden, Germany	Plastic, graduated cylinder, 100 mL, 1000 mL
Microtubes	SARSTEDT AG & Co. KG, Nümbrecht, Germany	2.0 mL
Millipak® Express 40 filters	Merck Millipore, Darmstadt, Germany	0.22 µm membrane
Neutral pipette tips	SARSTEDT AG & Co. KG, Nümbrecht, Germany	1.000 µL, MLA type
Nunc ™ MicroWell ™, black, 96-well plates	Thermo Fisher Scientific, Darmstadt, Germany	With transparent bottom made of polymer, cell culture, black
Parafilm M multi-purpose lab film	Pechiney, Paris, France	Non-sterile, 5 cm × 16 m
Pipette tips	SARSTEDT AG & Co. KG, Nümbrecht, Germany	200 µL, yellow
Reusable non-woven tissue dispenser system	Dr. Schumacher, Malsfeld-Beiseförth, Germany	DESCO WIPES
Sarstedt pipette tips	SARSTEDT AG & Co. KG, Nümbrecht, Germany	10 µL, sterile
Screw-cap tubes	SARSTEDT AG & Co. KG, Nümbrecht, Germany	15 mL, 50 mL, sterile
Serological pipettes	SARSTEDT AG & Co. KG, Nümbrecht, Germany	1mL, 5 mL, 10 mL, sterile
Standard disposable plastic spatulas, blue	Carl Roth, Karlsruhe, Germany	Non-sterile, 14 mm, blue
The PIPETMAN® L pipettes	Gilson, Limburg-Offheim,	P10L: 1 – 10 µL

	Germany	P200L: 20 – 200 µL P1000L: 10 – 1000 µL
Titer Tops® sealing film for microplates	Sigma-Aldrich, Munich, Germany	Non-cytotoxic, sterile, solvent resistant and waterproof, 8.26 cm × 15.24 cm
TPP® 24 well plates, transparent	TPP Techno Plastic Products AG, Trasadingen, Switzerland	F-bottom made of polystyrene, 1.86 cm^2, sterile
Transwell® Cell Culture Plate Inserts and accessories	Corning, New York, USA	Inserts in a 24 well plate, 10 µm thick polycarbonate membrane, 8 µm pore size, sterile
96-well cell culture microplates, black, µ-clear®	Greiner bio-one, Stonehouse, UK	F-bottom (fireplace shape), µ-clear®, black, CELLSTAR®, sterile

6.1.4 Human cancer cell lines

Permanent human cancer cell lines used in the study are listed in Table 6.

Table 6: List of applied cancer cell lines

Cell lines	Manufacture and place of origin	Specification
PC-3	The European Collection of Authenticated Cell Cultures (ECACC), EU	Human prostate cancer Epithelial, from metastasis in bone, androgen-independent, adherent, with tumorigenic in nude mice, p53-mutant
LNCap	The European Collection of Authenticated Cell Cultures (ECACC), EU	Human prostate cancer Epithelial, from metastasis at the left supraclavicular lymph node, androgen-dependent, adherent, single cells and loosely attached clusters, with tumorigenic in nude mice
T98G	Obtained from the University of Leipzig, Germany	Human glioblastoma Fibroblast, from brain, no-metastasis, adherent, without tumorigenic in nude mice, p53-mutant
FaDu	Obtained from National Center for Radiation Research in Oncology, Dresden, Germany	Human head and neck cancer Epithelial, from pharynx, no-metastasis, adherent, with tumorigenic in nude mice, p53-mutant

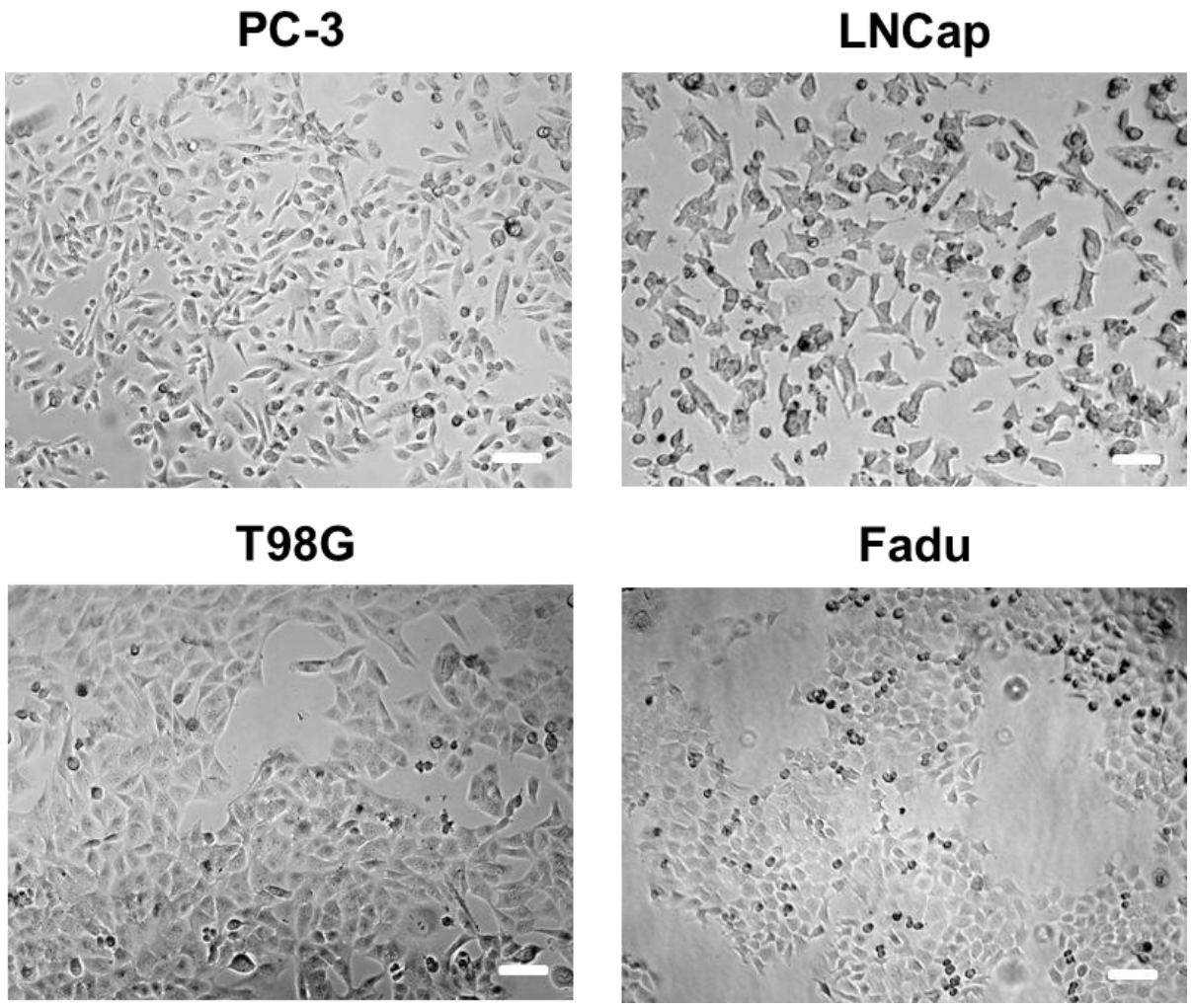

Figure 8: Microscopy images indicate adherent morphology of different cancer cell lines in 96-well plates. Cells were cultured for 24 h to form the adherent monolayer, scale bar = 100 µm.

6.2 Methods

6.2.1 Composition of the FUS system for *in vitro* treatment of cells

To treat human cancer cells *in vitro*, cells were cultured in special ultrasound penetrable 96-well µ-clear cell culture plates. The *in vitro* FUS apparatus contained a Perspex® water bath compartment (Figure 9B), where the ultrasound source (i.e. transducer) and 96-well cell culture plates were placed. The water enabled the delivery of ultrasound waves to the cells by acting as a transport medium, and the water also helped to have a stable temperature during the treatment. A self-priming water pump (Figure 9C) was employed for the circulation of degassed water to prevent bubble formation beneath the plate from interfering with the FUS wave propagation. The circulating water passed through an external heater

(Figure 9D) to hold the temperature. Since the limit of the pump was 34 °C, the temperature of circulating water was held three degrees below the physiological level (37 °C) to avoid overheating of cell culture medium during FUS treatments. A small polyamide block inside the water bath was used to detachably accommodate the customized single FUS transducers at frequencies of 0.487, 1.142 or 1.467 MHz (Figure 9A). The FUS transducers were made from Perspex® tubes (outer diameters = 40 mm) with geometrically-focused piezoceramic bowls positioned at the top of each tube. The outer diameters of the piezoceramic bowls were in the range of 30 – 35 mm. Adapted lengths of transducers were designed to precisely position the focus spot at the bottom of the 96-well plate (Figure 9E). Various waveforms could be generated by a FUS signal generator (Figure 9H) and amplified by an A075 RF power amplifier (Figure 9I). An X-slide linear stage connected to a programmable VXM motor controller and a NEMA 17 stepper motor (Figure 9F) were the main components of the motion system, which was used to move the 96-well plates for precise positioning of the focal regions at wells in different lines. Four starting positions of transducers on the polyamide block (Figure 9A) were alternated to sonicate selected wells in different columns of a 96-well plate. An infrared thermal camera (Figure 9G) was mounted above the 96-well plates to monitor the real-time temperature in the wells during FUS treatments.

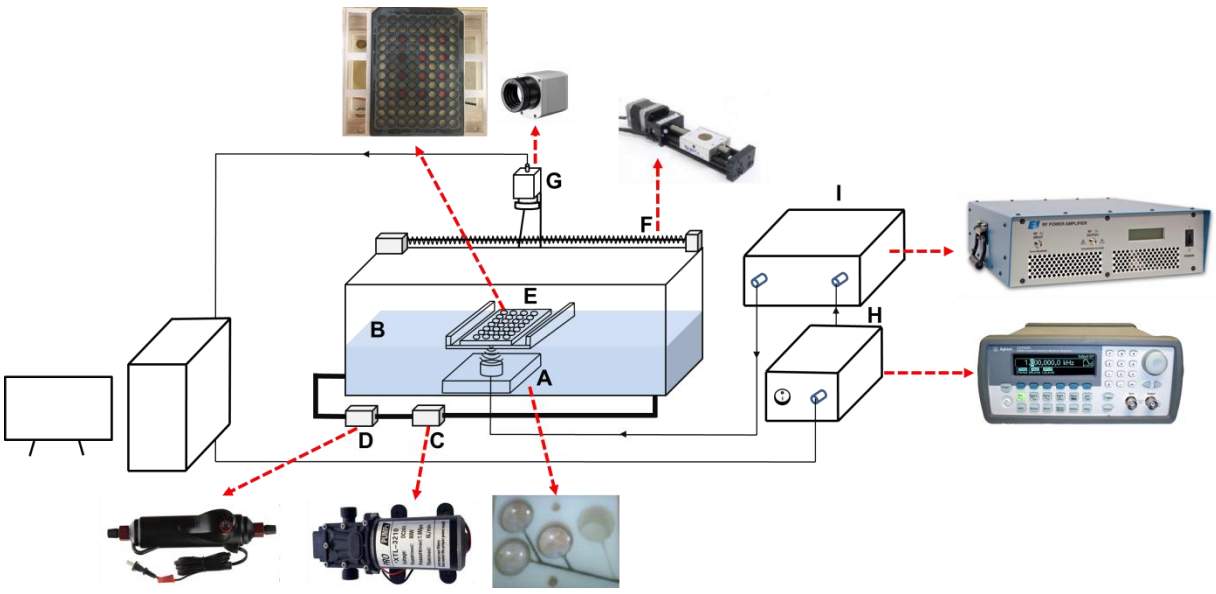

Figure 9: Schematic drawing of the *in vitro* FUS apparatus and pictures of its accessories. Piezoceramic bowl transducers were placed within a polyamide block (A) in a Perspex® water bath filled with degassed water (B); a self-priming water pump (C) was used to circulate the water; an external heater (D) kept the water temperature at 34 °C; a 96-well plate sealed with Titer Tops® film (E); the linear stage was driven by a stepper motor (F) to move the plate holder (E); an infrared thermal camera (G) used to

monitor the temperature of wells; the signal generator (H); the RF power amplifier (I).

The input commands for the linear stage as well as the sonication parameters defined by the waveform generator, including exposure duration, peak-to-peak output voltage (V*pp*) amplitude, frequency and position of transducers, were provided through a user-friendly interface (Figure 10) implemented in LabVIEW, which was also able to monitor and control the real-time temperature via readout of the infrared camera inside the wells.

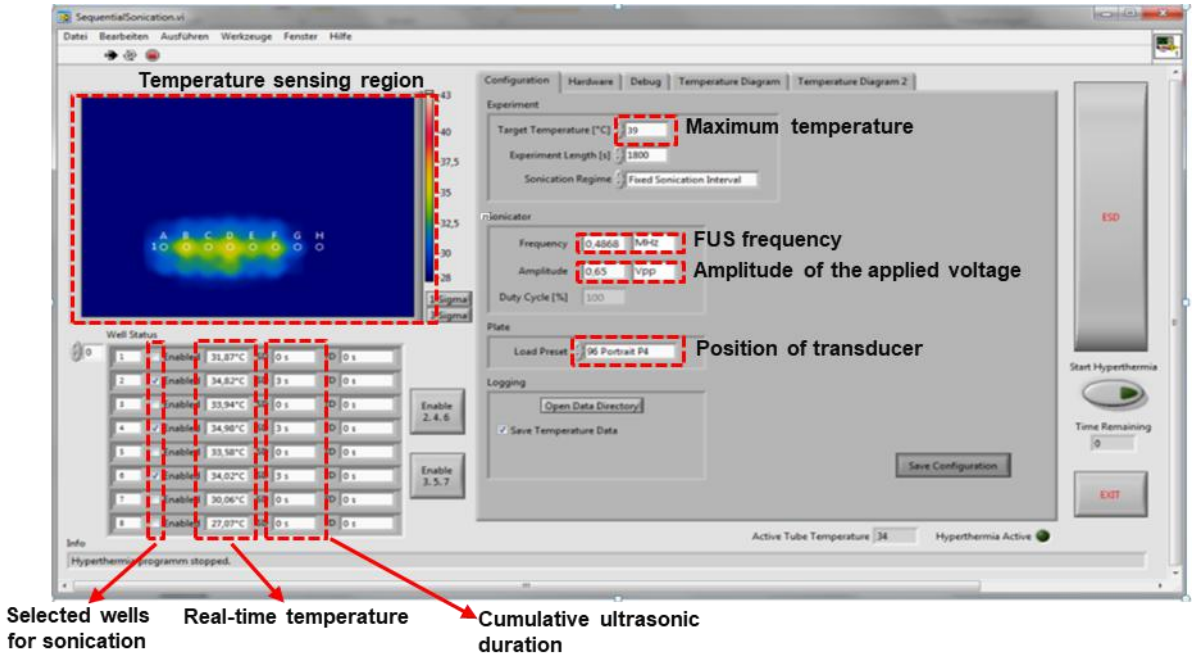

Figure 10: LabVIEW interface allows control of setting maximum temperatures inside wells and acoustic parameters at the focal spot. The thermal images and real-time temperatures of the sonicated wells were displayed in this interface; the amplitude of V*pp,* wave frequency, exposure duration and position of transducers were set for sonication; a sequence of individually chosen wells (out of 8 wells in each column) in a plate was selected for sonication.

6.2.2 Physical characterization of the *in vitro* FUS system

6.2.2.1 Setup of fiber-optic hydrophone system to characterize the FUS apparatus

The fiber-optic hydrophone (FOH) system (Figure 11B) was adopted to measure the acoustic pressure in the focal spot of the FUS acoustic field with a connection to an oscilloscope (Figure 11C). Ultrasound penetrable 96-well µ-clear cell culture plates were used to characterize the system and for *in vitro* treatment of cells. The acoustic pressure can induce changes in the thickness of thin polymer film. The

FOH system detected the optical thickness changes of the thin polymer film at the tip of the optical fiber sensor (Figure 11A). The sensitivities of the applied FOH system were 126 mV/MPa at 0.487 MHz, 121 mV/MPa at 1.142 MHz and 138 mV/MPa at 1.467 MHz based on the specification of manufacture. The detected signals were collected and digitized by an oscilloscope which was controlled by LabVIEW, and the data were analyzed using MATLAB.

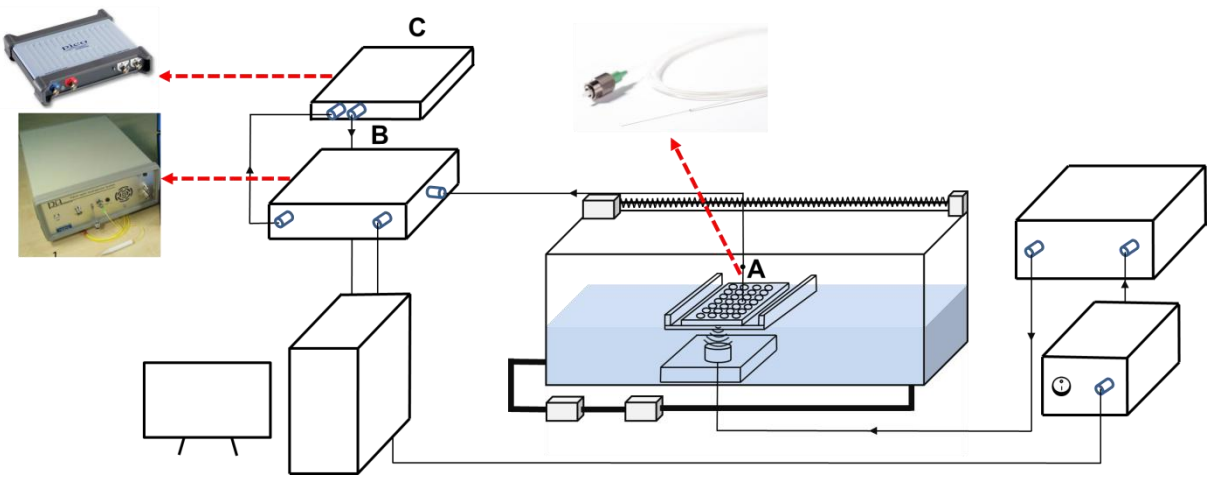

Figure 11: Schematic drawing of acoustic pressure/cavitation measurement with a FOH system. A 96-well plate filled with water was immersed in the water bath, the FOH sensor (A) was placed close to the bottom of the plate at the focal point, acquiring the acoustic pressure/cavitation signals to FOH system (B), and the collecting data was digitized by an oscilloscope (C).

Up to 420 µL/well of Milli-Q deionized water was added in each well of a 96-well µ-clear cell culture plate, and the plates were sealed with plate-sized Titer Tops® ultrasound transparent films to prevent bubbles (Figure 12A). The FOH sensor was positioned in the focal spot that was exactly at the bottom of the 96-well plate (Figure 12B). In order to reduce the interference of temperature rise on the acoustic pressure at the measuring spot, a short FUS burst of 1 ms in continuous ultrasound mode (containing averaging 400 – 1500-cycle sine-wave) was collected to plot the pressure waveforms for three transducers (Canney, Bailey, Crum, Khokhlova, & Sapozhnikov, 2008; Zhou, Zhai, Simmons, & Zhong, 2006). The V*pp* amplitude from the FUS signal generator was set in the range of 110 – 720 mV.

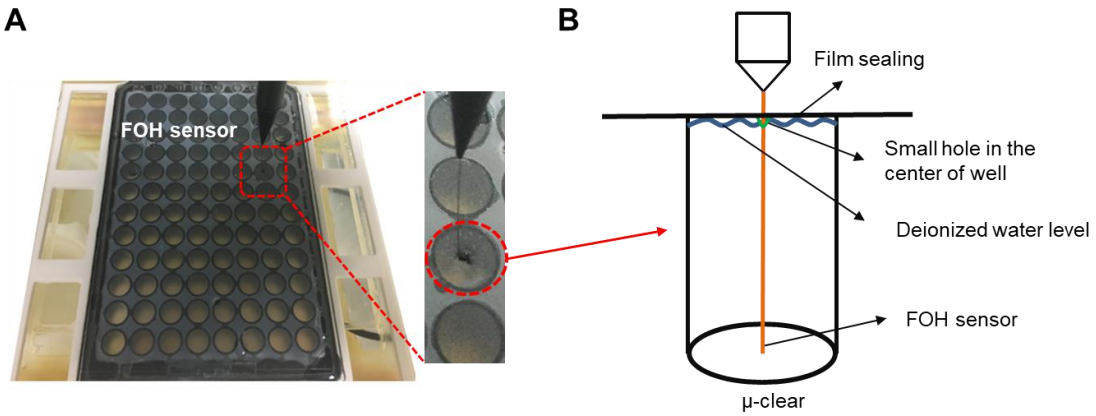

Figure 12: Characterization of the FUS *in vitro* system with a FOH system. (A) A FOH sensor was positioned at the bottom of a 96-well µ-clear plate filled with 420 µL Milli-Q water to measure the acoustic pressure signal of the focal spot during sonication. (B) Illustration of the position of the FOH sensor inside the well.

6.2.2.2 Data analysis in MATLAB

Following the measurements, the waveforms of acoustic compressional/rarefactional pressure (Figure 13A) were plotted based on Equation 1 (Bull, Civale, Rivens, & Ter Haar, 2013),

$$p = \frac{V}{M(f)}$$

Equation 1: Calculation of acoustic pressure (p) based on the raw voltage output of hydrophone

Where p is the time-varying acoustic pressure, V is the measured voltage with the hydrophone, and M (f) is the sensitivity of the hydrophone as a function of frequency (126 mV/MPa at 0.487 MHz, 121 mV/MPa at 1.142 MHz and 138 mV/MPa at 1.467 MHz). Temporal-peak negative pressure (*PNP*) was defined as the largest negative pressure excursion at any time in the short FUS burst (Figure 13A) (Salvesen, 2002). The waveforms of acoustic intensity (Figure 13B) were plotted based on Equation 2 (Afadzi et al., 2012; Hong et al., 2018),

$$\mathrm{I} = \frac{p^2}{Z}$$

Equation 2: Calculation of acoustic intensity

Where I is the time-varying acoustic intensity, Z (Pa • s/m) = ρ × c, is the acoustic impedance of the

medium, ρ (kg/m^3) is the density of the medium, and c is the speed of sound in that medium. The temporal-peak acoustic intensity (I_{TP}) was defined as the greatest acoustic intensity at any time in the short FUS burst (Figure 13B) (Barnett & Kossoff, 1984). Fast Fourier transformation (FFT) was used on the recorded waveform to determine its fundamental frequency and harmonics. Based on the measured *PNP*, the mechanical index (MI) of the FUS transducers was calculated. All the plots and calculations were conducted in MATLAB.

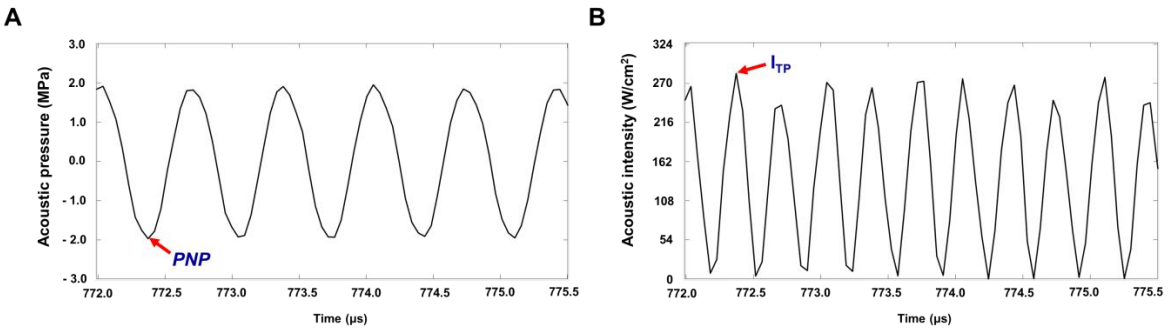

Figure 13: A typical drawing of the waveforms showing the peak negative pressure and time-varying acoustic intensity of a short FUS burst. (A) The output voltage signals of the FOH system were converted to acoustic pressure (Mpa), and the time-varying acoustic pressure was plotted in MATLAB. Peak negative pressure (*PNP*) was defined as the maximum pressure amplitude of the negative pulse at any time in the short FUS. (B) Time-varying acoustic intensity (W/cm^2) was plotted in MATLAB based on Equation 2, and temporal-peak acoustic intensity (I_{TP}) was defined as the greatest intensity amplitude at any time in the short FUS.

Mechanical index (MI) was developed to evaluate the likelihood of collapse cavitation occurring, which was expressed in Equation 3 (Husseini & Pitt, 2008),

$$\mathrm{MI} = \frac{PNP}{\sqrt{f}}$$

Equation 3: Calculation of mechanical index (MI)

Where *PNP* is peak negative pressure amplitude, *f* is the frequency of the applied transducer.

6.2.3 Cavitation measurement with FOH system

To measure the occurrence of cavitation inside of the μ-clear cell culture plates and to define the FUS intensity threshold for further treatment of cells, the sensor of the FOH system (Figure 11) was positioned

in the focal spot at the bottom of the wells filled with 420 µL Milli-Q deionized water and sealed by Titer Tops® films according to the transducer characterization described above (Figure 12). Measurements in cell culture medium were not performed because pre-tests showed cavitation dose measured in cell culture medium with the FOH system was the same as the result measured in deionized water. The V*pp* amplitude from the FUS signal generator was set in the range of 110 – 720 mV, and the sonication duration was 40 s. A set of 67,000,000 samples at a sampling rate of 20 MS/s (mega-samples per second) was acquired synchronously to the sonication. The data were processed by 1) splitting the binary data of each signal into 625 segments per second, 2) FFT of each segment, and 3) calculating the total root mean square (RMS) voltage of the signal over a chosen range of frequencies at a single time point (RMS voltage$_{t)}$. Stable cavitation was defined based on the sub- and ultra-harmonic signals (m/2*f_0, f_0: fundamental frequency, m =1, 3, 5, 7…) in the frequency spectrum (Lin et al., 2017; S. Y. Wu et al., 2014). A bandwidth of ± 20 kHz of sub- and ultra-harmonics was chosen as the frequency range for the calculation of the RMS voltage$_t$. The inertial cavitation was defined based on the frequency spectrum after excluding the fundamental waves and harmonics, sub- and ultra-harmonic signals. The RMS voltage$_t$ was plotted as a function of sonication time. The cavitation dose for each single period of 2.9 s was defined as the integral of RMS voltage$_t$ over time with baseline noise removed (Equation 4) (Lin et al., 2017; S. Y. Wu et al., 2014):

$$\text{Cavitation dose (2.9 s)} = \sum_{t=0\text{-}T} \text{dRMS voltage}_t\,(\text{FUS}) \; - \; \sum_{t=0\text{-}T} \text{dRMS voltage}_t\,(\text{Background noise})$$

Equation 4: Calculation of cavitation dose

Where t is the time for each sonication segment (1.6 ms); T is one period of sonication duration (2.9 s); the RMS voltage$_t$ is the cavitation level of one sonication segment for 1.6 ms. Due to the limited storage of the oscilloscope, the total cavitation dose for 40 s was measured as a sum up of 14 consecutive FUS periods of 2.9 s.

6.2.4 Chemical cavitation measurement with terephthalic acid (TA)

To validate the measurement result of the FOH system, the inertial cavitation dose was measured in the 96-well µ-clear plate format via a chemical method using TA according to the procedure of Barati et al. (Barati, Mokhtari-Dizaji, Mozdarani, Bathaie, & Hassan, 2007). Sonication protocols were the same as

described above (Materials and methods 6.2.3). The 2 mM TA solution was prepared by dissolving 0.0831 g TA powder and 0.05 g sodium hydroxide (NaOH) with 250 mL pre-warmed PBS. Up to 420 µL/well of this TA/NaOH mixture was added in the wells and sealed with Titer Tops® films, avoiding air bubble formation. During sonication, inertial cavitation generated ·OH free radicals from the breakdown of water and other molecules. Simplified equations for the generation of ·OH free radicals by inertial cavitation in water are shown in Figure 14A. After the sonication, the plate was incubated at room temperature for 3 h where TA reacted with ·OH free radicals generated by inertial cavitation to produce 2-hydroxyterephthalic (HTA) (Figure 14B), which can be detected using a microplate reader with excitation/emission wavelengths at 310/425 nm. After sonication, 200 µL of FUS irradiated TA solution was transferred from the treated plate to a new black 96-well plate, and fluorescence intensity was assessed by a microplate reader with excitation/emission wavelengths at 310/425 nm. The un-irradiated TA solution was set as background control. The fluorescence value, which subtracted the background control, was used to indicate the inertial cavitation dose. All experimental procedure was performed in darkness.

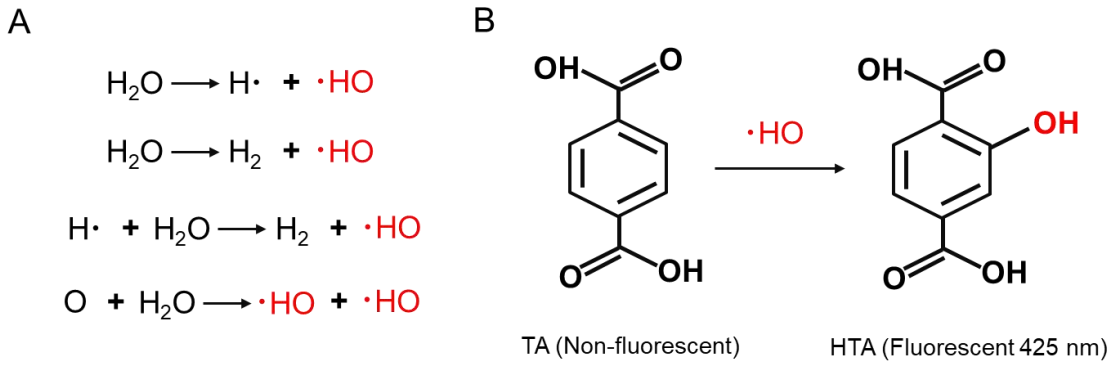

Figure 14: Simplified equations for the generation of (A) ·OH free radicals from the breakdown of water induced by inertial cavitation and (B) HTA converted from the reaction of TA with ·OH free radicals. Adapted from (Villeneuve, Alberti, Steghens, Lancelin, & Mestas, 2009).

6.2.5 Culture of human cancer cell lines

The prostate cancer cell lines PC-3 and LNCap, glioblastoma cell line T98G, and head and neck cancer cell line FaDu were selected for FUS sonication experiments. Cells were cultured in the corresponding complete medium described in Table 7. All cultures were maintained at 37 °C in a humidified air with 5 % (v/v) CO_2.

Table 7: *In vitro* cell culture medium and supplementary

Cell lines	Complete medium	
	Medium	Supplementary
PC-3	Ham's F-12K (Kaighn's)-Medium	[+] 10 % FBS [+] 100 U/mL penicillin [+] 100 mg/mL streptomycin
LNCap	RPMI Medium 1640 (1×)	[+] 10 % FBS [+] 100 U/mL penicillin [+] 100 mg/mL streptomycin
T98G	Dulbecco's Modified Eagle Medium (DMEM)	[+] 10 % FBS [+] 100 U/mL penicillin [+] 100 mg/mL streptomycin
FaDu	Dulbecco's Modified Eagle Medium (DMEM)	[+] 2 % HEPES [+] 1 % Sodium Pyruvate [+] 1 % MEM non-essential amino acids [+] 10 % FBS [+] 100 U/mL penicillin [+] 100 mg/mL streptomycin

Confluent monolayers of cancer cells cultivated in T25/75/175 plastic flasks were dispersed with 1/2.5/4 mL Trypsin/EDTA (1×), detached cells were collected with complete medium to screw-cap tubes. The cell suspension was centrifuged at 300 × g for 5 min, and then the supernatant was decanted. Cell pellets were resuspended with complete medium, and approximately 15 µL cell suspension was pipetted for living cell staining with trypan blue solution. Cell counting was performed using a hemocytometer under the microscope with 100-fold magnification. The cells were seeded into new flasks at the density of 1×10^5 /mL – 3×10^5 /mL and left undisturbed for 24 – 36 h in the incubator to facilitate cell attachment. Adherent cells were cultured and passaged every 3 – 5 days. Cells were harvested from plastic flasks and seeded evenly in 96-well plates for experiments. To reach 80 – 100 % confluency of cells in 96-well plates at desired endpoint day after treatments, cell seeding number per well for the different cell lines is shown in Table 8.

Table 8: Cell seeding number per well in a 96-well plate for different cell lines

Cell line	Cell seeding number per well
PC-3	600 – 10000
LNCap	2000– 15000
T98G	8000
FaDu	5000 – 8000

6.2.6 FUS treatment of cancer cells

Cancer cells were harvested from the flasks and seeded in ultrasound penetrable 96-well plates with the µ-clear bottom in 100 µL corresponding complete medium. The seeding was performed 24 – 48 h prior to treatment. Due to loose adherence, the 96-well plates for culturing of LNCap cells were coated with 40 µL/cm^2 poly-L-lysine solutions for 30 min at 37 °C, and washed twice with distilled water (Song & Khera, 2014). Poly-L-lysine pre-coated plates were used to improve the adherence of LNCap cells. Before sonication, up to 420 µL/well of cell culture medium was added in wells (with cells) and PBS was added in the remaining wells (without cells) (Figure 15A). The selected wells for sonication were separated by one well without cells to avoid thermal diffusion from the sonicated wells to neighboring wells (Figure 15A). The plate was sealed with Titer Tops® film (plate-sized US-transparent films, Figure 15A) to keep sterilization of cells, carefully avoiding air bubble formation. Afterwards, the plate was immersed in a water bath in the FUS system for sonication as shown in Figure 15B.

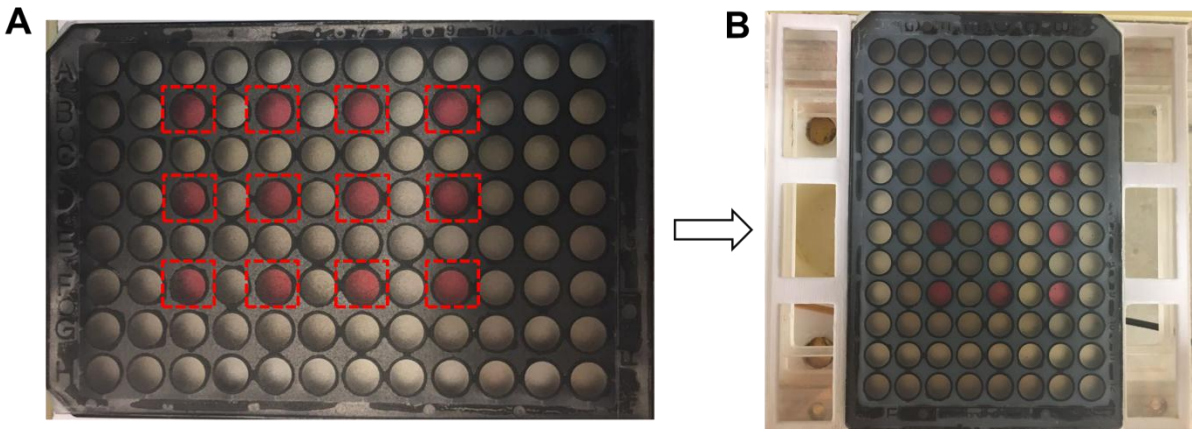

Figure 15: The 96-well plate with µ-clear bottom was prepared for sonication. (A) The 96-well plate full-filled with cell culture medium and PBS, sealed with a Titer Tops® film without air bubbles, the red dashed box indicates the wells for sonication; (B) The 96-well plate was fixed in sonicator by a plate holder located above the FUS transducers.

To investigate the effects of FUS-induced cavitation to support water bath hyperthermia (HT) or radiation therapy, two different treatment protocols of FUS with the 1.467 MHz transducer were conducted on monolayer cells in 96-well plates as follow: (1) short FUS treatment (FUS) with an acoustic intensity of 129 W/cm^2 and an active sonication duration of 40 s. (2) FUS-induced cavitation (FUS-Cav) with acoustic intensity at 1136 W/cm^2 and an active sonication duration of 40 s. In order to avoid the interference of the acoustic waves, three nonadjacent wells in one column (Figure 15A) were selected for segmental sonication, the real-time temperatures inside wells were monitored by the thermal camera. When the temperature in the well reached 39 °C, the sonication programmatically stopped until the temperature decreased to 34 °C. Duration and the temperature curves of the two FUS treatments were shown in Figure 16. To control the temperatures in a specific range and make the results comparable, the cells were exposed to ultrasound at different intensities in on/off mode with the same sonication duration of 40 s in FUS and FUS-Cav treatments. The temperature curves (Figure 16) illustrate the different heating profiles at two intensities. The temperature fluctuation was observed in both FUS and FUS-Cav treatments. The temperature increased to 39 °C when sonication was activated, and then sonication was deactivated and resulted in a temperature decrease to 34 °C. For FUS treatment at the acoustic intensity of 129 W/cm^2, the active sonication duration of each cycle is 2.43 s and the whole treatment duration is 73.7 s with the mean temperature of 36.99 ± 1.67 °C. While in FUS-Cav treatment at the intensity of 1136 W/cm^2, the active sonication duration of each cycle is 0.86 s and the treatment duration is 126.7 s with the temperature of

36.50 ± 1.53 °C. After sonication, the medium was aspirated and refilled with 100 µL/well fresh cell culture medium. Cells were observed under a microscope to check adherence.

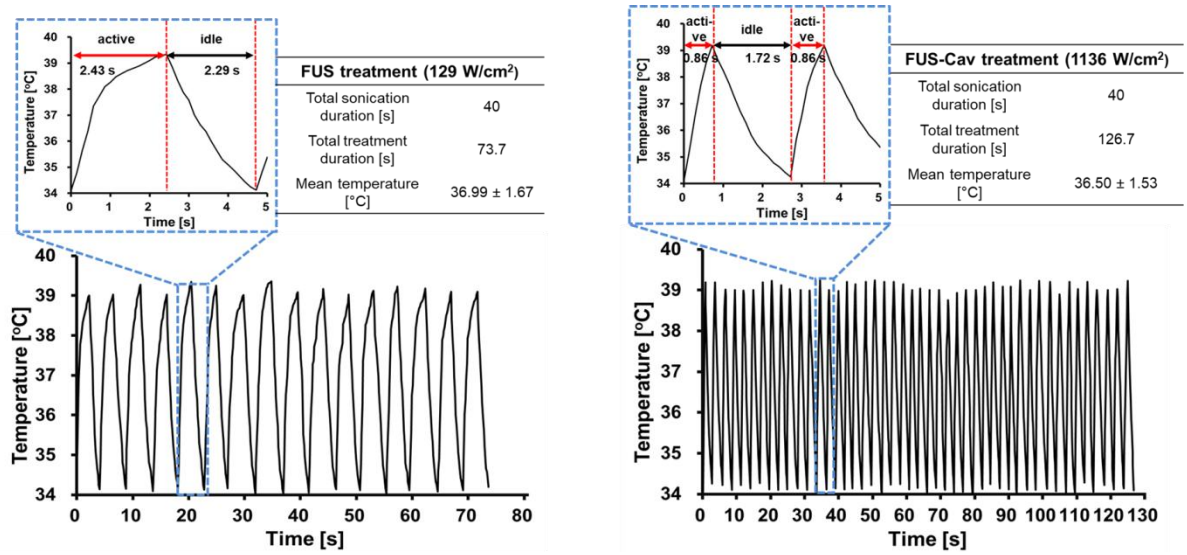

Figure 16: Temperature curves showing the pattern of sectional sonication. The diagram demonstrates the active sonication duration (red arrows) and idle (black arrows) duration in each cycle of sectional sonication. The mean temperatures of FUS and FUS-Cav treatments are 36.99 ± 1.67 °C and 36.50 ± 1.53 °C. The total treatment durations of FUS and FUS-Cav are 73.7 s and 126.7 s, respectively.

6.2.7 Water bath hyperthermia treatment

In order to compare the effects of heating versus FUS mechanical effects in radio-sensitization and to investigate the effects of FUS-induced cavitation to support water bath HT, cancer cells were treated with conventional hyperthermia in a water bath. Cells were seeded in ultrasound penetrable 96-well plates with µ-clear bottom as described above (Materials and methods 6.2.5). To maintain the sterile environment and prevent evaporation of the cell culture medium, 96-well plates were sealed with Titer Tops® films before water bath HT treatment and then carefully placed in a pre-warmed water bath. Type T PTFE-insulated Copper-Constantan precision fine wire thermocouples (diameter 0.07 mm) were used to measure the temperature inside two reference wells (Figure 17A), and a Pico data logger was used to record real-time temperature and collect data. According to the literature (Cihoric et al., 2015) and preliminary experiments, water bath HT treatment was performed at the temperature of 45 °C for 30 min. The temperature curves of the water bath HT treatment were shown in Figure 17B. After treatment, the medium was aspirated and refilled with 100 µL/well fresh cell culture medium. Cells were observed under a microscope to check

adherence.

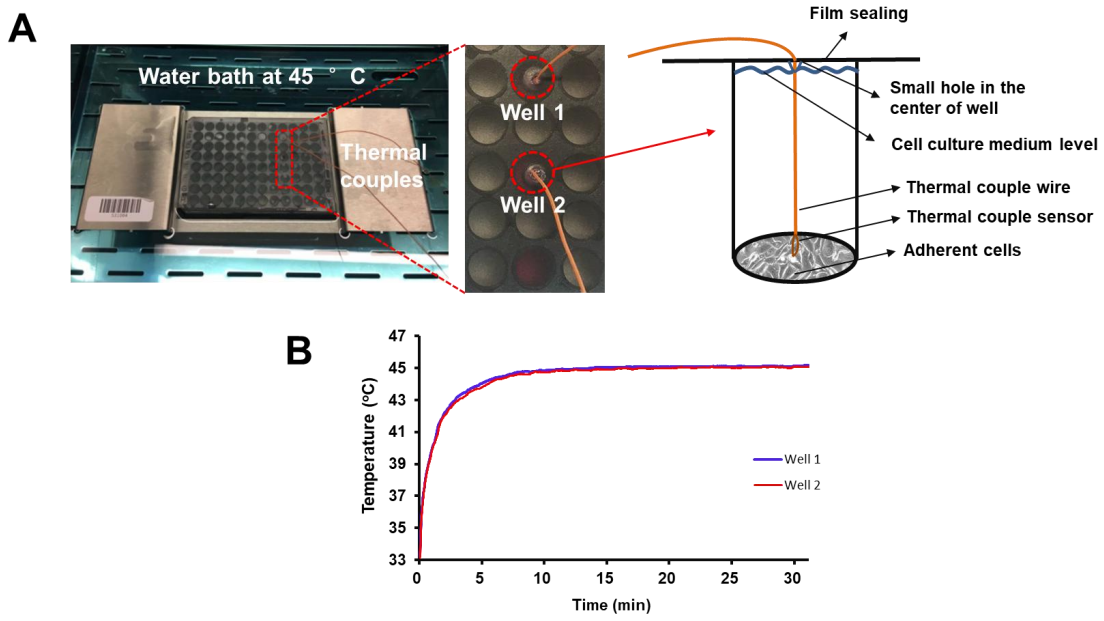

Figure 17: Experimental setup of water bath hyperthermia with 96-well plate at 45 °C. (A) The real-time temperatures in two reference wells were measured with inserted thermal couples close to monolayer cells. (B) Temperature curves in two reference wells.

6.2.8 Radiation therapy *in vitro*

Cancer cells cultured in 96-well plates were irradiated with a single dose using a 150 kV X-ray machine at a dose rate of 1.276 Gy/min. According to preliminary experiments performed at the University hospital Leipzig by Xinrui Zhang, a single dose at 5 and10 Gy was used in the combination experiments.

6.2.9 The protocol of FUS\FUS-Cav combined with RT or HT

Cancer cells were seeded in 96-well plates as described in Materials and methods 6.2.5, and the monolayer of cells was formed after 24 – 48 h of cell culture. To investigate the additive effects of FUS/FUS-Cav as an adjuvant therapy on RT, the cancer cells were firstly exposed with FUS/FUS-Cav according to the single FUS treatment protocols (as described in Materials and methods 6.2.6), and the water bath HT treatment was performed as a reference group. RT treatment was carried with an interval of 60 min following single FUS/FUS-Cav or HT treatment. In order to examine the additive effects of FUS/FUS-Cav to HT, water bath HT treatment was performed 60 min after FUS/FUS-Cav. The short-term effects of the

combination treatment were assessed via the measurement of cell invasion and metabolic activity 48 h after treatments. The long-term effects were evaluated by determining the cell clonogenic survival 14 – 21 days post-treatments.

6.2.10 Evaluation of cell ability to reproduce with clonogenic assay

To examine the reproductive ability of a single cell in the long-term after different treatment regimes, clonogenic assay was performed according to the procedure reported by Franken et al. (Franken, Rodermond, Stap, Haveman, & van Bree, 2006). Briefly, cells were treated in ultrasound penetrable 96-well plates with µ-clear bottom as described above (Materials and methods 6.2.9). Cell suspensions were harvested from 96-well plates with 100 µL trypsin/EDTA (1×) per well immediately after treatment and were seeded with a density of 200 – 17,000 cells/well into 6-well plates in triplicates. Seeding densities were adjusted as Table 9 to yield proper colony numbers in each well for different treatments. The 6-well plates were incubated for 14 or 21 days (Table 9) to allow colony formation, while the cell culture medium was changed twice per week. Colonies were gently rinsed with PBS twice before fixation with ice-cold methanol/acetone (1:1, V/V) for 5 min, afterwards stained with 0.5 % crystal violet solution in water for 30 min at room temperature and washed with deionized water to remove the unbound stain. Colonies in dried plates were scored if they exceeded a threshold number of 50 cells.

Table 9: Scheme for seeding cells and incubation for the clonogenic assay in three cancer cell lines

Different treatments and incubation time	Seeding densities of different cell lines (cells/well)		
	PC-3	T98G	FaDu
Incubation time	21 days	21 days	14 days
Untreated groups	250	250	250
FUS	250	250	250
FUS-Cav	250	250	250
Water bath HT	250	250	1000
FUS + Water bath HT	250	250	1000

FUS-Cav + Water bath HT	250	250	1000
RT (5 Gy)	5000	1000	3000
RT (10 Gy)	8000	10000	10000
FUS + RT (5 Gy)	5000	1000	3000
FUS + RT (10 Gy)	13000	10000	14000
FUS-Cav + RT (5 Gy)	5000	1000	3000
FUS-Cav + RT (10 Gy)	17000	10000	12000
Water bath HT+ RT (5 Gy)	5000	1000	3000
Water bath HT+ RT (10 Gy)	8000	10000	15000

The plating efficiency (PE) is defined as the number of scored colonies in untreated groups divided by the number of cells seeded (Equation 5) (Young & Bennewith, 2017):

$$\mathrm{PE} = \frac{\text{no. of colonies formed}}{\text{no. of cells seeded}} \times 100\ \%$$

Equation 5: Calculation of plating efficiency

The number of colonies that arised after treatment of cells, expressed in terms of PE as Equation 6, is called the survival fraction (SF) (Young & Bennewith, 2017):

$$\mathrm{SF} = \frac{\text{no. of colonies formed after treatment}}{\text{no. of cells seeded in treated groups} \times \mathrm{PE}} \times 100\ \%$$

Equation 6: Calculation of survival fraction

6.2.11 Measurement of cellular metabolic activity with WST-1 assay

To determine the short-term impacts of the different treatments on the cellular metabolic activity of the

human prostate cancer cell line PC-3, the tetrazolium salt-based WST-1assay was performed 48 h after treatments. The cellular enzyme of mitochondrial dehydrogenases cleaved WST-1 reagent (tetrazolium salt) to formazan dye in the sample, quantification of formazan dye was directly correlated to the number of metabolically active cells in the culture medium. According to the manufactures' instructions, the culture medium was discarded, and cells were incubated with 100 µL fresh cell culture medium containing WST-1 reagent (final concentration of 10 %) in the 96-well plates at 37 °C for 30 min. The absorbance of the formazan product was measured at 435 nm with a reference wavelength of 680 nm using a microplate reader. All data were normalized to untreated control which was set as 100 %.

6.2.12 Evaluation of cell invasion ability with Transwell® assay

The cell invasion ability of prostate cancer PC-3 cells was assessed by the *in vitro* Transwell® invasion assay. The Transwell® chamber system composed of Transwell® inserts mounted on a 24-well plate, the upper and lower chambers were divided by the polycarbonate porous membrane pre-coated with 100 µg/cm^2 matrigel at 37 °C for 4 h. The PC-3 cells were harvested from 96-well plates immediately after treatments. Approximately 1 × 10^5 cells were resuspended with 100 µL serum-free cell culture medium and seeded in the upper Transwell® chamber (Figure 18A). 600 µL culture medium supplemented with 10 % FBS was added served as a source of chemo-attractants in the lower chamber. The 24-well plate mounted with Transwell® inserts was incubated at 37 °C for 48 h. After incubation, the non-invaded cells on the upper surface of the membrane were removed with a sterile cotton swab, and the invaded cells at the lower surface of the polycarbonate porous membrane (Figure 18B) were fixed with 600 µL methanol added in another lower chamber and stained with 0.1 % crystal violet at ambient temperature for 15 min. Invaded cells were observed under a microscope, bright images of 5 random fields were taken at 200-fold magnification in each Transwell® insert and cells were counted using Image J software. All data were normalized to untreated control which was set to 100 %.

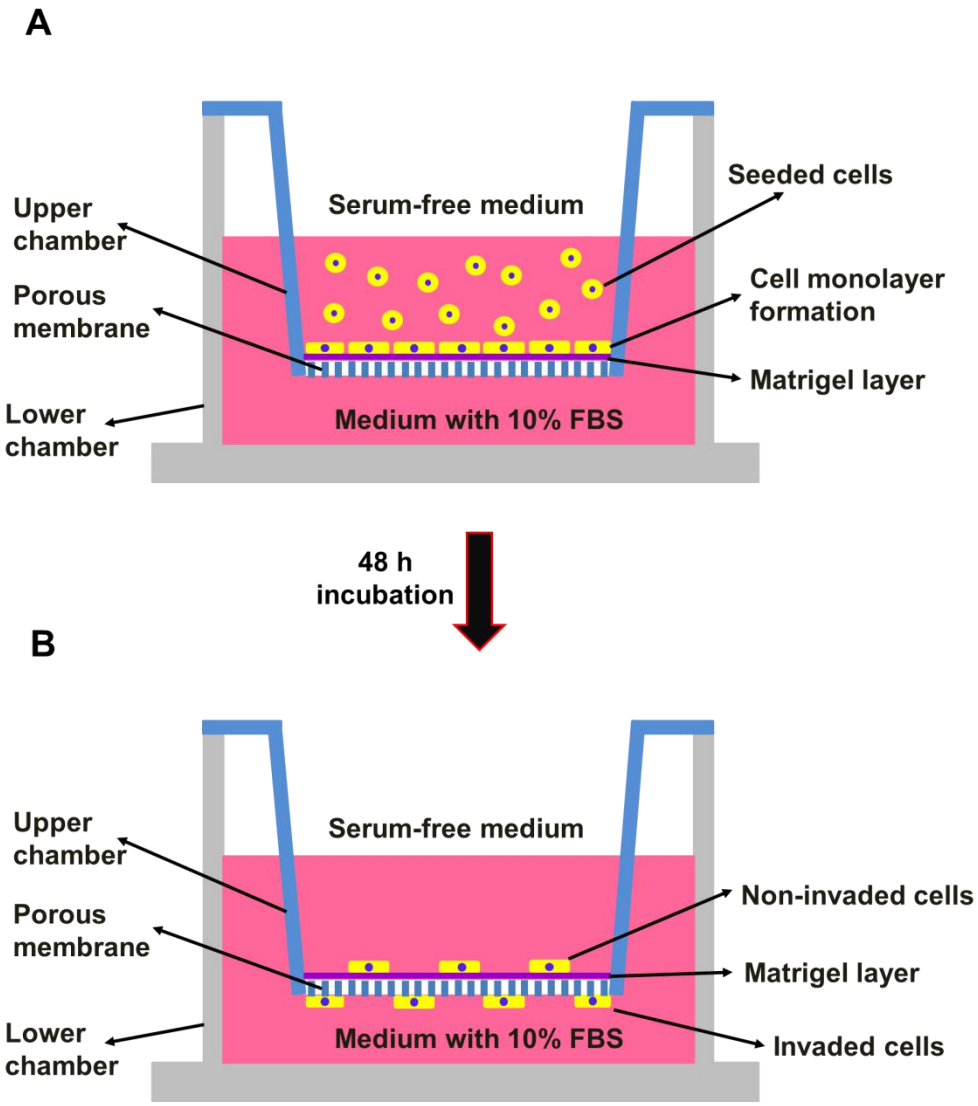

Figure 18: Schematic illustration of *in vitro* Transwell® invasion chamber assay. (A) Cell suspension with the serum-free medium was seeded in the Transwell® insert; (B) Invaded cells migrated through the matrigel layer and porous membrane to attach at the lower surface of porous membrane; non-invaded cells attached at the upper layer of the porous membrane after 48 h incubation. Adapted from (S. Yu et al., 2013).

6.2.13 Detection of sonoporation by cell staining with propidium iodide (PI)

Sonoporation is defined as the changes in cell membrane permeability generally induced by stable cavitation (Qin, Wang, & Willmann, 2016). To investigate this phenomenon on cells, PI was employed as a cell membrane integrity probe that cannot penetrate through intact cell membranes of living cells (van Wamel et al., 2006). CellMask™ Green Plasma Membrane Stain was used for visualization of the cell membrane. Cells were seeded in ultrasound penetrable 96-well plates with µ-clear bottom at a density of

5,000 cells/well 24 h prior to treatments. FUS/FUS-Cav treatment with the sonication duration of 40 s was conducted as described above (Materials and methods 6.2.6), and cells were washed gently with 100 µL PBS. PI at a final concentration of 1 µg/mL and CellMask™ at a final concentration of 5 µg/mL were added in cell culture medium before or 30 min after sonication of the cells. The PI was immediately visualized at excitation/emission at 535/617 nm, and cell plasma membrane stained with CellMask™ was observed at ex 522/em 535 nm using a fluorescence microscope and ZEN 2.3 software. Since the dimension of the focal field covered one well of the 96-well plate, the fluorescent images of 5 random fields were taken at 200-fold magnification in each well and cells were counted. The cells stained with PI and CellMask™ were counted to quantify the percentage of PI-positive cells.

6.2.14 Detection of SRD5A as a therapeutic target for prostate cancer with immunofluorescence microscopy

According to the literature (Liu & Yamauchi, 2008) and preliminary experiments, the prostate cancer cell lines PC-3 and LNCap in the 96-well µ-clear plate were incubated for 24 h after treatments as described in Materials and methods 6.2.9. Cells in a 96-well plate were fixed with 100 µL/well of 4 % formaldehyde in PBS for 15 min on ice, and then cells were permeabilized with 0.1 % Triton ® X-100 in PBS for 10 min. Non-specific bindings of antibodies were blocked with blocking buffer (4 % FBS in PBS) at room temperature for 1 h. Cells were incubated overnight with blocking buffer containing 2 µg/mL 5α-reductase-1 primary antibody (Anti-SRD5A1 antibody produced in rabbit) or 5-reductase-3 primary antibody (Anti-SRD5A3 antibody produced in rabbit) at 4 ˚C. After washing four times with PBS, cells were incubated with 2 µg/mL secondary antibodies (Anti-Rabbit IgG (H+L), F(ab')2 Fragment (Alexa Fluor® 594 Conjugate)) in blocking buffer for 3 h at room temperature in the dark. The secondary antibody was removed, and the cell nuclei were stained with the nuclear stain 4, 6-diamidino-2-phenylindole (DAPI) for 5 min. Immunofluorescence in the absence of primary antibodies was used as the negative control. The expressions of SRD5A1 and SRD5A3 proteins labeled by Alexa Fluor® 594 were visualized at ex 561/em 594 nm and cell nuclei stained by DAPI at ex 358/em 461 nm using a fluorescence microscope with 400-fold magnification.

6.2.15 Quantification for the reduction of SRD5A proteins with flow cytometry

Flow cytometry was performed to quantify the SRD5A positive cells. PC-3 and LNCap cells were seeded and treated as described above (Materials and methods 6.2.5 and 6.2.9). Cell suspensions were harvested in the 1.5 mL microtube from 96-well plate 24 h incubation after treatments. Cell supernatants were discarded after centrifuging at 2000 rpm, 5 min. The cells were fixed on ice with 4 % formaldehyde solution in PBS for 15 min and permeabilized with 0.1 % Triton ® X-100 in PBS for 10 min. Non-specific binding of antibodies was blocked with blocking buffer at room temperature for 1 h. The cells were incubated with 2 µg/mL 5α-reductase-1 primary antibody (Anti-SRD5A1 antibody produced in rabbit) or 5α-reductase-3 primary antibody (Anti-SRD5A3 antibody produced in rabbit) dissolved in blocking buffer overnight at 4 ˚C. Next, cells were washed four times with PBS and incubated with 2 µg/mL secondary antibodies (Anti-Rabbit IgG (H+L), F(ab')2 Fragment (Alexa Fluor® 594 Conjugate)) in blocking buffer for 3 h at room temperature in the dark. Samples without incubation of primary antibody were used as the background control, and cells with higher fluorescence intensity than the background group were the fluorescent dye positive cells, the percentage of which indicated the overall SRD5A level 24 h after all treatments. Cell doublets and debris were excluded from analysis using forward-scattered light (FSC) versus side-scattered light (SSC). Analysis of percent dye positive cells was performed on at least 20.000 single cells. All data were normalized to untreated control which was set to 100 %.

6.2.16 Testosterone treatment

Androgen-independent cell line PC-3 and androgen-dependent cell line LNCap were selected to investigate the long-term effects of various testosterone concentrations in prostate cancer cells *in vitro*. The cells were cultured as described method in Materials and methods 6.2.5. The testosterone solution at the concentration of 1 mg/mL was diluted with the corresponding cell culture medium to prepare stock solution at a 1 µg/mL concentration. The final concentrations of exogenous testosterone 1, 8, and 32 ng/mL were prepared in cell culture medium. LNCap at a density of 2000 cells/well and PC-3 at a density of 600 cells/well were seeded in ultrasound penetrable 96-well plates with µ-clear bottom to reach 80 – 100 % confluency at the desired time point after treatments. The 96-well plates pre-coated with Poly-L-lysine were used to improve the adherence of LNCap cells. Cell culture medium was removed 24 h after seeding,

fresh medium containing testosterone at a concentration of 1, 8 or 32 ng/mL was added. The cells were incubated at 37 °C for 8 – 12 days, and the corresponding cell culture mediums with testosterone were changed every 2 days. Cells were observed under a microscope every day during the whole experiment, and images were taken at the experimental endpoint of day 12 for the LNCap cell line and day 8 for the PC-3 cell line due to different doubling times as described method in Materials and methods 6.2.5. WST-1 assay was performed to evaluate the metabolic activity of the cells at the experimental endpoint, and the results of the WST-1 assay performed at day 8 for PC-3 cells and day 12 for LNCap cells were normalized to untreated control set to 100 %.

6.2.17 FUS/FUS-Cav combined with testosterone treatment

FUS/FUS-Cav treatment was expected to create pores in the membrane of prostate cancer cells to facilitate testosterone uptake. Monolayer cells in 96-well plates were treated with FUS or FUS-Cav as described in Materials and methods 6.2.6, in the culture medium containing testosterone at the concentrations of 1, 8 or 32 ng/mL. After FUS or FUS-Cav treatment, 100 µL cell culture medium containing testosterone at the concentration of 1, 8 or 32 ng/mL replaced the old medium, afterwards cells were cultured at 37 °C for 8 – 12 days and the corresponding cell culture mediums with testosterone were changed every 2 days. At the experimental endpoint of day 12 for LNCap cells and day 8 for PC-3 cells, cell morphology changes were observed by transmitted microscopy images and cell relative metabolic activity was evaluated by WST-1 assay.

7 Results

7.1 Physical characterization of the *in vitro* FUS system

The short FUS bursts of 1 ms in continuous ultrasound mode (containing averaging 400 – 1500-cycle sine-wave) generated by three transducers were recorded to test acoustic frequencies and temporal-peak negative pressure (*PNP*) of FUS waves. The frequency spectrums (Figure 19) represent the frequency distribution and intensity of the acoustic wave at the focus spot, in which the dominant signals are the fundamental frequencies (f_0) symbolized by the peaks of 0.487 MHz, 1.142 MHz and 1.467 MHz marked with green arrows. Due to the nonlinear propagation of FUS waves in the acoustic field, the harmonics ($m*f_0$, m = 2, 3, 4…) also occur and are indicated by the peaks marked with purple arrows (Figure 19).

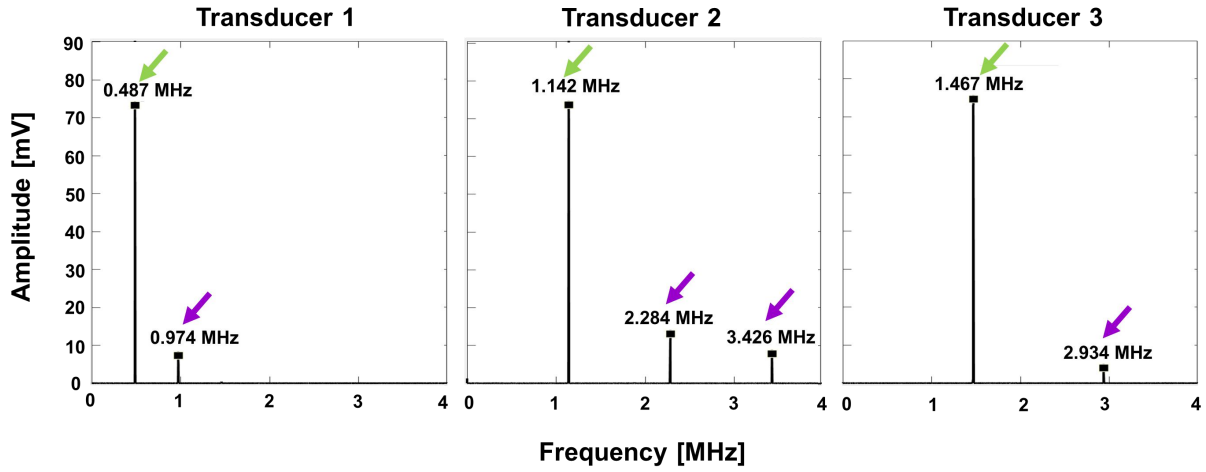

Figure 19: Frequency spectrums of the focal spot in acoustic fields generated by three transducers. The acoustic fundamental frequencies were measured as 0.487 MHz, 1.142 MHz and 1.467 MHz for three transducers; green arrows: FUS fundamental frequencies; purple arrows: harmonics generated by the nonlinear propagation of FUS waves.

To characterize the *PNP* in the focal spot, the output voltage signals of the FOH system for the short FUS burst (1 ms) were converted to acoustic pressure based on the frequency response. Figure 20A displays a representative waveform showing the time-varying acoustic compressional/rarefactional pressure of the short FUS burst, in which the maximum pressure amplitude of the negative pulse, i.e. the *PNP*, is marked by a red arrow. Figure 20B presents the time-varying acoustic intensity calculated based on acoustic pressure, in which the temporal-peak acoustic intensity (I_{TP}) is marked with a purple arrow. The mechanical index (MI), indicating the probability of mechanical effects, together with *PNP* and I_{TP} at

various peak-to-peak output voltages, are shown in Table 10 for all transducers.

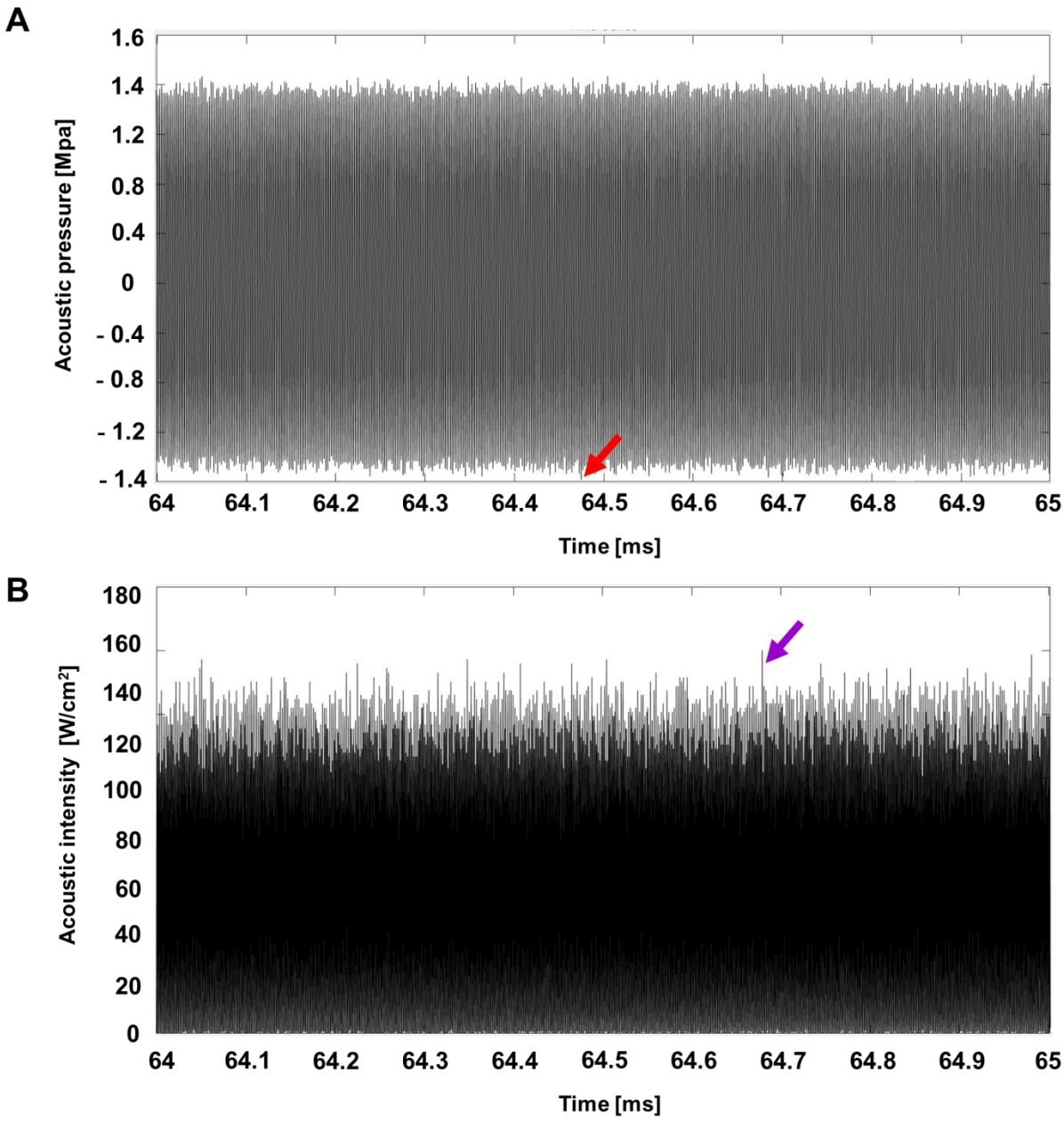

Figure 20: A representative output signal from the measurement of a short FUS burst by FOH. (A) Time-varying acoustic pressure (Mpa) of the short FUS burst; red arrow: the maximum pressure amplitude of the negative pulse indicating temporal-peak negative pressure (*PNP*). (B) Time-varying acoustic intensity (W/cm^2) of the short FUS burst; purple arrow: the maximum intensity amplitude was recognized as the temporal-peak acoustic intensity (I_{TP}).

Table 10: Temporal-peak acoustic intensity (I_{TP}), temporal-peak negative acoustic pressure (*PNP*) and mechanical index (MI) value at various peak-to-peak output voltages for the set of three transducers

Transducer frequency [MHz]	Peak-to-peak output voltage [mV]	Temporal-peak acoustic intensity [W/cm^2]	Temporal-peak negative acoustic pressure [Mpa]	Mechanical index
0.487	120	37.98	0.75	1.07
	300	124.49	1.36	1.95
	450	336.99	2.23	3.20
	600	625.82	3.04	4.36
	720	838.61	3.52	5.05
1.142	190	87.76	1.14	1.07
	260	213.10	1.78	1.67
	350	306.83	2.13	1.99
	430	522.10	2.78	2.60
	500	835.89	3.52	3.29
1.467	110	128.81	1.38	1.14
	200	344.03	2.26	1.86
	250	538.89	2.82	2.33
	350	1136.22	4.10	3.39
	420	1704.04	5.02	4.15

7.2 Cavitation occurs at a certain level of acoustic intensity

7.2.1 Characteristics of ultrasonic spectrograms

The time-domain spectrograms of the single period of 2.9 s FUS generated by three transducers at various acoustic intensities are exhibited in Figure 21A – C, which describe the variation of peak-to-peak acoustic amplitude as the function of time at the focal spot of the acoustic field. For each individual transducer with a specific frequency, the peak-to-peak acoustic amplitude increased with rising acoustic intensity. The locally enlarged graph of Figure 21A shows that the acoustic amplitude changes with time in the form of sine waves. The amplitude principally oscillates at the driving frequency of each transducer (f_0: fundamental frequency), and secondly, at the frequency of higher harmonics ($m * f_0$, m = 2, 3, 4, 5…).

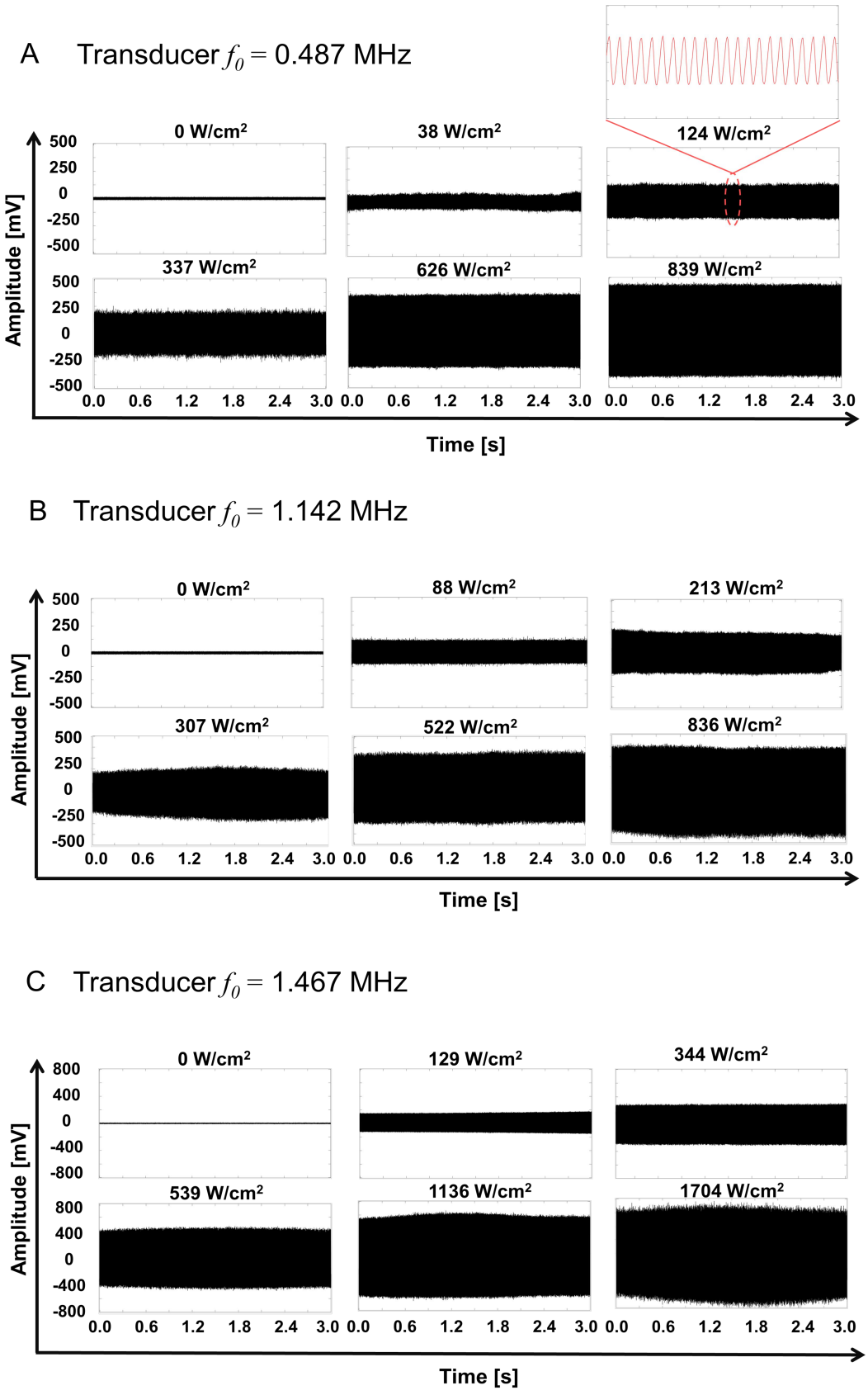

Figure 21: Acoustic signals in time-domain for one single period of 2.9 s FUS at (A) 0.487 MHz, (B) 1.142 MHz and (C) 1.467 MHz with various acoustic intensities. Raw data were obtained from FOH

measurement at a sampling rate of 20 MS/s.

To confirm the frequency distribution at the focal spot of the acoustic field, the acoustic signals in the time-domain were converted to the frequency-domain signals by FFT in MATLAB. Figure 22 shows frequency-domain spectrograms for all transducers, in which the separated peaks represent component frequencies in the focal spot of the acoustic field at various acoustic intensities. In the frequency domains, the predominant signals are the FUS fundamental frequencies (f_0) marked with green arrows and the higher harmonics ($m*f_0$, m = 2, 3, 4…) marked with purple arrows. These signals represent the linear (fundamental wave) and nonlinear (higher harmonics) propagation of ultrasonic waves at various acoustic frequencies and intensities. The sub- and ultra-harmonic signals ($m*f_0/2$, m =1, 3, 5, 7…) marked with blue arrows shown in Figure 22 are generally accepted as the frequencies of acoustic scattering from gas bubbles vibration related to stable cavitation. Broadband noise is defined as the spectrum that excludes fundamental, harmonic, sub- and ultra-harmonic frequency components and is broadly accepted as an indicator for inertial cavitation, marked with red arrows in Figure 22. In terms of characteristics of spectrograms, the stable cavitation indicated by sub- and ultra-harmonic signals belongs to the discrete spectrum (discrete peaks with gaps between them), which is effortless to be identified in the frequency domains. As noticed in the frequency domains of three transducers with various frequencies and acoustic intensities (Figure 22), sub- and ultra-harmonic signals (blue arrows) occur at and above 337 W/cm^2 for 0.487 MHz (Figure 22A), 213 W/cm^2 for 1.142 MHz (Figure 22B) and 344 W/ cm^2 for 1.467 MHz (Figure 22C), which indicate the occurrence of stable cavitation. The broadband noise is the continuous spectrum (continuous small peaks without gaps between them), which consists of numerous smoothly varying peaks and can be easily confused with the background baseline in the frequency domains (the dotted red arrows in Figure 22) due to the absence of amplitudes far greater than the baseline. The quantification of cavitation dose and the definition of cavitation threshold are able to determine whether inertial cavitation occurs or not. However, in some frequency spectrograms of higher acoustic intensities, the broadband noises are easy to be identified due to the increase of amplitude, indicating the inertial cavitation occurrence under these intensities (the solid red arrows in Figure 22).

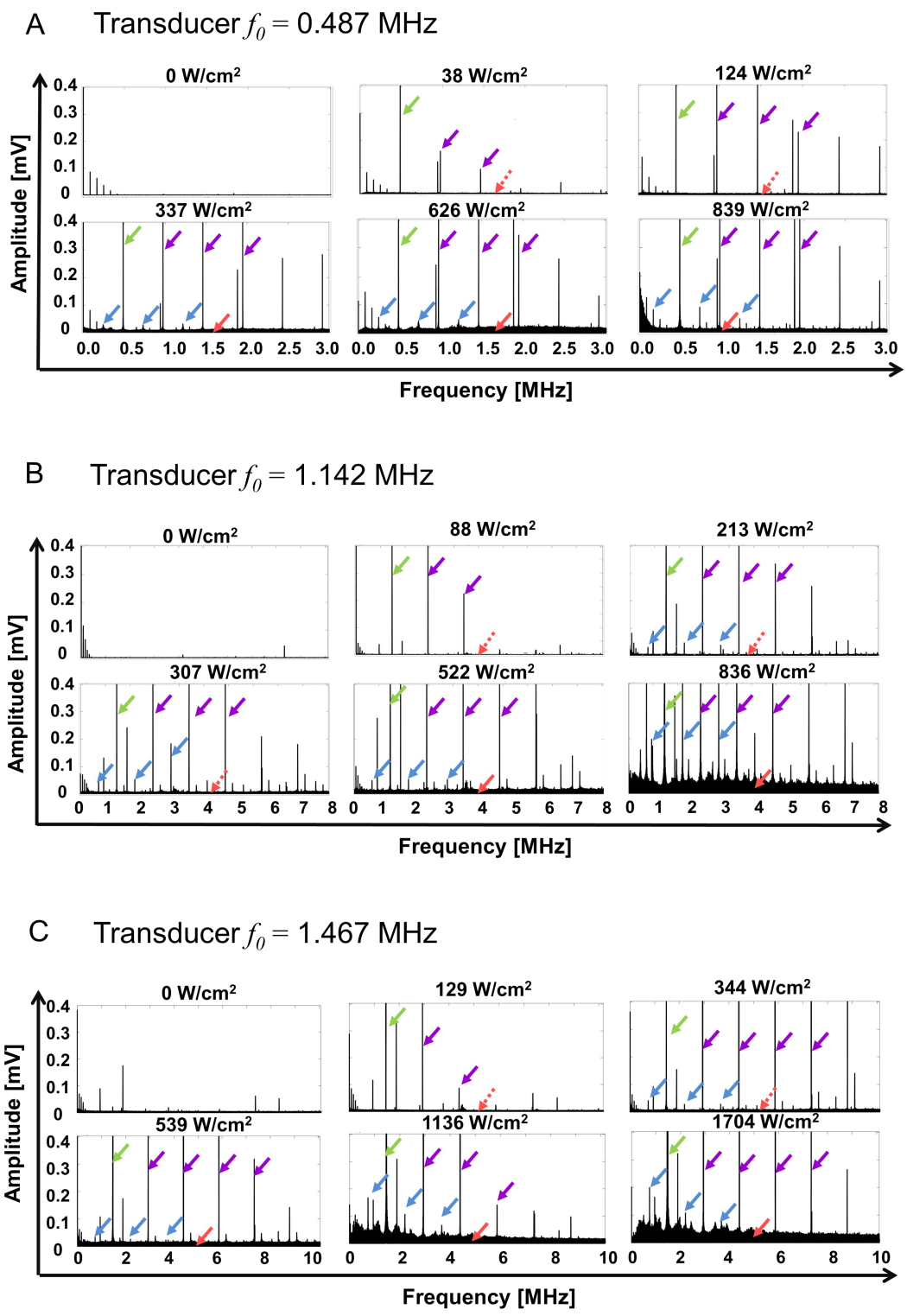

Figure 22: Acoustic signals in frequency-domain for one single period of 2.9 s FUS at (A) 0.487 MHz, (B) 1.142 MHz and (C) 1.467 MHz with different acoustic intensities. The digitized data was converted to a signal in the frequency-domain by FFT; green arrows: fundamental frequency (f_0); purple arrows: higher harmonics ($m*f_0$, m =2, 3, 4, 5…); blue arrows: sub- and ultra-harmonics ($m*f_0$ /2, m =1, 3, 5, 7…) representing stable cavitation; red (solid or dotted) arrows: broadband noise representing inertial cavitation.

7.2.2 Cavitation dose depends on the acoustic intensity

Figure 23 illustrates the curve of inertial cavitation level over time for the sonication period of 2.9 s generated by the three transducers with acoustic intensity from 0 – 1704 W/cm^2 (Figure 23), designating the randomness and uncertainty of cavitation event at each time point. The Y-axis values of each curve in Figure 23 represent the root mean square (RMS) voltage$_t$ over broadband noise, which depicts the inertial cavitation level at every time point (i.e. each FUS segment of 1.6 ms) with various acoustic frequencies and intensities. The integral of the area under the RMS voltage$_t$-time curve is defined as the cavitation dose during each 2.9 s FUS period.

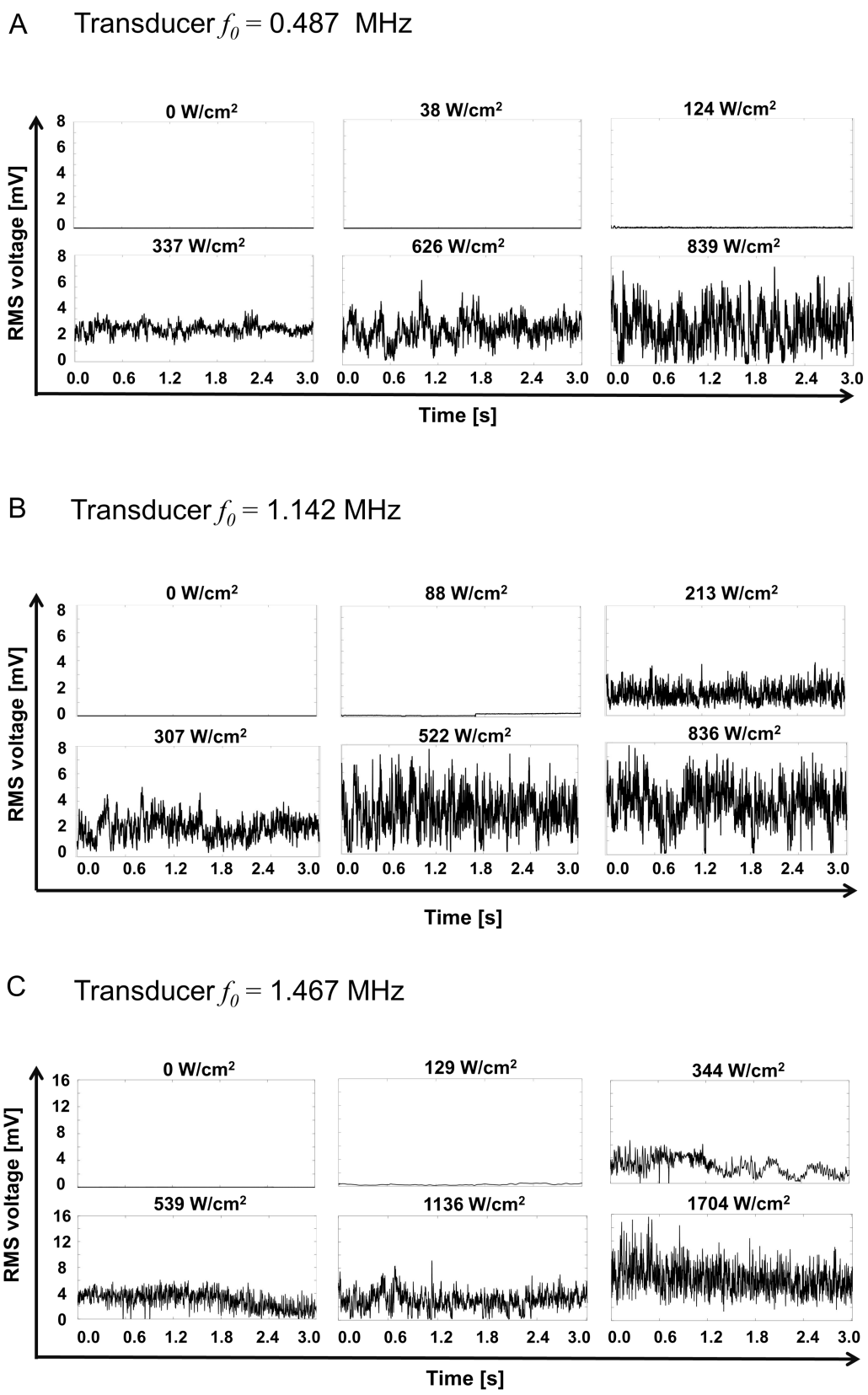

Figure 23: Root mean square (RMS) voltage$_t$-time curve for one single period of 2.9 s FUS at (A) o.487 MHz, (B) 1.142 MHz and (C) 1.467 MHz with various acoustic intensities. RMS voltage over the

range of broadband noise at a single time point (RMS voltage$_t$) was plotted as a function of time to exhibit the change in inertial cavitation level along with the time of FUS. The integral of the area under the RMS voltage$_t$-time curve was defined as the cavitation dose in 2.9 s.

For all transducers with various frequencies, both the inertial cavitation and stable cavitation dose were directly associated with acoustic intensity. The stable cavitation doses were calculated as 0.29 ± 0.99 mV*s, 0.25 ± 0.99 mV*s and 0.90 ± 0.65 mV*s at respective acoustic intensities of 124 W/cm^2 (0.487 MHz), 88 W/cm^2 (1.142 MHz) and 129 W/cm^2 (1.467 MHz) with total sonication duration of 40 s (Table 11). The sub- and ultra- harmonics (blue arrows in Figure 22) representing stable cavitation did not emerge in the frequency-domain at these acoustic intensities (no blue arrows in the figures of these intensities in Figure 22). Thus no stable cavitation occurred, and the cavitation doses calculated under these acoustic intensities should be the result of the background noise. Subsequently, the stable cavitation doses began to increase drastically with the enhancement of acoustic intensities (red solid arrows in Figure 24). As the acoustic intensities increased to 337 W/cm^2 (0.487 MHz), 213 W/cm^2 (1.142 MHz) and 344 W/cm^2 (1.467 MHz), the stable cavitation doses significantly enhanced to 7.03 ± 1.12 mV*s (0.487 MHz), 4.15 ± 0.36 mV*s (1.142 MHz) and 2.92 ± 1.68 mV*s (1.467 MHz). The sub- and ultra- harmonics were also presented in the frequency-domain (blue arrows in the figures of these intensities in Figure 22). As the continued increase of acoustic intensity, the stable cavitation dose was also increasing (red dotted arrows in Figure 24). The greatest stable cavitation dose was 23.94 ± 7.01 mV*s occurring at an acoustic intensity of 1704 W/cm^2 generated by the 1.467 MHz transducer. Therefore, the stable cavitation was acoustic intensity-dependent and estimated to occur at and above 337 W/cm^2 (0.487 MHz), 213 W/cm^2 (1.142 MHz), and 344 W/cm^2 (1.467 MHz).

The inertial cavitation threshold is defined as the acoustic intensity under which the broadband noise is equal to three times the standard deviation (SD) of background noise (S. Y. Wu et al., 2014). In the study, the SD of the background noise of the un-sonicated samples was measured as 2.07 mV*s (data not shown). After exposure with FUS at the intensity of 124 W/cm^2 (0.487 MHz), 88 W/cm^2 (1.142 MHz) and 129 W/cm^2 (1.467 MHz), hydrophone measured the inertial cavitation dose as - 0.20 ± 0.76 mV*s, 0.40 ± 0.71 mV*s, 0.82 ± 1.25 mV*s (Table 11), all of which were smaller than three times that of the SD (6.21 mV*s). Conversely, inertial cavitation dose was measured as 17.33 ± 8.23 mV*s, 10.57 ± 0.32 mV*s, 11.82 ± 5.48 mV*s for FUS exposure at the intensity of 337 W/cm^2 (0.487 MHz), 213 W/cm^2 (1.142 MHz) and 344

W/cm^2 (1.467 MHz) (Table 11). All three doses were greater than the inertial cavitation threshold and thus indicated the occurrence of inertial cavitation (purple solid arrows in Figure 24). After the initiation of inertial cavitation, the cavitation doses increased with the enhancements of acoustic intensities for each transducer (purple dotted arrows in Figure 24). The results demonstrated that the inertial cavitation occurred at and above 337 W/cm^2 (0.487 MHz), 213 W/cm^2 (1.142 MHz), and 344 W/cm^2 (1.467 MHz) and cavitation dose was positively related to acoustic intensity for each transducer.

The results of inertial cavitation measurement by FOH were confirmed with the TA method by measuring the fluorescence intensity of HTA. Compared with the untreated samples, there was a significant occurrence of fluorescence at the acoustic intensity of 337 W/cm^2 (0.487 MHz), 213 W/cm^2 (1.142 MHz) and 344 W/cm^2 (1.467 MHz) (blue solid arrows in Figure 24), indicating the occurrence of inertial cavitation during the 40 s FUS exposure. The fluorescence intensity increased with the continued enhancement of acoustic intensities (blue dotted arrows in Figure 24). This trend was comparable to the inertial cavitation dose results measured by the FOH.

In this context, the cavitation occurred at acoustic intensities of 344 W/cm^2 and above for the 1.467 MHz transducer, which was selected to perform the FUS treatment on cancer cells. Based on the results of cavitation measurement, the FUS treatments were defined as short FUS shots of 40 s without cavitation at the intensity of 129 W/cm^2 (FUS) and with cavitation at the intensity of 1136 W/cm^2 (FUS-Cav).

Table 11: Cavitation doses measured by the FOH system for the set of three transducers with different frequencies and acoustic intensities

Transducer frequency [MHz]	Peak-to-peak output voltage [mV]	Temporal-peak acoustic intensity [W/cm^2]	Stable cavitation dose [mV*s]	Inertial cavitation dose [mV*s]
0.487	120	37.98	0.39 ± 0.43	0.28 ± 0.79
	300	124.49	0.29 ± 0.99	- 0.20 ± 0.76
	450	336.99	7.03 ± 1.12	17.33 ± 8.23
	600	625.82	11.89 ± 3.55	27.07 ± 7.20
	720	838.61	15.19 ± 3.75	35.51 ± 8.36
1.142	190	87.76	0.25 ± 0.99	0.40 ± 0.71
	260	213.10	4.15 ± 0.36	10.57 ± 0.32
	350	306.83	6.76 ± 0.66	18.09 ± 3.95
	430	522.10	9.93 ± 1.28	31.74 ± 2.65
	500	835.89	15.04 ± 1.99	51.31 ± 3.90
1.467	110	128.81	0.90 ± 0.65	0.82 ± 1.25
	200	344.03	2.92 ± 1.68	11.82 ± 5.48
	250	538.89	5.53 ± 2.36	21.52 ± 13.73
	350	1136.22	16.33 ±4.29	46.27 ± 17.17
	420	1704.04	23.94 ± 7.01	64.07± 25.50

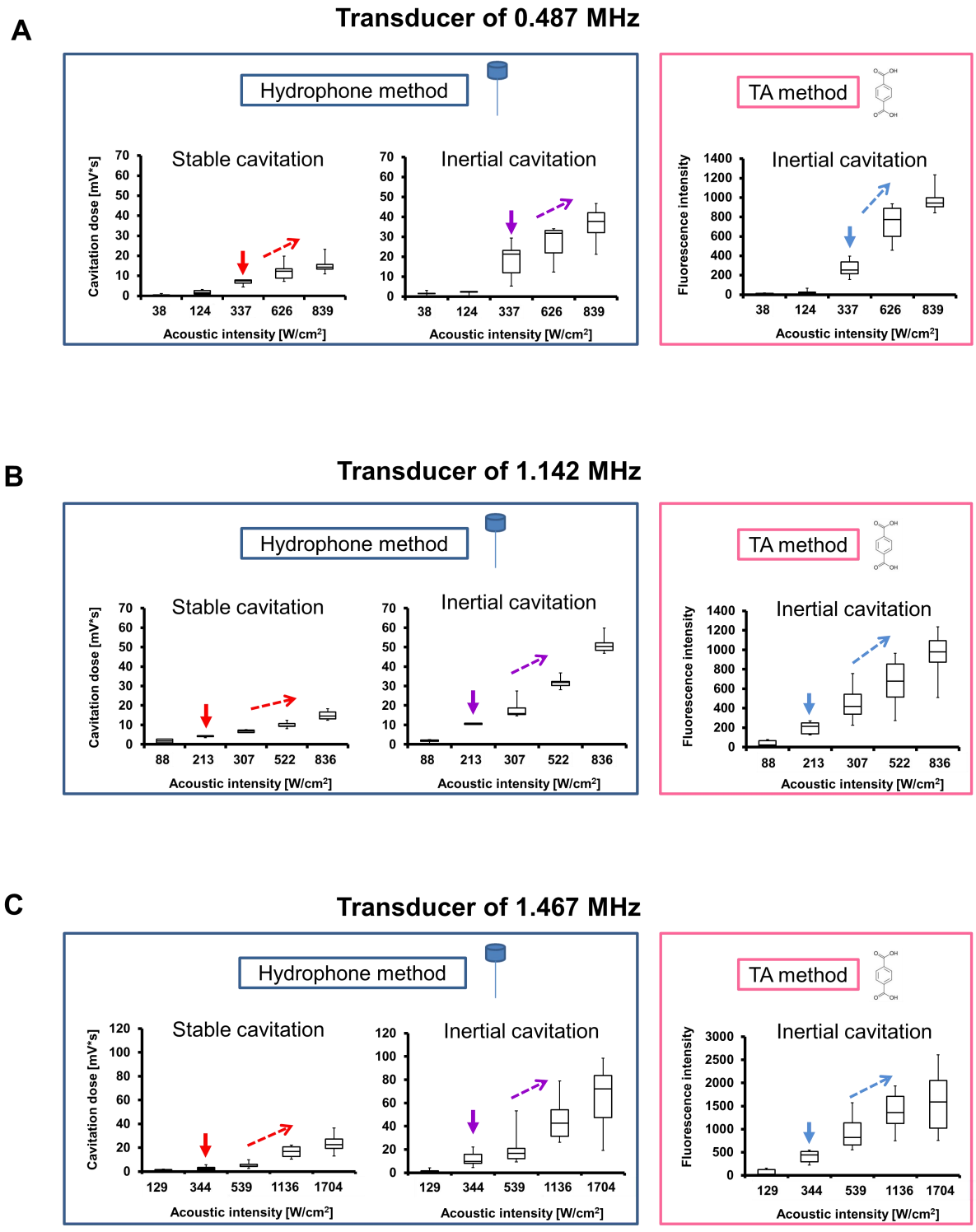

Figure 24: The association of cavitation doses with the acoustic intensities of three transducers with various frequencies. Results of cavitation measurement at the focal spot of FUS generated by (A) 0.487 MHz transducer, (B) 1.142 MHz transducer, (C) 1.467 MHz transducer; blue box: stable and inertial cavitation dose in 40 s was determined with FOH system, n = 9; red box: inertial cavitation dose was validated by terephthalic acid (TA) method with sonication duration of 40 s measuring the fluorescence of 2-hydroxyterephthalic acid (HTA), n = 9; solid arrows: the acoustic intensities for initiation of cavitation;

dotted arrows: the variation trends of cavitation doses along with enhancements of acoustic intensities.

7.3 FUS/FUS-Cav supports RT to reduce the long-term clonogenic survival of cancer cells

Clonogenic assay was performed to assess the long-term cell clonogenic survival after each treatment. Survival fraction (SF) calculated based on the quantification of cell colonies (Figure 25A) formed 14 – 21 days post-treatment revealed that single FUS/FUS-Cav had no impact on clonogenic survival of all cell lines. In contrast, single water bath hyperthermia (HT) treatment at 45 °C for 30 min resulted in a significantly decreased SF to 0.74 ± 0.04 (PC-3), 0.45 ± 0.07 (T98G) and 0.20 ± 0.05 (FaDu) compared to the group of untreated control with SF of 1.00. Compared to single RT of 5 Gy, the combination treatment demonstrated a 1.2-fold (FUS + 5 Gy), 2.0-fold (FUS-Cav + 5 Gy), and 3.6-fold (HT + 10 Gy) reduction of SF for PC-3 cells; a 1.5-fold (FUS + 5 Gy), 1.6-fold (FUS-Cav + 5 Gy), and 9.5-fold (HT + 5 Gy) reduction of SF for T98G cells and a 3.5-fold (FUS + 5 Gy), 7.4-fold (FUS-Cav + 5 Gy), and 14.8-fold (HT + 5 Gy) reduction of SF for Fadu cells. These results suggested that FUS/FUS-Cav exhibited radio-sensitization effects for all cancer cell lines, whereas the combination of water bath HT and RT showed more decrease of cell SF than FUS/FUS-Cav combined with RT, indicating lower radio-sensitization effects induced by FUS/FUS-Cav than water bath HT for RT of 5 Gy (Figure 25B). Notably, compared to single RT of 10 Gy for PC-3 cells, the combination treatment displayed a 26-fold (FUS + 10 Gy), 32-fold (FUS-Cav + 10 Gy), and 9-fold (HT + 10 Gy) SF decrease betokening more effective radio-sensitization of FUS/FUS-Cav than water bath HT in PC-3 cells (red arrows in Figure 25B). In contrast, T98G cells showed a different reaction where the combinatory treatment led to a 2.0-fold (FUS + 10 Gy), 6.4-fold (FUS-Cav + 10 Gy), and 6.0-fold (HT + 10 Gy) SF decrease compared to single RT indicating that FUS-Cav showed similar radio-sensitization effects with water bath HT (red arrows in Figure 25B). For FaDu cells, the combinatory treatments showed a 5.6-fold (FUS + 10 Gy), 4.7-fold (FUS-Cav + 10 Gy), and 5.9-fold (HT + 10 Gy) reduction of SF compared to RT alone, revealing the comparable radio-sensitization effects of FUS/FUS-Cav with water bath HT (red arrows in Figure 25B).

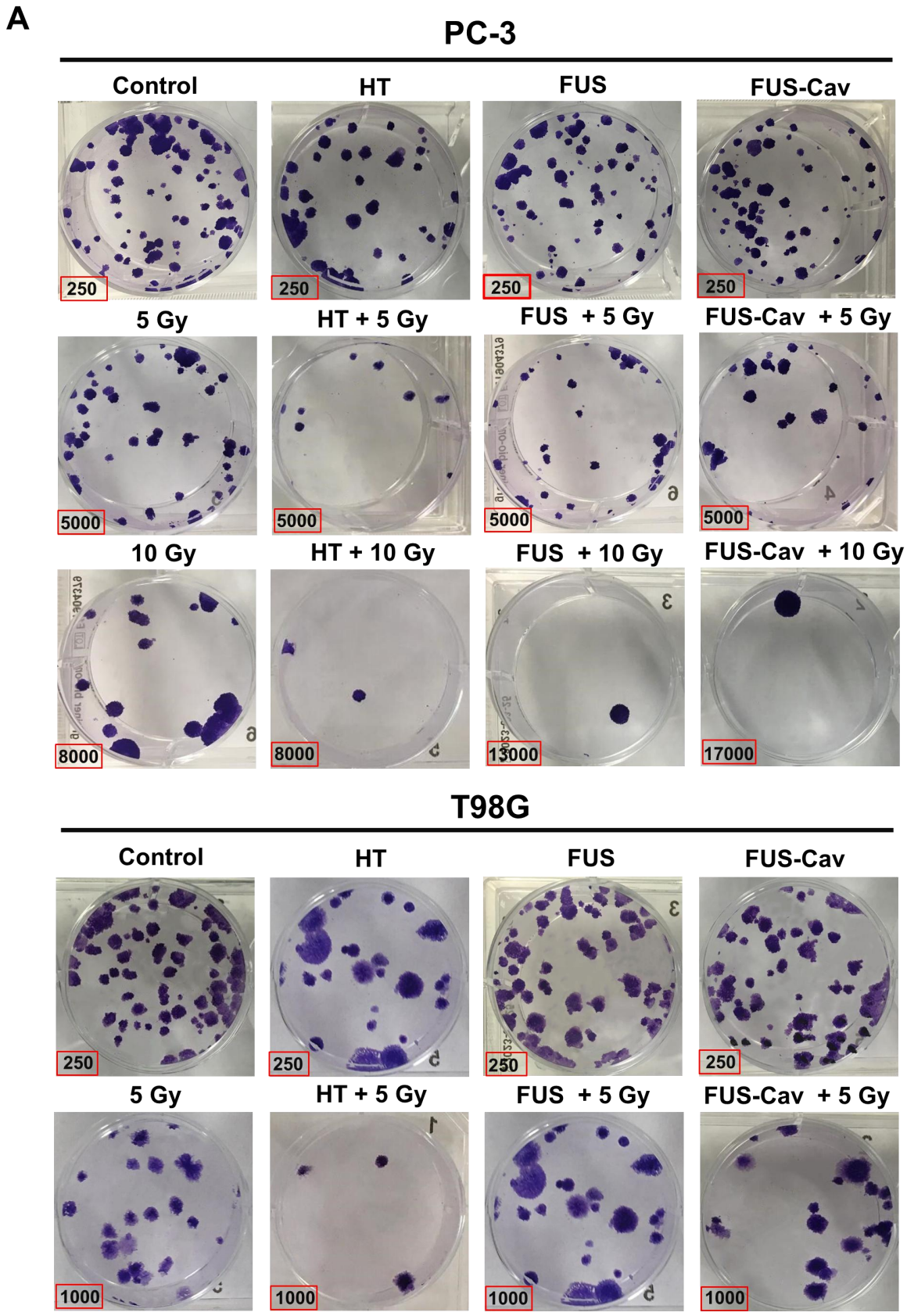
A
PC-3
Control
HT
FUS
FUS-Cav
250
250
250
250
5 Gy
HT + 5 Gy
FUS + 5 Gy
FUS-Cav + 5 Gy
5000
5000
5000
5000
10 Gy
HT + 10 Gy
FUS + 10 Gy
FUS-Cav + 10 Gy
8000
8000
13000
17000
T98G
Control
HT
FUS
FUS-Cav
250
250
250
250
5 Gy
HT + 5 Gy
FUS + 5 Gy
FUS-Cav + 5 Gy
1000
1000
1000
1000

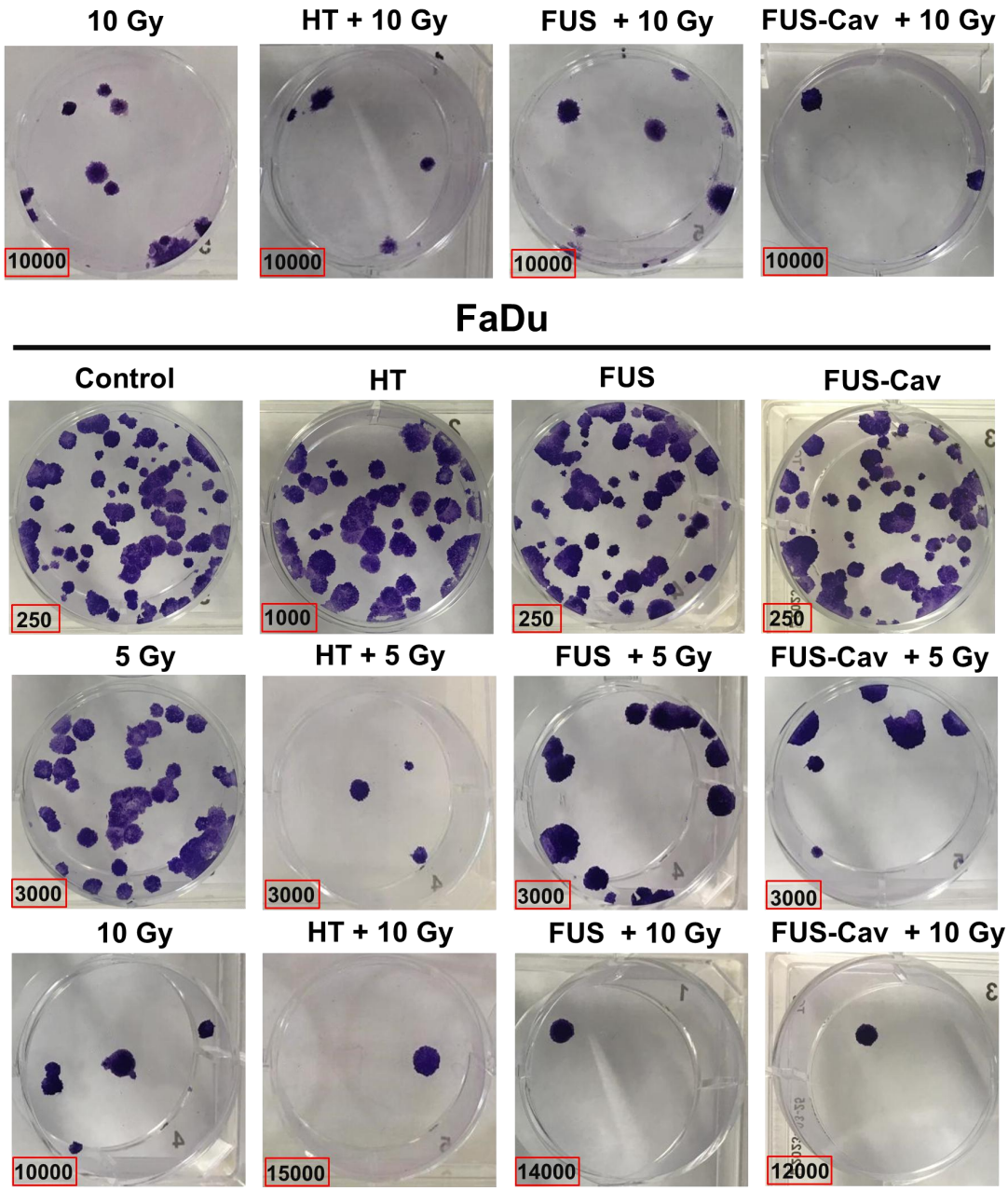
10 Gy
HT + 10 Gy
FUS + 10 Gy
FUS-Cav + 10 Gy
10000
10000
10000
10000
FaDu
Control
HT
FUS
FUS-Cav
250
1000
250
250
5 Gy
HT + 5 Gy
FUS + 5 Gy
FUS-Cav + 5 Gy
3000
3000
3000
3000
10 Gy
HT + 10 Gy
FUS + 10 Gy
FUS-Cav + 10 Gy
10000
15000
14000
12000

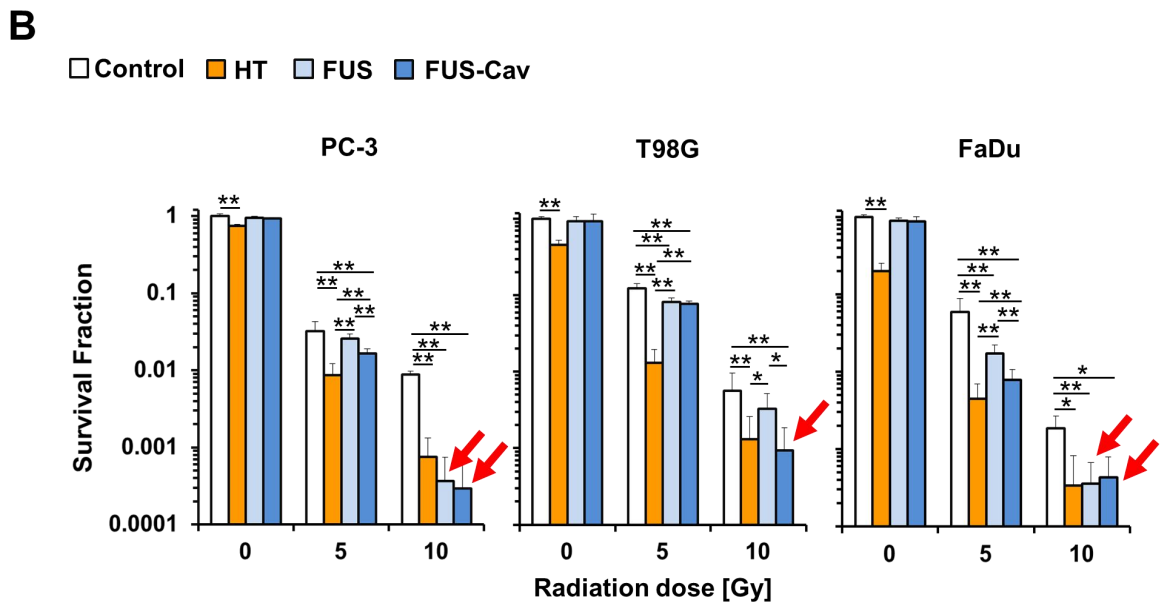

Figure 25: FUS or FUS-Cav revealed significant radio-sensitization effects reducing the long-term clonogenic survival in cancer cells. (A) Representative photographs of colony formation in the three cell lines. The seeding number per well is shown in the red box for each photograph. Cell survival fraction was calculated as the counted colonies divided by the product of the seeding number and the plating efficiency. (B) Cell survival fraction diagrams of PC-3, T98G and FaDu cells, suggesting the ability of a single cell to grow into a colony after various treatments. Data were normalized to untreated control, which was set to 1.00, and relative values are presented as mean ± SEM, n = 6, * $p \leq 0.05$; ** $p \leq 0.01$; *** $p \leq 0.001$. Red arrows: comparable radio-sensitization effects with water bath HT in the reduction of cell long-term clonogenic survival.

7.4 FUS/FUS-Cav increases the effects of HT by reducing the long-term clonogenic survival of cancer cells

Cell survival fraction was calculated based on seeding number and counted cell colonies (Figure 26A) formed 14 – 21 days post-treatment to investigate whether FUS/FU-Cav could support water bath HT to inhibit the cell clonogenic survival of three types of cancer cells. A significant reduction of SF was observed in all cell lines after the treatment of water bath HT (SF of single HT: 0.74 ± 0.04 in PC-3, 0.45 ± 0.07 in T98G, 0.20 ± 0.05 in FaDu) compared to untreated control (Figure 26B). The combination treatment of FUS and water bath HT resulted in a 1.3 fold (PC-3), 1.6 fold (T98G), and 2.6 fold (FaDu) reduction of SF compared to water bath HT alone (Figure 26B). Also, an increased effect was seen by adding FUS-Cav to water bath HT, leading to a 2-fold (PC-3), 1.9-fold (T98G), and 3.3-fold (FaDu) reduction of SF compared to single water bath HT treatment (red arrows in Figure 26B), revealing greater

additive effects of FUS-Cav to water bath HT than FUS.

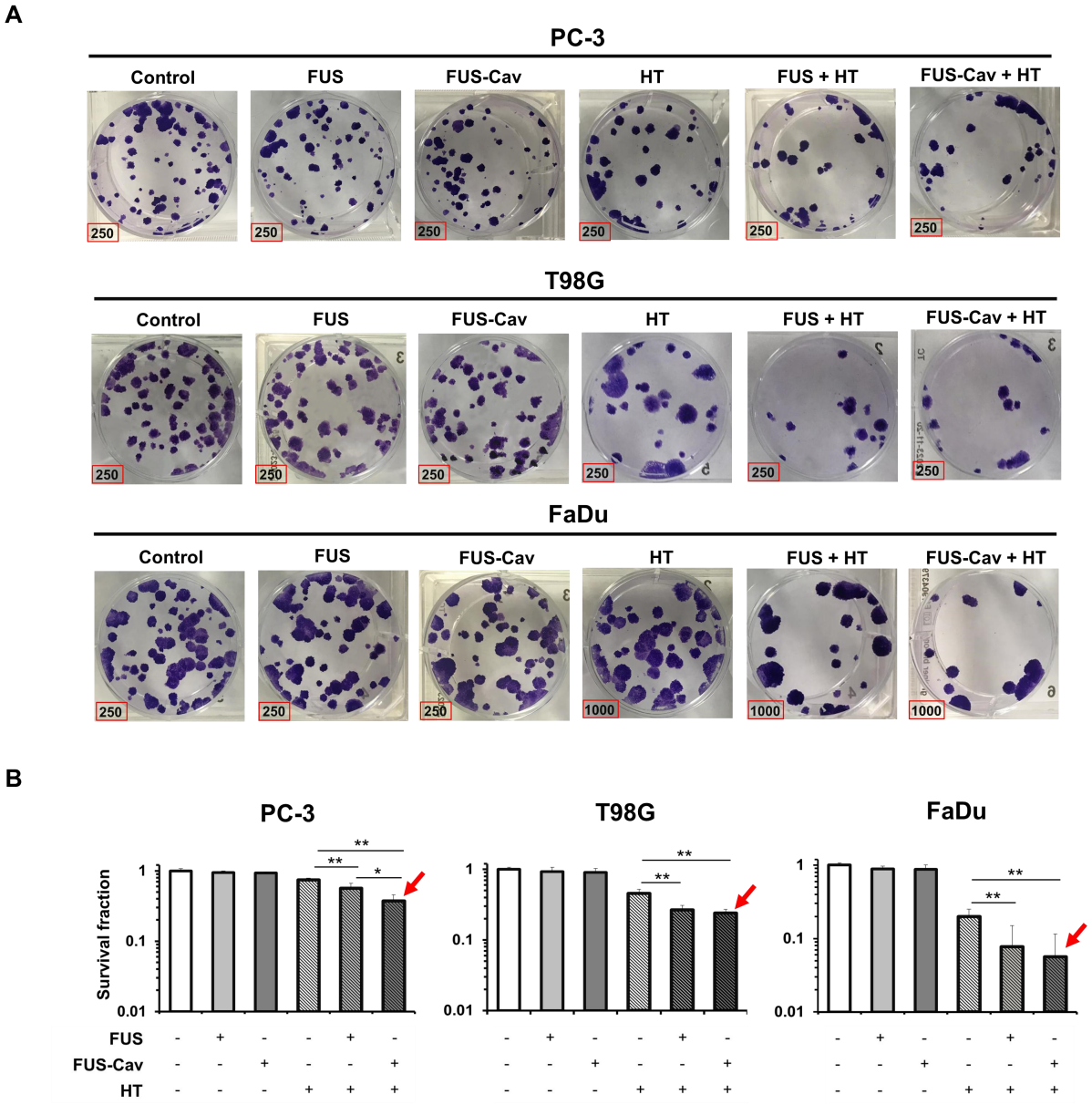

Figure 26: FUS or FUS-Cav demonstrated support to water bath HT. (A) Representative photographs of stained colonies are shown with the seeding number per well in the red box. Cell survival fraction was calculated as the counted colonies divided by the product of the seeding number and the plating efficiency. (B) Cell survival fraction diagrams derived from clonogenic assays of FaDu, T98G and PC-3 cells. Data were normalized to untreated control, which was set to 1.00, and relative values are presented as mean ± SEM, n = 6, * $p \leq 0.05$; ** $p \leq 0.01$; *** $p \leq 0.001$. Red arrows: the most additive effects induced by FUS-Cav to water bath HT reducing cell long-term clonogenic survival.

7.5 FUS/FUS-Cav enhances the suppressive effects of RT in short-term cell potential to invade and metabolic activity of prostate cancer cells

Transwell® invasion assay and WST-1 assay were performed to evaluate the short-term radio-sensitization effects of FUS/FUS-Cav on PC-3 cell invasion and cell metabolic activity. Representative microscopy images of PC-3 cells stained with crystal violet present the population of cells invading through the matrigel membrane (Figure 27A) 48 h post-treatment. FUS and FUS-Cav reduced relative cell invasion to 92.69 ± 0.98 % and 78.80 ± 1.62 % compared to 100 ± 0.76 % of untreated control. Relative cell metabolic activity was slightly reduced to 96.95 ± 4.23 % and 87.46 ± 3.18 % by single treatments of FUS and FUS-Cav. The impact of RT (10 Gy) on cell invasiveness and metabolic activity was significantly enhanced by adding short FUS or FUS-Cav treatment (Figure 27B – C): the relative cell invasion of PC-3 was reduced to 45.18 ± 0.74 % (FUS + 10 Gy) and 33.35 ± 0.60 % (FUS-Cav + 10 Gy) in comparison to single treatments (FUS: 92.69 ± 0.98 %; FUS-Cav: 78.80 ± 1.62 %; RT: 52.82 ± 1.31 %) 48 h after treatment. Compared with relative cell metabolic activity after single RT (81.53 ± 4.62 %), the combination of FUS or FUS-Cav and RT led to a significant loss of metabolic activity to 54.70 ± 3.58 % (FUS + 10 Gy) and 46.51 ± 3.61 % (FUS-Cav + 10 Gy). The above results reveal the radio-additive effects of FUS/FUS-Cav in decreasing the cell invasion and metabolic activity, and FUS-Cav showed greater radio-additive effects than FUS (red arrows in Figure 27B – C).

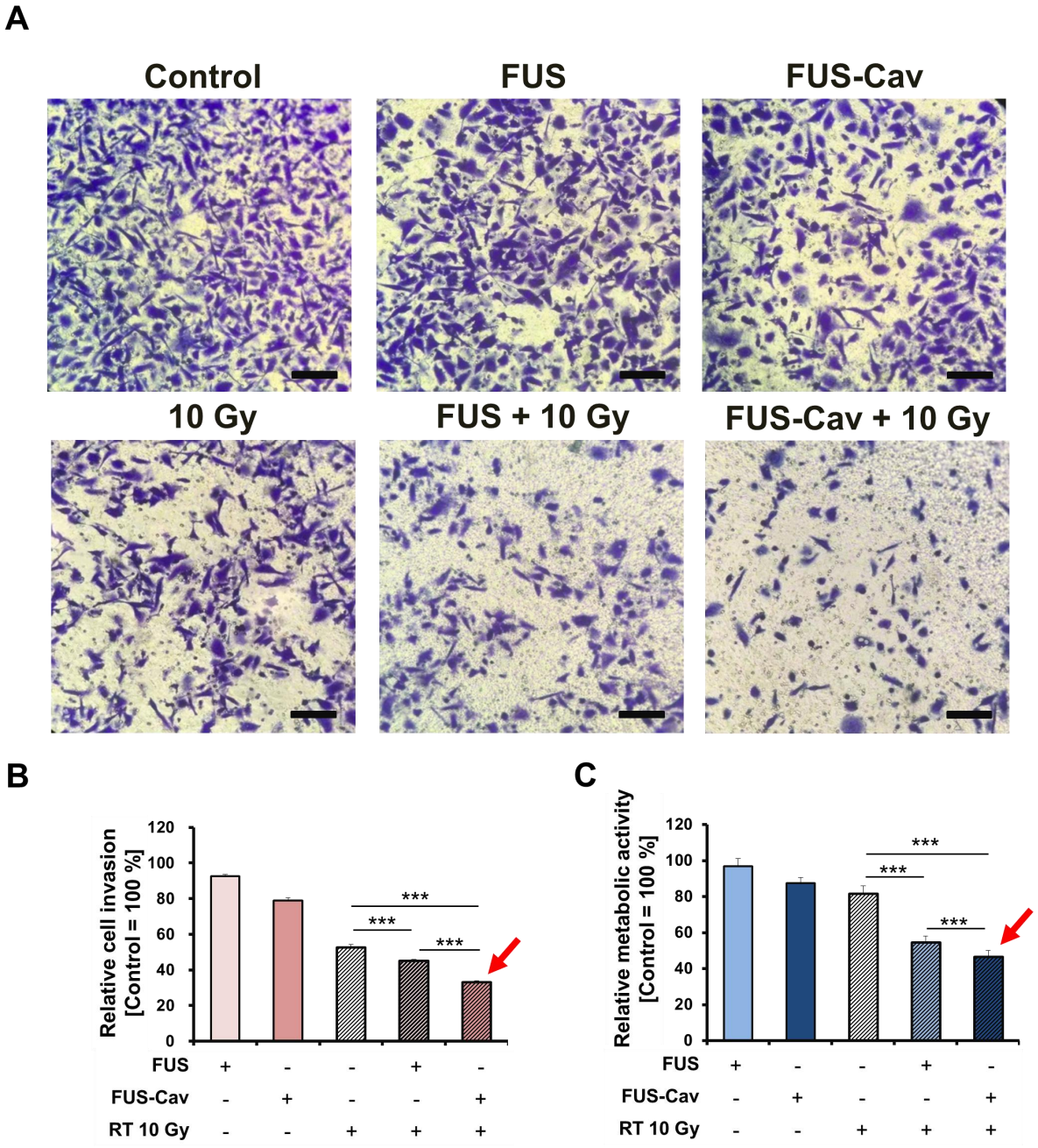

Figure 27: FUS or FUS-Cav supported RT to reduce the invasive potential and metabolic activity of PC-3 cells. (A) Representative microscopy images of Transwell® assay in PC-3 cells after different treatments. Scale bar = 100 µm. (B) Relative cell invasion of PC-3 cells derived from semi-quantitative analysis of the Transwell® assay revealing cell invasive potential 48 h post-treatment. (C) Relative cell metabolic activity of PC-3 cells 48 h post-treatment. Data were normalized to untreated control, which was set to 100 %, and relative values are presented as mean ± SEM, n = 6, * $p \leq 0.05$; ** $p \leq 0.01$; *** $p \leq 0.001$. Red arrows: the greatest radio-sensitization effects of FUS-Cav in diminishing cell potential to invade and metabolic activity.

7.6 FUS/FUS-Cav supports HT to diminish the short-term cell potential to invade and metabolic activity of prostate cancer cells

In order to assess the additive effects of FUS/FUS-Cav to water bath HT treatment on the cells' potential to invade and metabolic activity, Transwell® invasion assay and WST-1 assay were conducted 48 h after all treatments. Figure 28A contains the representative microscopy images showing the population of invaded cells. Single water bath HT treatment decreased the relative cell invasion and metabolic activity to 70.73 ± 2.14 % and 78.79 ± 5.89 %, respectively, in comparison to untreated control (Figure 28B – C). FUS and FUS-Cav displayed significant supports to water bath HT on the reduction of cell invasion and metabolic activity. The combination of FUS/FUS-Cav and water bath HT led to decreased relative cell invasion to 62.95 ± 0.66 % (FUS + HT) and 42.67 ± 1.17 % (FUS-Cav + HT) in comparison with single water bath HT treatment (70.73 ± 2.14 %), and the cell metabolic activity was decreased to 73.15 ± 3.76 % (FUS + HT) and 62.98 ± 4.74 % (FUS-Cav + HT) from 78.79 ± 5.89 % (HT). These results demonstrated that FUS-Cav provided the most additive effects to water bath HT in reducing both cell invasion and cell metabolic activity (red arrows in Figure 28B – C).

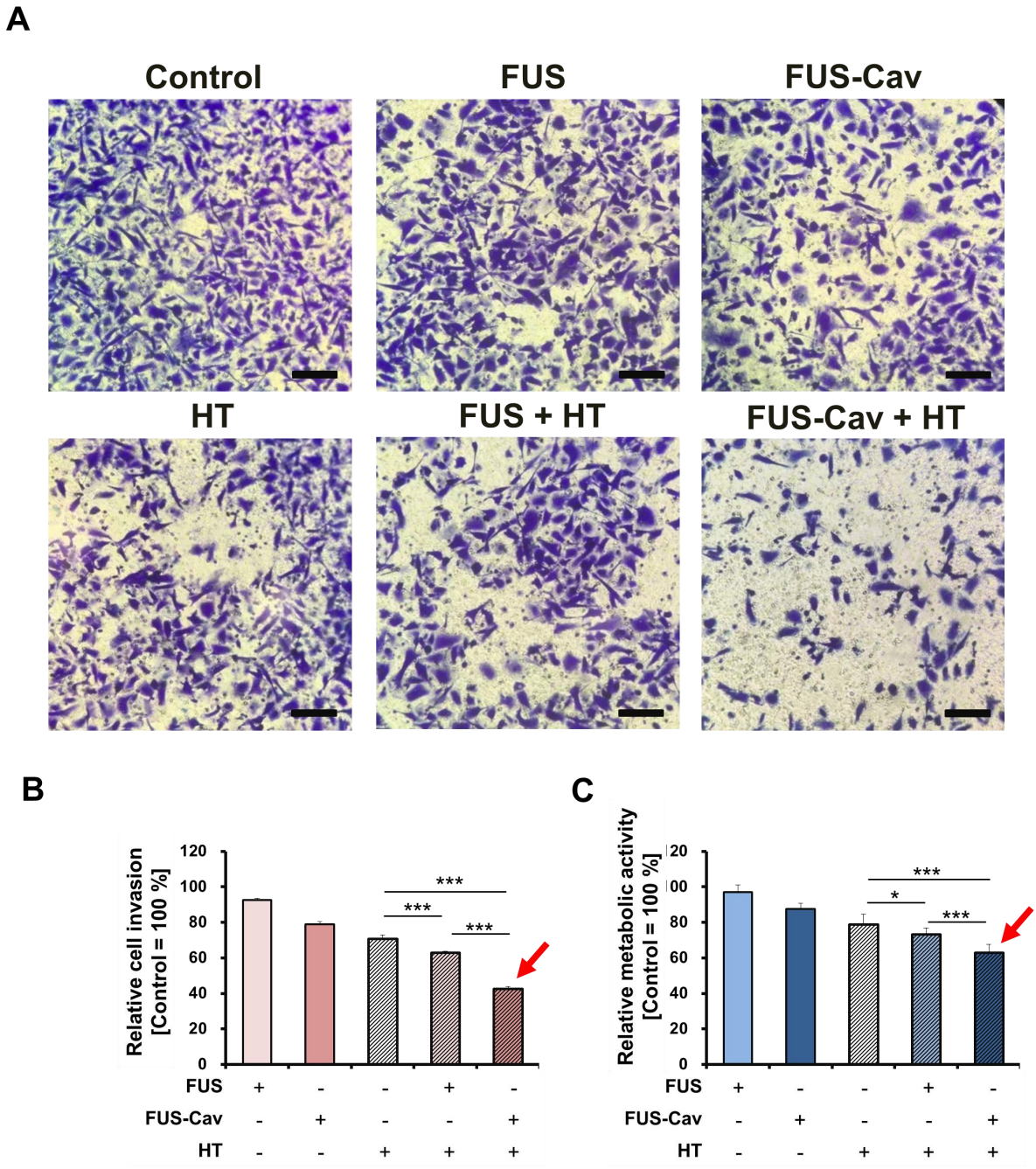

Figure 28: FUS or FUS-Cav demonstrated additive effects to water bath HT decreasing the cell invasive potential and metabolic activity in PC-3 cells. (A) Representative microscopy images of Transwell® assay in PC-3 cells after different treatments. Scale bar = 100 µm. Relative semi-quantitative results of the Transwell® assay and WST-1 assay indicate (B) cell invasive potential and (C) cell metabolic activity of PC-3 cells 48 h post-treatment. Data were normalized to untreated control, which was set to 100 %, and relative values are presented as mean ± SEM, n = 6, * $p \leq 0.05$; ** $p \leq 0.01$; *** $p \leq 0.001$. Red arrows: FUS-Cav is the most effective support to water bath HT in the suppression of cell invasiveness and metabolic activity.

7.7 FUS-Cav treatment immediately induces sonoporation effects in PC-3 and FaDu cells

The sonoporation effects induced by FUS/FUS-Cav treatment were exemplarily investigated in PC-3 and FaDu cell lines. Intracellular uptake of propidium iodide (PI) was considered as an indicator of sonoporation. The fluorescent images captured by the fluorescent microscope showed that the PI molecules were indeed taken into the PC-3 and FaDu cells (Figure 29A). The most significant numbers of PI-stained cell nuclei were observed in the group of FUS-Cav treatment at the acoustic intensity of 1136 W/cm^2 for both PC-3 and FaDu cells (red box in Figure 29A), indicating the occurrence of sonoporation. In contrast, FUS with the acoustic intensity of 129 W/cm^2 showed limited sonoporation events compared to FUS-Cav treatment. Cell membrane stained by CellMask^{TM} was not significantly changed before and after FUS-Cav treatment (Figure 29A). In the semi-quantitative results (Figure 29B), FUS-Cav treatment at the acoustic intensity of 1136 W/cm^2 with a total sonication duration of 40 s led to an increased percentage of intracellular PI in FaDu and PC-3 cells compared to untreated control. Remarkably, the percentage of PI-positive cells was significantly enhanced to 49.9 % in PC-3 and 23.3 % in FaDu cells immediately after exposure of FUS-Cav (red arrows in Figure 29B), and only 4 % PI-positive cells were observed in both cell lines 30 min post-treatment suggesting the recovery of sonoporation. In contrast, the percentage of PI-positive cells was not significantly increased (PC-3: 1.38 ± 0.24 %, FaDu: 1.78 ± 0.50 %) immediately after FUS exposure (129 W/cm^2, 40 s) compared to untreated samples (PC-3: 1.17 ± 1.11 %, FaDu: 1.47 ± 0.84 %), showing that sonoporation did not occur in PC-3 and Fadu cells after FUS treatment.

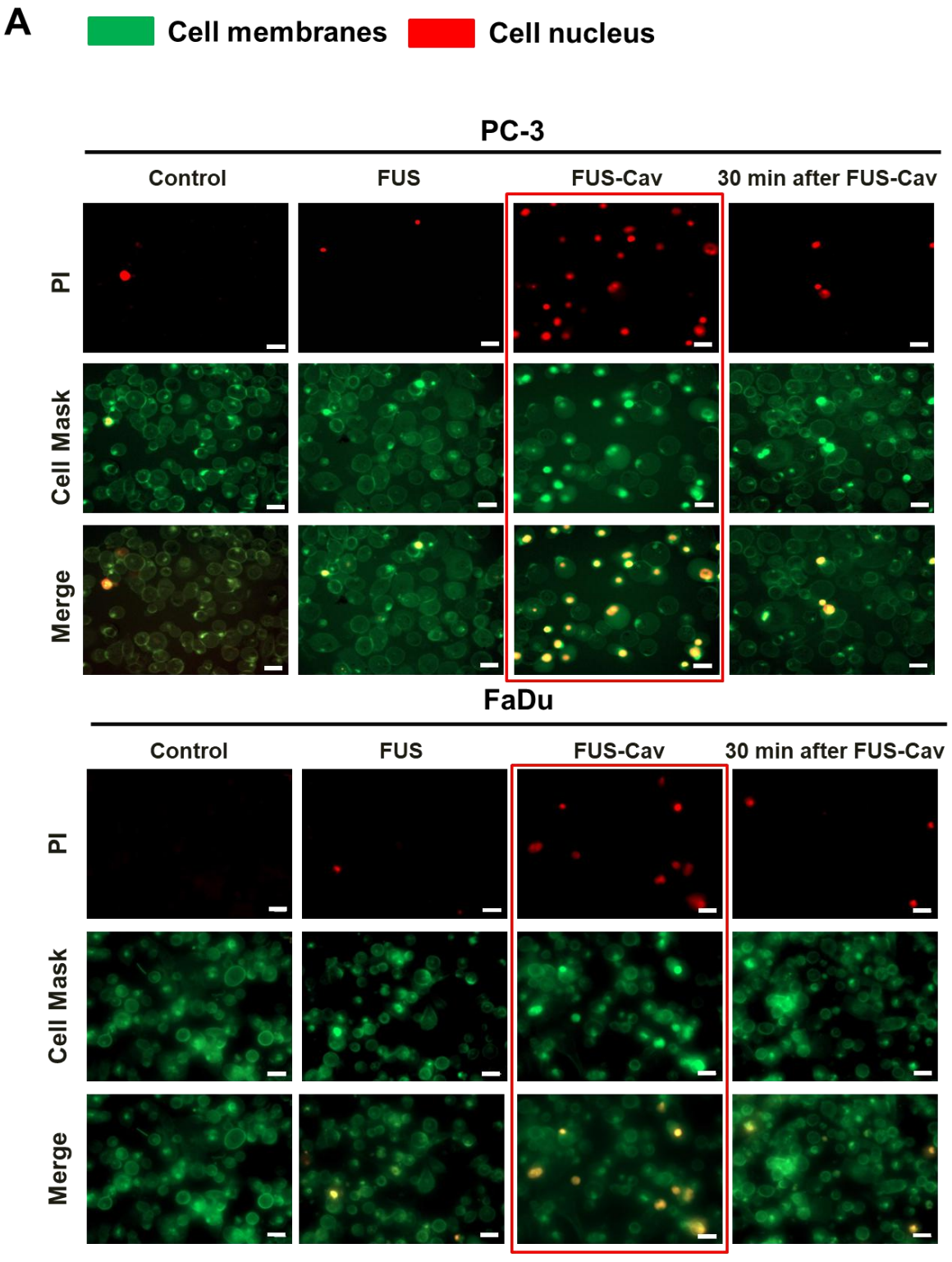
A
Cell membranes
Cell nucleus
PC-3
Control
FUS
FUS-Cav
30 min after FUS-Cav
PI
Cell Mask
Merge
FaDu
Control
FUS
FUS-Cav
30 min after FUS-Cav
PI
Cell Mask
Merge

B

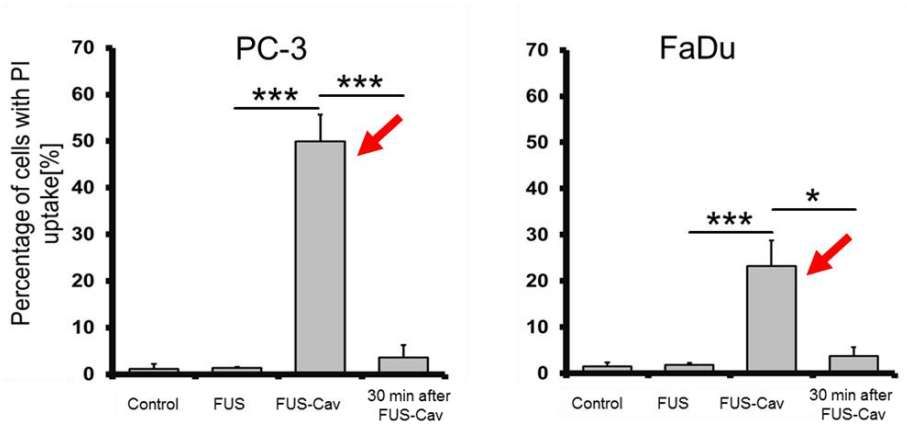

Figure 29: FUS-Cav induced sonoporation in PC-3 and FaDu cells. (A) Representative fluorescence microscopy images for PC-3 and FaDu cells showing an increase in red PI fluorescence during FUS-Cav (red box); red: PI-stained cell nucleus; green: CellMask™ stained cell membranes, scale bar = 30 µm. (B) Semi-quantitative analysis of PI-positive percentage representing the occurrence of sonoporation in PC-3 and FaDu cells. Data were normalized to total cell number as 100 % and relative values presented as mean ± SEM, n = 6, * $p \leq 0.05$; ** $p \leq 0.01$; *** $p \leq 0.001$. Red arrows: the highest PI uptake in each diagram.

7.8 FUS/FUS-Cav enhances the effects of HT by inhibiting the SRD5A protein level in prostate cancer cell lines

After various treatment regimes, fluorescent microscopy was performed to visualize the subcellular localization of immunofluorescence-tagged SRD5A1 and SRD5A3 in the prostate cancer PC-3 and LNCap cell lines. Figure 30A shows that the Alexa Fluor® 594-tagged SRD5A1 and SRD5A3 protein are bright, and the fluorescence is distributed diffusely throughout the cytoplasm. In most cases, SRD5A was detected in the cytoplasm, although it was also observed in cell nuclear/perinuclear localization. In the fluorescent microscopy images for both PC-3 and LNCap cell lines, no striking difference was noted in the distribution of immunofluorescence-tagged SRD5A1 and SRD5A3 in either the single treatment of FUS or FUS-Cav compared to untreated control (blue arrows in Figure 30A). Nevertheless, the distribution of SRD5A1 and SRD5A3 proteins were down-regulated 24 h post single treatment of water bath HT. The effects of water bath HT treatment on reducing the SRD5A level were seemingly enlarged by adding short FUS or FUS-Cav treatment in terms of the visualization of SRD5A protein distributions (red arrows in Figure 30A).

In order to quantify the percentage of fluorescent dye-positive cells in the total number of cells collected

for analysis, flow cytometry was performed for the fluorescence-activated cell sorting after each treatment. Figure 30B shows the percentage of cells with immunofluorescence-tagged SRD5A1 or SRD5A3 protein for PC-3 and LNCap cell lines 24 h post-treatment. Figure 30C demonstrates the relative level of these two isozymes to untreated control in both cell lines after various treatments. For the PC-3 cell line, the relative SRD5A1 level was significantly diminished to 52.94 ± 2.84 % by the single treatment of water bath HT compared to the untreated sample (100 ± 2.22 %). Single treatment of FUS/FUS-Cav had no impact on the SRD5A1 expression, and the combinatory treatment of FUS/FUS-Cav and water bath HT was not able to significantly reduce the SRD5A1 level compared to single treatment of water bath HT as well, indicating FUS/FUS-Cav had no additive effects to water bath HT suppressing the SRD5A1 expression. Single FUS/FUS-Cav did not show significant suppressive effects on the expression of SRD5A3 compared to untreated control. The relative SRD5A3 level was significantly decreased by the combinatory treatments to 22.87 ± 4.88 % (FUS-Cav + HT) compared to single water bath HT (55.70 ± 4.70 %), denoting a significant additive effect of FUS-Cav to water bath HT in reducing the SRD5A3 expression (the red arrow in the red box of Figure 30C). For the LNCap cell line, the relative SRD5A1 level was slightly decreased to 95.40 ± 4.75 % and 91.19 ± 2.98 % by single treatments of FUS and FUS-Cav compared to untreated control (100 ± 5.39 %), which was consistent with the result of microscopy observation (Figure 30C). Nevertheless, FUS strengthened the impacts of combination treatment of FUS + HT, significantly reducing the relative SRD5A1 level from 51.21 ± 6.47 % (HT) to 43.72 ± 2.43 % (FUS + HT). More additive effects were seen by adding FUS-Cav to water bath HT resulting in a greater decrease to 38.28 ± 3.76 % in SRD5A1 level compared with water bath HT treatment alone (the upper red arrow in the blue box of Figure 30C). FUS or FUS-Cav treatment alone significantly reduced the SRD5A3 level to 82.6 ± 11.4 % or 87.93 ± 4.58 % compared to untreated control. FUS enhanced the inhibition effects of combination treatment of FUS + HT, reducing the SRD5A3 level from 26.78 ± 5.03 % (HT) to 12.92 ± 1.35 % (FUS + HT) (the lower red arrow in the blue box of Figure 30C). Whereas, FUS-Cav had little or no additive effects on water bath HT: the combination treatment of FUS-Cav with water bath HT led to an insignificant reduction of SRD5A3 level from 26.78 ± 5.03 % (HT) to 23.32 ± 1.76 % (FUS-Cav + HT).

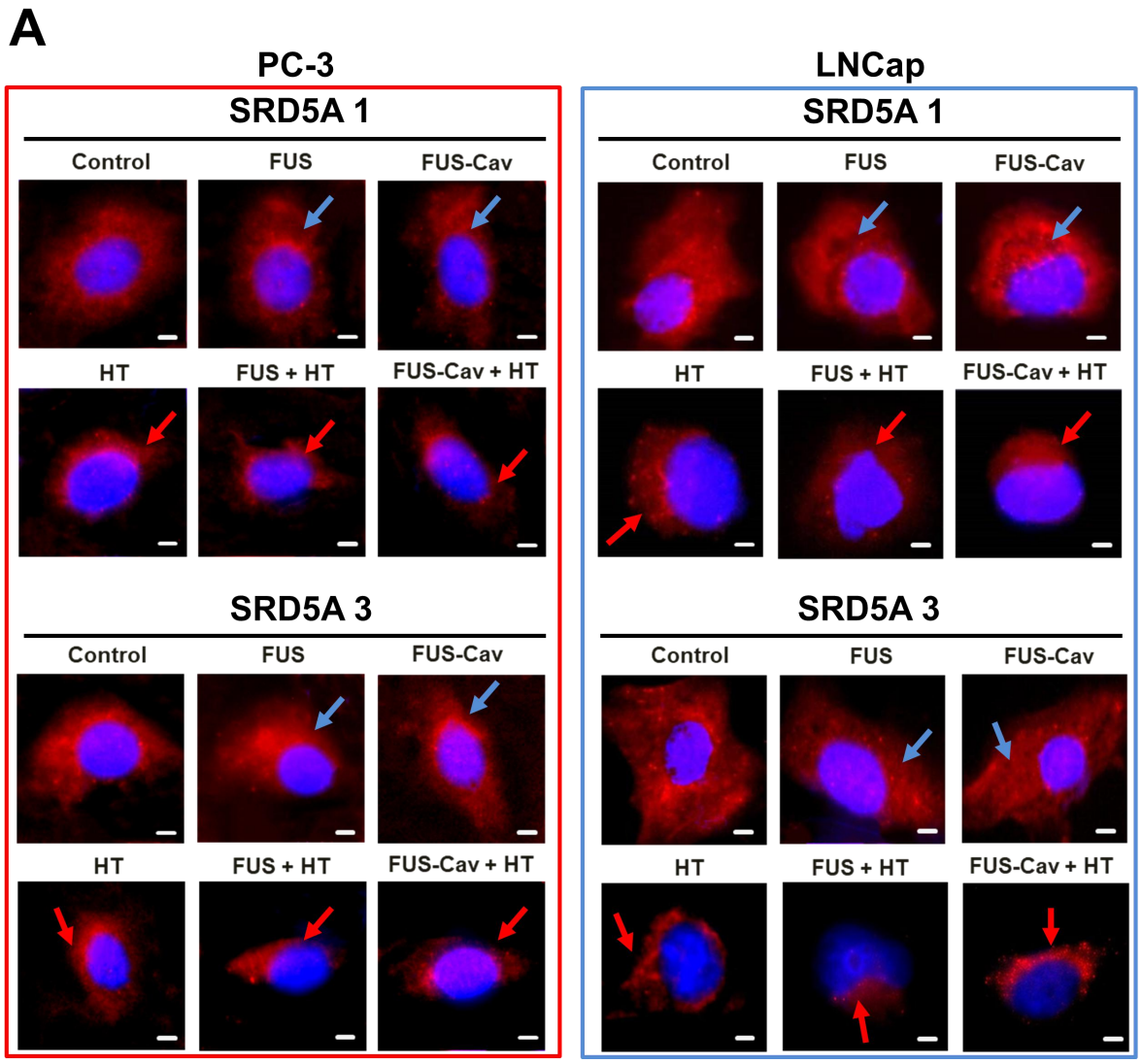
A
PC-3
LNCap
SRD5A 1
Control
FUS
FUS-Cav
HT
FUS + HT
FUS-Cav + HT
SRD5A 3

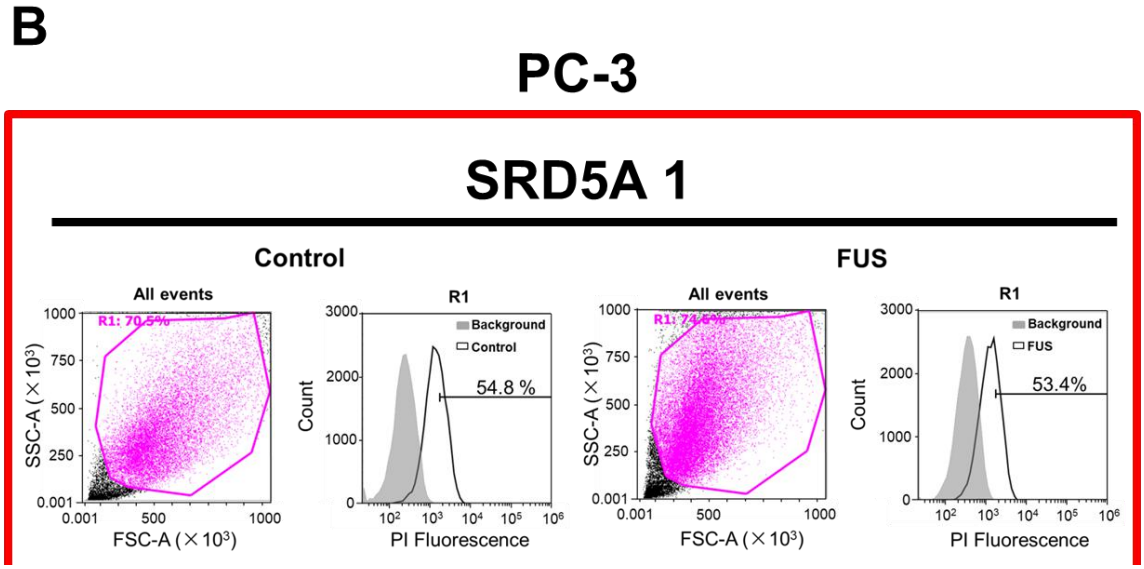
B
PC-3
SRD5A 1
Control
FUS
All events
R1
R1: 70.5%
SSC-A (×10³)
FSC-A (×10³)
Count
PI Fluorescence
Background
Control
54.8 %
R1: 74.6%
FUS
53.4%

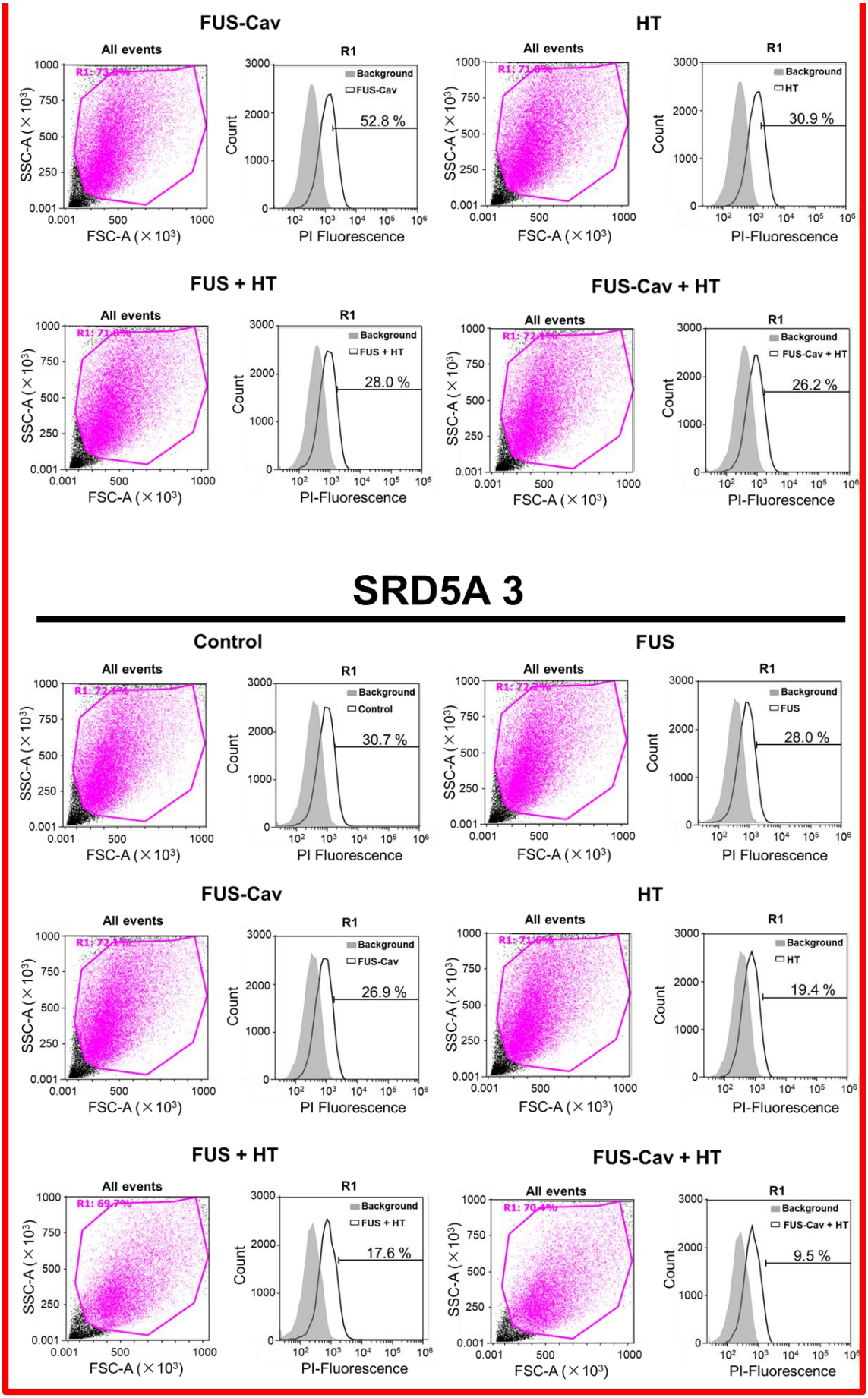
FUS-Cav
All events
R1
Background
FUS-Cav
52.8 %
HT
All events
R1
Background
HT
30.9 %
FUS + HT
All events
R1
Background
FUS + HT
28.0 %
FUS-Cav + HT
All events
R1
Background
FUS-Cav + HT
26.2 %
SSC-A (×10³)
FSC-A (×10³)
Count
PI Fluorescence
PI-Fluorescence
SRD5A 3
Control
All events
R1
Background
Control
30.7 %
FUS
All events
R1
Background
FUS
28.0 %
FUS-Cav
All events
R1
Background
FUS-Cav
26.9 %
HT
All events
R1
Background
HT
19.4 %
FUS + HT
All events
R1
Background
FUS + HT
17.6 %
FUS-Cav + HT
All events
R1
Background
FUS-Cav + HT
9.5 %

LNCap

SRD5A 1

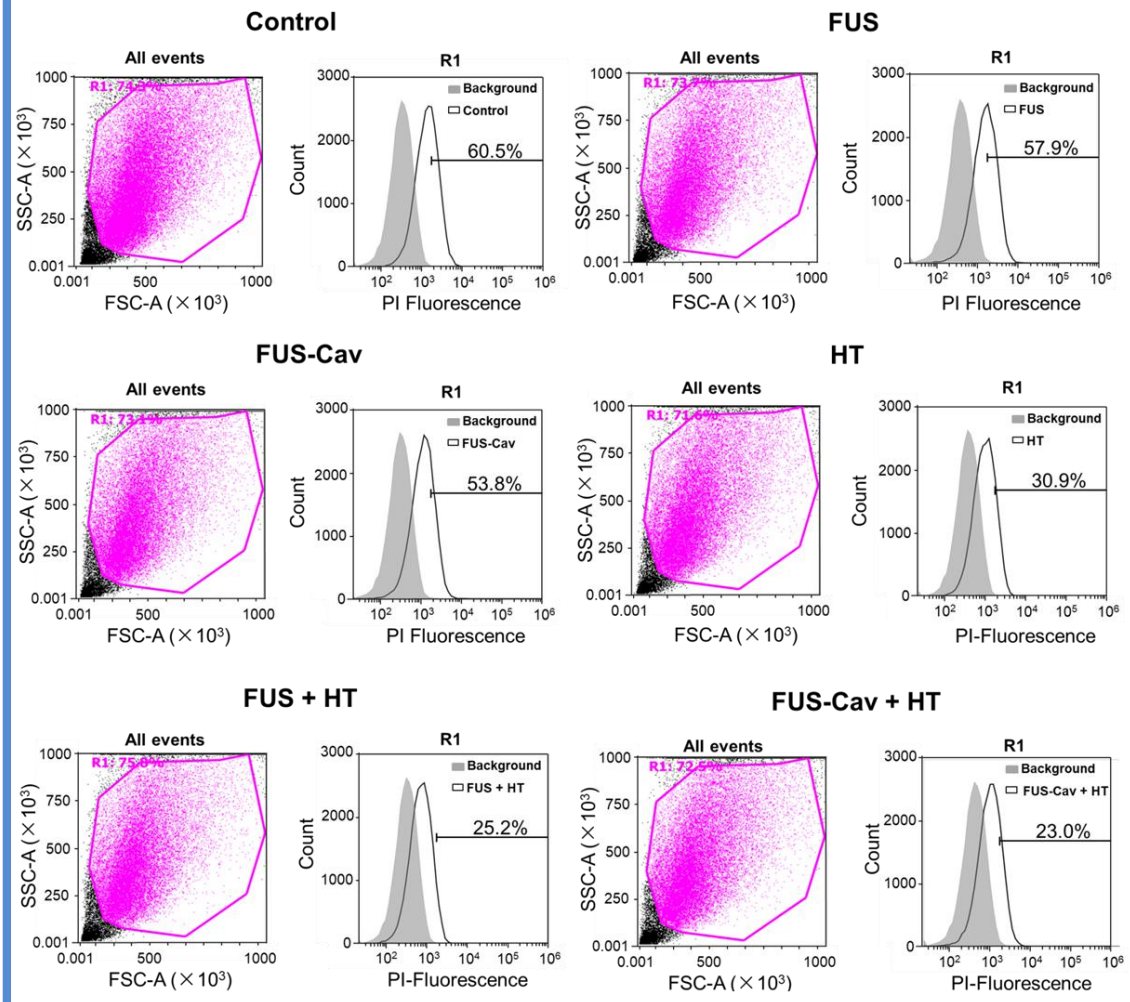

SRD5A 3

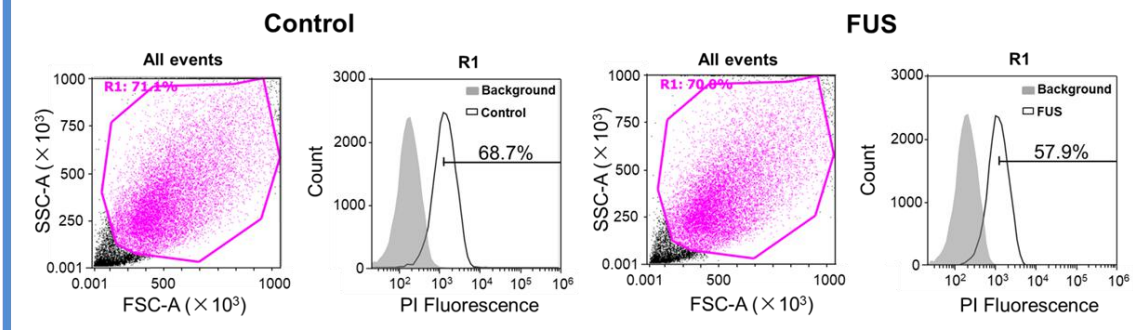

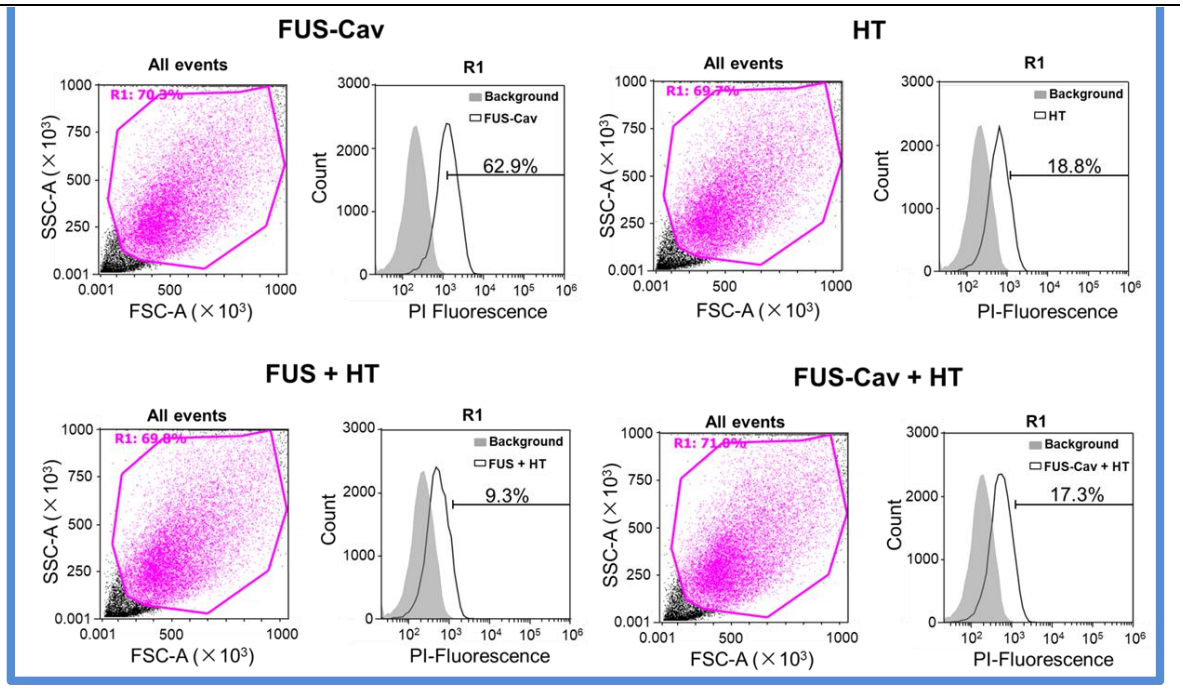

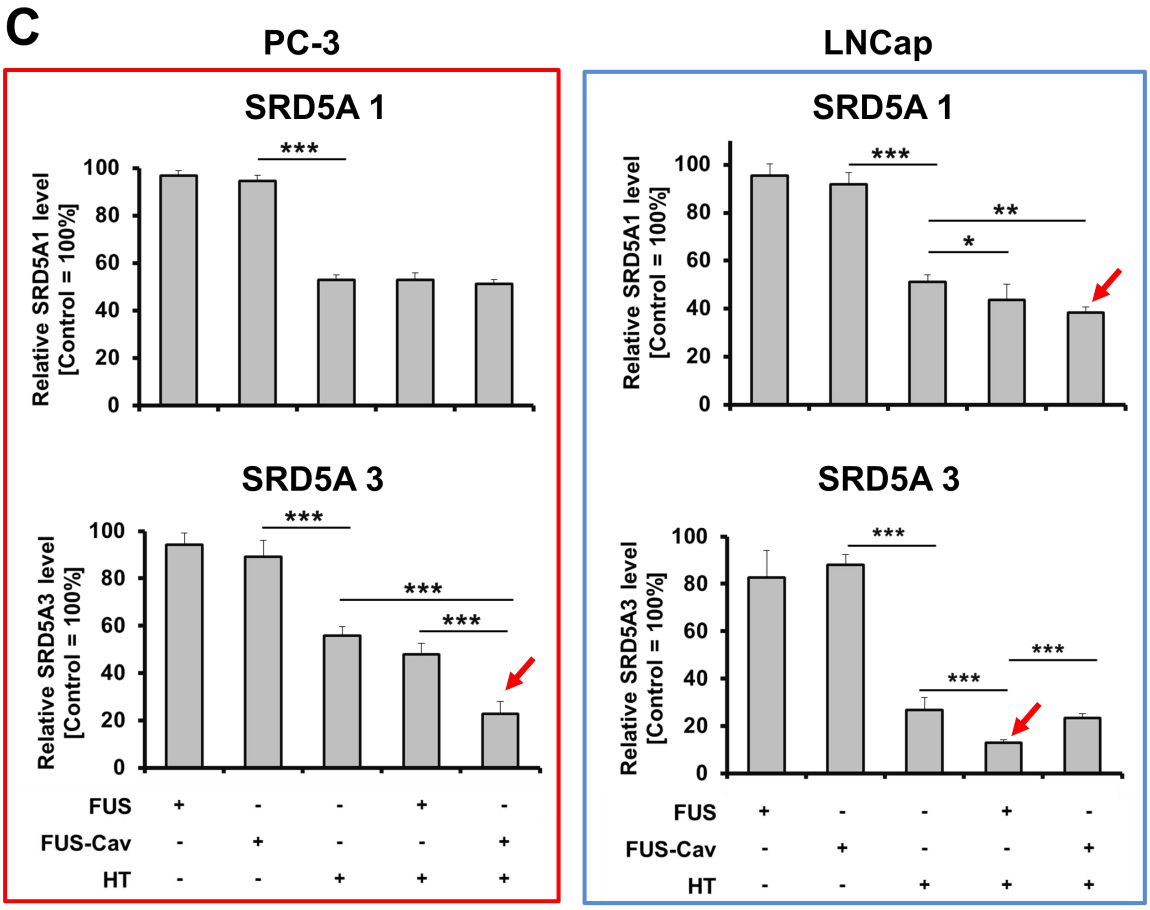

Figure 30: Various effects of FUS/FUS-Cav to water bath HT decreasing the SRD5A distribution and expression were associated with cancer cell type. (A) Representative fluorescence microscopy images for PC-3 and LNCap cells showing the distribution of SRD5A1 and SRD5A3 proteins in the cytoplasm 24

h post-treatment. Scale bar = 5 μm, blue arrows: no striking difference with untreated control; red arrows: significant reduction compared to untreated control. (B) Flow cytometry results exhibit the percentage of immunofluorescence-positive cells in all collected PC-3 and LNCap cells for analysis: (Left) Scatter plots (cell size/granularity) showing intact cells occupying a larger population in the center of plots and cell debris occupying a smaller population near side scatter axis; (Right) Histograms of immunofluorescence-positive cells showing the SRD5A level (percentage of fluorescence-positive cells indicated in each plot) after each treatment. The fluorescence-negative cells immunostained in the absence of a primary antibody were set as the background control. (C) Statistical results of quantitative analysis with flow cytometry indicate SRD5A1 and SRD5A3 levels in PC-3 and LNCap cells 24 h post-treatment. Data were normalized to untreated control, which was set to 100 %, and relative values are presented as mean ± SEM, n = 6, * $p \leq 0.05$; ** $p \leq 0.01$; *** $p \leq 0.001$. Red arrows: the most additive effects of FUS/FUS-Cav to water bath HT reducing the SRD5A level in both cell lines.

7.9 FUS-Cav enhances the effects of the testosterone treatment by reducing the long-term cell metabolic activity of androgen-dependent prostate cancer cell line

In order to examine the effects of exogenous testosterone on the metabolic activity of prostate cancer cells in the long-term culture *in vitro*, cell culture medium containing exogenous dissolved testosterone was used to cultivate the androgen-dependent prostate cancer cell line LNCap and the androgen-independent prostate cancer cell line PC-3. Figure 31A shows that the confluence of adherent LNCap cells was reduced 12 days after treatment with 1 ng/mL testosterone compared to untreated control. The higher concentrations of 8 ng/mL and 32 ng/mL testosterone result in a greater cell confluence reduction (red arrows in Figure 31A) compared to 1 ng/mL testosterone. The relative metabolic activity of LNCap cells was reduced to 38.66 ± 6.02 % (1 ng/mL), 27.11 ± 4.42 % (8 ng/mL) and 25.51 ± 3.12 % (32 ng/mL) 12 days post-treatment (red arrows in Figure 31B) compared to untreated control (100.00 ± 15.55 %). Compared with the untreated control, invariant cell confluence after testosterone treatment demonstrated that testosterone in the concentration of 1, 8, and 32 ng/mL seemingly had no impact on androgen-independent cell line PC-3 (Figure 31B). No significant reduction of relative metabolic activity was measured for PC-3 cells 8 days after testosterone treatment (blue arrows in Figure 31B).

In order to determine the effects of FUS/FUS-Cav on testosterone treatment, cancer cells in the culture medium containing testosterone were treated with FUS/FUS-Cav in advance. Cell confluence reduction induced by each treatment was observed by microscopy images. The cell confluence was decreased by the combination treatment (FUS-Cav + 1 or 8 ng/mL testosterone) compared to single testosterone treatment with 1 or 8 ng/mL (purple arrows in Figure 31A). FUS/FUS-Cav treatment alone had no impact on the

relative metabolic activity level after long-term culture for both cell lines (Figure 31B). However, FUS-Cav supported testosterone treatment in LNCap cells by reducing the long-term metabolic activity, the combination treatment of FUS-Cav and 1 ng/mL testosterone led to a significant reduction of relative metabolic activity from 38.66 ± 6.02 % (1 ng/mL testosterone treatment) to 28.90 ± 9.34 % (FUS-Cav + 1 ng/mL testosterone treatment), and the FUS-Cav combined with 8 ng/mL testosterone treatment resulted in a significant decrease of relative metabolic activity from 27.11 ± 4.41 % (8 ng/mL testosterone treatment) to 15.32 ± 6.43 % (FUS-Cav + 8 ng/mL testosterone treatment) (purple arrows in Figure 31B). However, FUS/FUS-Cav could not support the testosterone treatment with 32 ng/mL testosterone to further reduce the cell relative metabolic activity. For the androgen-independent cell line PC-3, both single treatments of FUS/FUS-Cav and the combination with testosterone treatment had no significant impact on the cell metabolic activity after long-term culture (blue arrows in Figure 31B).

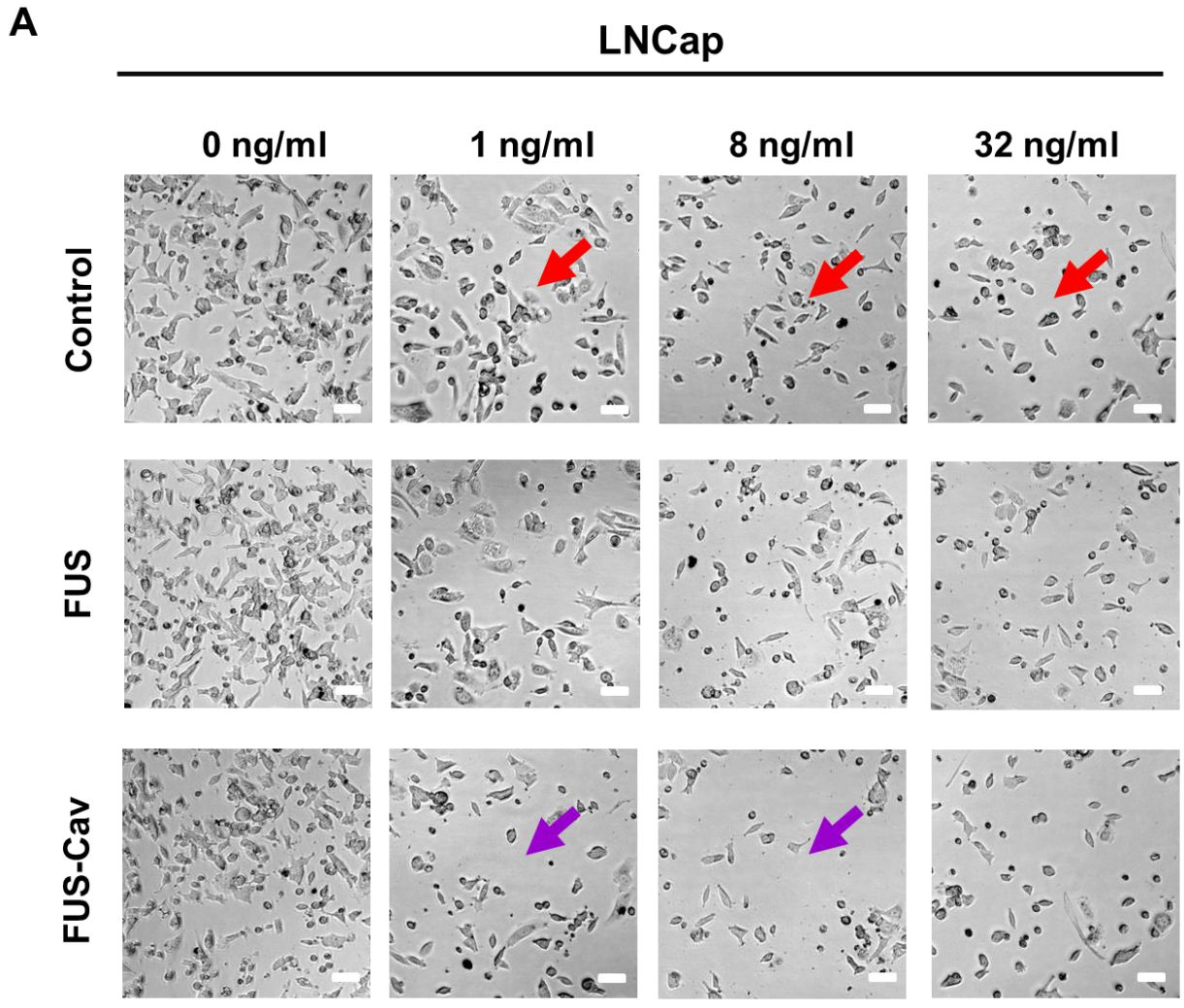

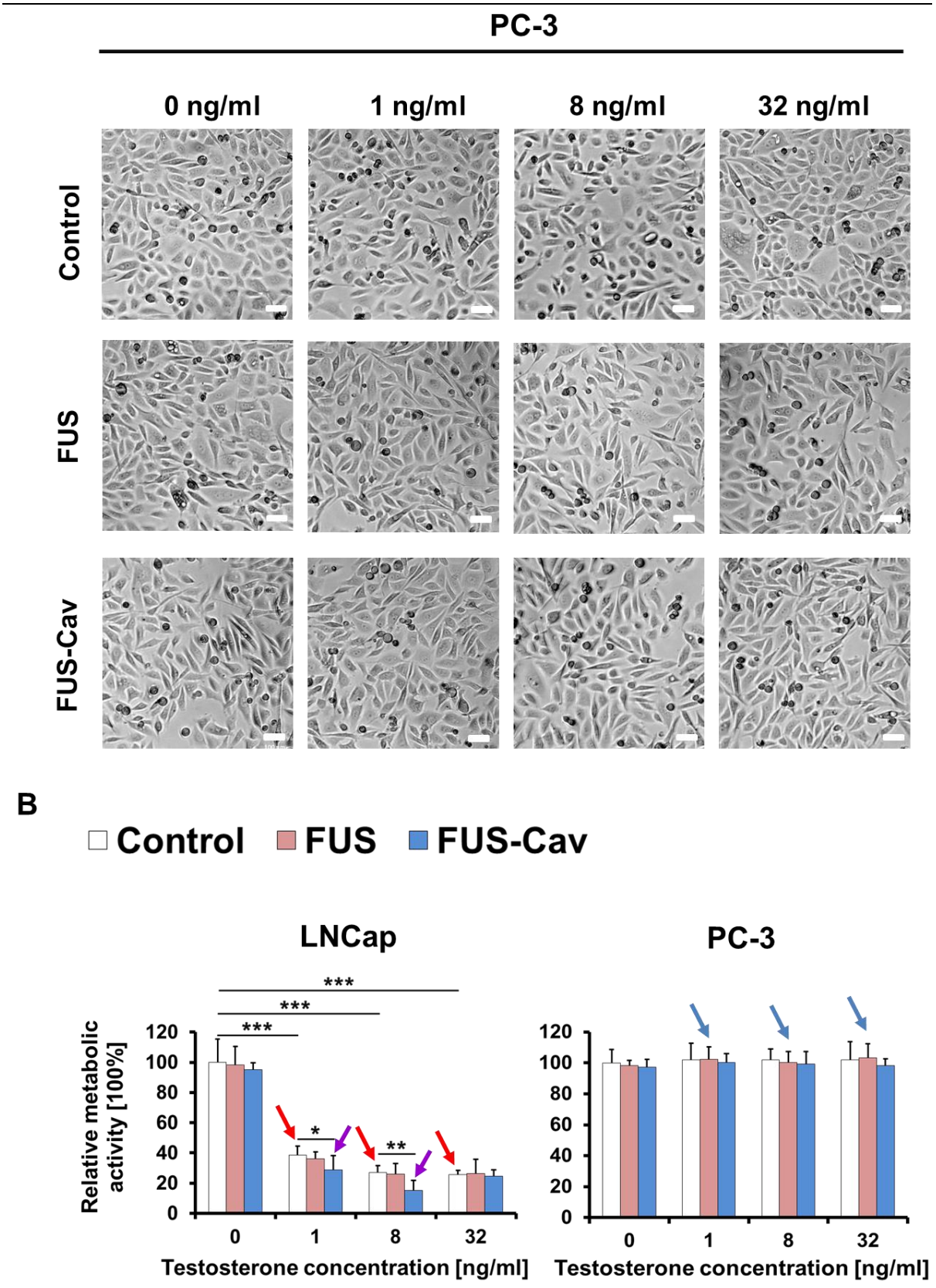

Figure 31: Long-term cultivation with testosterone of 1, 8, and 32 ng/mL led to a significant decrease of cell metabolic activity in LNCap cells. FUS/FUS-Cav supports the treatment of 1 or 8 ng/mL testosterone. LNCap and PC-3 cells were treated by FUS or FUS-Cav in the culture medium with

testosterone of 1, 8, 32 ng/mL. Afterwards, cells were cultured with these concentrations of testosterone for 8 or 12 days. At day 12 (for LNCap cells) and day 8 (for PC-3 cells), (A) cell morphology changes were observed by transmitted microscopy images, scale bar = 50 μm, red arrows: the reduced confluence of LNCap cells by testosterone treatment compared to untreated control in the absence of FUS/FUS-Cav; purple arrows： decreased confluence of LNCap cells in combination treatment (FUS-Cav + 1 or 8 ng/mL testosterone) compared to single treatment (1 or 8 ng/mL testosterone). (B) Relative cell metabolic activity of LNCap and PC-3 cells were measured with WST-1 assays post-treatment. Data were normalized to untreated control, which was set to 100 %, and relative values are presented as mean ± SEM, n = 6, * $p \leq 0.05$; ** $p \leq 0.01$; *** $p \leq 0.001$. Red arrows: significant reduction of LNCap cell relative metabolic activity by testosterone treatment compared to untreated control; purple arrows: significant reduction of LNCap cell relative metabolic activity in combination treatment (FUS-Cav + 1 or 8 ng/mL testosterone) compared to single treatment (1 or 8 ng/mL testosterone); blue arrows: neither the testosterone nor the combination treatment with FUS/FUS-Cav had impacts on the relative metabolic activity of PC-3 cell in long-term.

8 Discussion

In this thesis, FUS-induced cavitation was measured *in vitro* in a defined 96-well cell culture plate, and the short- and long-term effects of cavitation as a single treatment or an adjuvant therapy to radiation therapy, standard hyperthermia and testosterone treatment (only for prostate cancer) were investigated at the cellular and molecular levels in human prostate cancer (PC-3 and LNCap), glioblastoma (T98G) and head and neck (FaDu) cells *in vitro*. We hypothesize that FUS can induce cavitation in a defined 96-well cell culture plate, and the cavitation owns the potential to be a promising adjuvant therapy in the management of cancerous disease:

(1) The occurrence and acoustic intensity threshold of cavitation can be determined *in vitro* in a defined 96-well cell culture plate environment by FOH.

(2) The combination of FUS-induced cavitation and radiation therapy (RT) or water bath hyperthermia (HT) may lead to a significant decline in long-term cell clonogenic survival and short-term cell metabolic activity compared to single RT or HT. The potential mechanism is supposed to be cavitation-induced cell membrane changes and changes of 5α-reductase level in the AR signaling pathway of prostate cancer cells caused by combination treatment.

(3) The combination of FUS-induced cavitation and RT or HT may result in a significant reduction in prostate cancer cell potential to invade compared to RT or HT alone.

(4) The combination of FUS-induced cavitation and testosterone treatment may lead to a significant reduction of long-term cell metabolic activity for androgen-dependent prostate cancer cells compared to single testosterone treatment.

8.1 Cavitation measurement in a defined 96-well plate by PCD technique and sonochemistry method

The techniques for cavitation measurement mainly include sonoluminescence/sonochemistry methods, high-speed photography, laser scattering, synchrotron X-ray imaging technique, MRI techniques and active/passive cavitation detection (ACD/PCD). Table 12 provides a summary of various cavitation detection techniques and their related characteristics. Due to the limited applicability to the *in vivo* system, sonoluminescence/sonochemistry methods, high-speed photography, and laser scattering are rarely used for

in vivo and clinical cavitation monitoring.

Table 12: Summary of various cavitation detection techniques and characteristics

Cavitation detection technique	Measured features	Measurement modality	Advantages	Disadvantages	Reference
Sonoluminescence /sonochemistry methods	Light emissions Free radicals Electron-spin-resonance	Indirect measurement	Quantitative measurements Minimized interference to the acoustic field	Not applicable to *in vivo* system	(Matula, Hilmo, Bailey, & Crum, 2002; P. Li, Takahashi, & Chiba, 2009)
High-speed photography	Spatial and temporal oscillation or collapse of bubbles	Direct imaging	Visualization of dynamics of cavitated bubbles	Not applicable to *in vivo* system Limited field for visualization Not applicable for the view of bubble clouds	(Chen, 2011; Zahra Izadifar et al., 2019)
Laser scattering	Scattered light from cavitated bubbles	Indirect measurement	Exact determination of spherical-shaped cavitated bubble dynamics	Not applicable to *in vivo* system Only applies to the samples of small volumes	(Chen, 2011; Matula, Hilmo, Bailey, & Crum, 2002)
Synchrotron X-ray imaging technique	Scattered X-rays from cavitated bubbles	Indirect measurement	Providing existence and location of cavitated bubbles	Cannot give information about the size and behavior of a single bubble	(Z. Izadifar, Belev, Izadifar, Izadifar, & Chapman, 2014)
MRI techniques	Cavitation-induced thermal effects or flow turbulence	Indirect measurement	Clinical monitoring of cavitation	Not applicable for quantitative measurements	(Kopechek et al., 2014;; Elbes et al., 2014)

Active/passive cavitation detection	Acoustic emissions from cavitated bubbles	Indirect measurement	Imaging of cavitation field Clinical applicability Digital simulation precisely for cavitation events Quantitative measurements	Possible interference to cavitation field Unable to estimate the in situ exposure of ultrasound *in vivo*	(Duck, 1999; Zijlstra et al., 2009)

PCD technique and sonochemistry method were used in our study to measure the cavitation that occurred in 96-well plates. PCD technique refers to the passive records of acoustic emissions scattered from cavitated bubbles by various hydrophones or the special listening transducers (Figure 32). As a clinically applicable technique, PCD has been applied in clinical HIFU devices such as Sonalleve (Profound Medical, Mississauga, Canada) and ExAblate (Insightec, Haifa, Israel) to monitor the occurrence of cavitation. The sonochemistry method is widely accepted as an approach of inertial cavitation measurement with the advantage of no interference to the acoustic field.

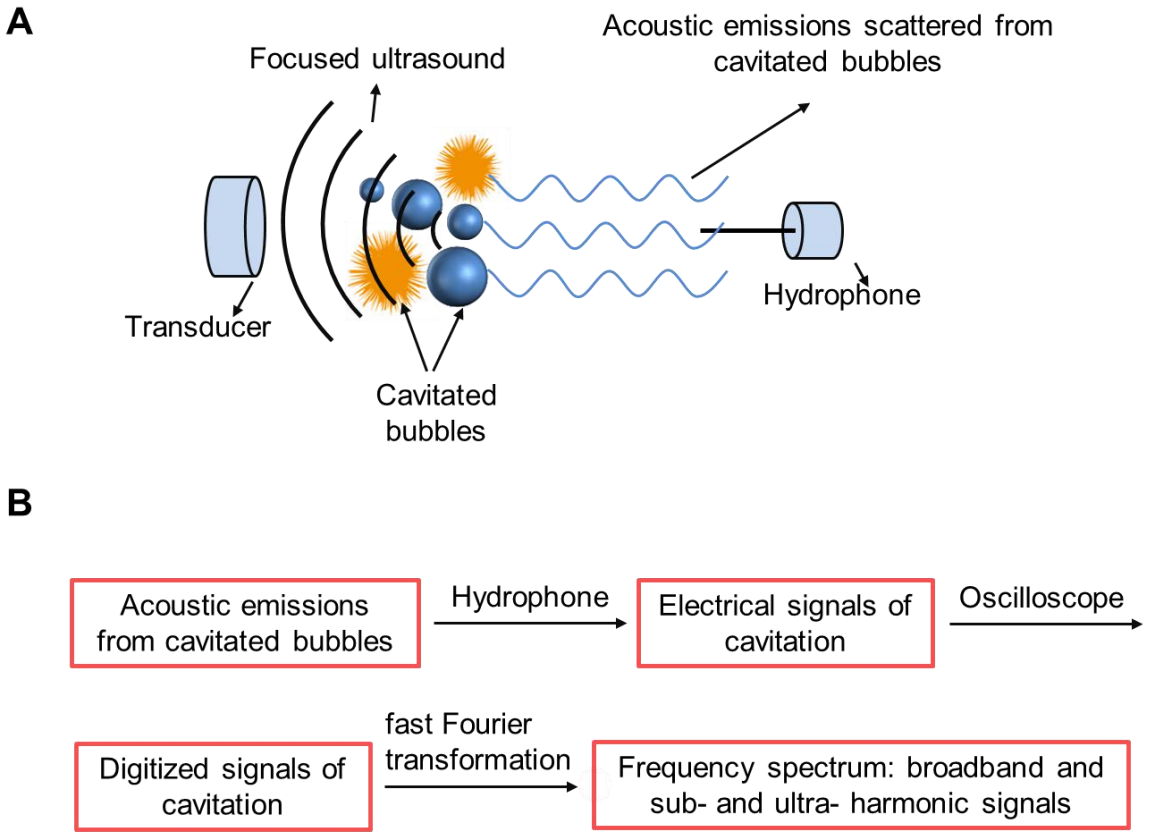

Figure 32: Schematic diagram shows the principle of cavitation measurement by PCD technique. (A) In the acoustic field, the acoustic emissions scattered from the cavitated bubbles are passively recorded by a hydrophone. (B) Electrical signals of cavitation detected by the hydrophone are digitized by an oscilloscope. The digitized signals of cavitation are processed by fast Fourier transformation (FFT) to form the frequency spectrum, in which the broadband and sub- and ultra- harmonic signals represent inertial and stable cavitation, respectively.

Due to the small and thin size, the FOH sensor is the only hydrophone detector that can be positioned inside the defined 96-well cell culture plate with the minimized interference for the acoustic field. The FOH method, belongs to the PCD technique, was selected as the primary method to detect the cavitation that occurred inside the 96-well plate in our study. As a method without interference to the acoustic field for cavitation measurement, the sonochemistry method (i.e. TA method) was utilized to validate the cavitation measurement results by FOH method. The results of our measurements showed that cavitation occurred at and above acoustic temporal-peak negative pressure (*PNP*) of 2.26 Mpa (corresponding to the acoustic intensity of 344 W/cm^2), and no cavitation occurred at and below *PNP* of 1.38 Mpa (corresponding to the acoustic intensity of 129 W/cm^2) of the 1.467 MHz transducer, indicating the cavitation threshold should be in the *PNP* range of 1.38 – 2.26 Mpa (i.e. acoustic intensity range of 129 –

344 W/cm^2).

Several previous studies from other researchers measured the cavitation using PCD or sonochemistry methods. In the study of Bull et al. (Bull, Civale, Rivens, & ter Haar, 2011), FOH was proved to be an eligible tool to measure the cavitation via the comparison with another standard cavitation detector. Another study demonstrated the excellent correlation between the production of free hydroxyl radicals and inertial cavitation dose determined by a needle hydrophone, indicating that TA method can be utilized to validate the cavitation measurement result by PCD technique (Somaglino, Bouchoux, Mestas, & Lafon, 2011). Cavitation threshold, is the minimum peak negative pressure (*PNP*) or acoustic intensity at which cavitation initiates to occur, can be determined by PCD technique and validated by TA method (Somaglino, Bouchoux, Mestas, & Lafon, 2011). The *PNP* of 1.4 Mpa was determined as the cavitation threshold for distilled water in a low volume chamber by Bustamante et al. (Bustamante & Cronin, 2019). Brüningk et al. (Brüningk, Rivens, Mouratidis, & Ter Haar, 2019) reported that cavitation occurred in water at acoustic intensities above 200 W/cm^2. It was also reported that the cavitation threshold in the deionized water was detected at the *PNP* of 1.5 – 3.0 Mpa by the PCD technique (Li et al., 2014). In this context, cavitation thresholds measured by other researchers are in agreement with our results. The inertial cavitation threshold determined by TA method in our experiment was compatible with FOH method, which is in accordance with the report of Somaglino et al. that TA method is an appropriate approach to validate the cavitation dose measured by the hydrophone method (Somaglino, Bouchoux, Mestas, & Lafon, 2011).

In this study, the measurement of cavitation dose was carried out in 96-well plates, with the same *in vitro* experimental setup as the biological experiments. This allows for establishing the correlation between acoustic waves and biological effects. In order to maintain a sterile environment and monitor the temperature in the 96-well plate in real-time without disturbing the acoustic field, it has so far not been probable to eliminate the reflections of acoustic waves at the medium/air interface and possible formation of the standing waves in the described *in vitro* FUS setup. However, the influence of acoustic reflections may not cause considerable errors in cavitation measurement. In the report of Robertson et al., the existence of acoustic reflections only reduced inertial cavitation dose by approximately 15%. The limitation of this study is the likely impact of acoustic reflections and standing waves on cells and cavitation measurement, and the acoustic parameters for the generation of cavitation require to be further optimized and validated using an *in vivo* model.

MRI and PCD techniques can be used in clinical devices to monitor cavitation. MRI techniques only detect the cavitation-induced physical responses to determine the occurrence of cavitation (as described in Medical and technical background 4.3.3.7). Quantitative measurements of cavitation by MRI techniques have not been achieved yet. Numerous studies have utilized PCD technology to quantify cavitation events for the evaluation of cavitation intensity. The integral of RMS value of cavitation signal measured by PCD over sonication time is termed as the cavitation dose, and the unit is mV*s, which was used in our study. Cavitation is avoided in most clinical MRI-guided HIFU ablation processes because it has the potential to damage normal tissue and affect MR thermometry. Using PCD technique to quantify the cavitation events was mostly conducted *in vitro.* Although PCD system has already applied in the MR-guided HIFU devices (e.g. Sonalleve (Profound Medical, Mississauga, Canada) and ExAblate (Insightec, Haifa, Israel)), the quantitative measurement of cavitation by PCD has not been widely investigated in clinical devices. Currently, multi-elements arrays based PCD system (passive cavitation imaging, PCI) can visualize the cavitation field (Salgaonkar, Datta, Holland, & Mast, 2009). However, it is now challenging for the clinic use to cover the histological lesions in patients (Zahra Izadifar et al., 2019). The integration of PCD into HIFU system is only to monitor cavitation events and avoid cavitation-related harm to healthy tissues or cavitation-caused artifacts for the MR thermometry during the treatments (Viallon et al., 2010). Hence, it is required to develop a set of standard procedures to quantify and control cavitation events based on PCD technology and to cover the targeted histological lesions in patients accurately in future research if the potential benefits of cavitation need to be harnessed in the clinic.

8.2 Short-term and long-term additive effects of FUS-Cav to RT or HT

In our study, the combination of radiation therapy (RT) and water bath hyperthermia (HT) revealed a significant decline in long-term cell clonogenic survival compared to single RT, betokening radio-sensitization effects of conventional HT as reported in other studies (van den Tempel et al., 2017; L. Zhu et al., 2019), in which the underlying mechanism was described as DNA repair damage of cancer cells caused by HT. Single FUS/FUS-Cav treatment showed deficient inhibitory effects on the long-term clonogenic survival and short-term metabolic activity of cancer cells, indicating short FUS shots with/without cavitation are less harmful to cancer cells than HT. However, the combination of FUS-Cav with RT led to a significant decrease of long-term cell clonogenic survival in all three types of cancer cell

lines compared to the single RT, revealing the long-term radio-sensitization effects of short FUS-induced cavitation. Notably, FUS-Cav exhibited comparable radio-additive effects like water bath HT in all cell lines, which means the equivalent radio-sensitization effects of HT are achieved by FUS-induced cavitation, whereas the treatment duration could be decreased dramatically. Especially in the prostate cancer PC-3 cell line, the radio-sensitization effects of FUS-Cav were even more significant than HT. Additionally, a higher reduction of metabolic activity of PC-3 cells by FUS-Cav + RT compared to single RT demonstrates the short-term radio-sensitization effects of FUS-induced cavitation. Our findings indicate that FUS-induced cavitation is an efficient means to improve the efficacy of RT. The concordant results in the *in vivo* studies have been previously reported in recent years. For example, the combination treatment of cavitation and RT showed an enhanced anti-tumor effect compared to single RT in New Zealand white rabbits bearing prostate tumor (PC-3) xenografts (McNabb et al., 2020). Localized cavitation of 2 – 3 min supported RT to treat hepatocellular carcinoma via the enhancement of tumor response in an orthotopic rat model in the study of Daecher (Daecher et al., 2017). El Kaffas et al. (El Kaffas et al., 2018) reported that the enhancement of RT was achieved by 5 min pre-treatment of ultrasound-stimulated MBs on a murine fibrosarcoma model and the underlying mechanism was described as the cavitation-induced tumor vascular shutdown.

HT treatment using water bath in the range of 39 – 45 °C was able to inhibit cancer cell proliferation and induce heat shock proteins to suppress tumor growth (Toraya-Brown & Fiering, 2014). HT is typically utilized in combination with other tumor therapies to improve efficacy (i.e. as a sensitizer for RT), but single HT treatment has also become a promising therapeutic strategy to treat cancer (Kang et al., 2020). In our study, short FUS shots were utilized to combine with water bath HT to investigate the synergistic effects of these two treatment modalities where the water bath HT could be later replaced in medical use by FUS-induced HT. Here, the combination treatment of FUS/FUS-Cav + HT led to a further significant reduction of long-term cell survival in all cell lines compared to the single water bath HT treatment, suggesting the additive effects of short FUS shots to water bath HT. FUS-Cav + HT resulted in a more significant reduction of long-term cell clonogenic survival than FUS + HT in PC-3 cells, which indicated that the FUS-induced cavitation might be more responsible for impacting PC-3 cells. FUS-induced cavitation also showed the short-term additive effects to HT because FUS-Cav combined with HT led to higher loss of cell metabolic activity than single HT in PC-3 cells. A great deal of literature reported that

cavitation-induced heating could reduce the acoustic power required for ultrasound-induced HT (Santos, Wu, Li, Goertz, & Hynynen, 2018; Yildirim et al., 2018; Zilonova, Solovchuk, & Sheu, 2019), whereas rare literature reported the impact of cavitation combined with HT on cancer cells. Our research clarifies that cavitation can biologically enhance the anti-tumor effects of HT, not just that the cavitation-induced heating physically promotes the achievement of HT. Although our findings demonstrate that FUS-induced cavitation can improve the efficacy of RT or HT significantly *in vitro*, no animal experiments have been carried out so far to validate these outcomes due to the limitation of current experimental equipment which cannot perform the quantitative measurement of cavitation. The next step should focus on the *in vivo* experiments to validate the additive effects of FUS-induced cavitation to RT or HT.

Currently, a lot of research about cavitation mainly focuses on the effects to cell membranes. Cavitation was reported to induce the deformation, damage or sonoporation on the membrane of cancer cells and was usually used to deliver therapeutic agents (e.g. drugs or gene fragments) to targeted cells. Besides, the impacts of cavitation on cell membranes were also reported to induce anti-proliferative effects on cancer cells. Cavitation-induced sonoporation on the membrane of cancer cells was reported to reduce the expression of polyadenosine diphosphate ribose polymerase (PARP) protein, a pro-apoptotic hallmark correlated to impairment of DNA repair functionality (Figure 33). Sonoporation was also found to suppress the expression of a variety of checkpoint proteins such as cyclin and Cdk (cyclin-dependent kinase) that play a vital role in cell-cycle progression and prolong the DNA-synthesis, thereby inducing cell-cycle arrest of cancer cells (Figure 33) (X. Chen, Wan, & Yu, 2013; Zhong, Sit, Wan, & Yu, 2011). Zhou et al. (Zhou, Yang, Cui, Ye, & Deng, 2012) reported that approximately half of the sonoporated KHT-C (mouse fibrosarcoma) cells could not maintain long-term cell survival after the ultrasound-mediated MBs. The potential impacts of ultrasound mechanical effects also include changes in cell ultrastructure, division ability, chromosomal and cytogenetic effects, and functions (Z. Izadifar, Babyn, & Chapman, 2017). In our research, sonoporation occurred in more PC-3 cells (49.9 %) than FaDu cells (23.3 %) immediately after short FUS shots with cavitation (FUS-Cav), revealing that PC-3 cells are more susceptible to cavitation, which might be the biophysical mechanism at the cellular level here leading to lower survival of PC-3 compared to FaDu cells in the combination treatments. Short FUS shots without cavitation (FUS) could not induce sonoporation in both cell lines, which is supposed to be the potential reason here leading to more additive effects induced by FUS-Cav than FUS to RT or HT. The extents and types of

anti-proliferative effects induced by sonoporation vary depending on cancer cell types (X. Chen et al., 2013; Karshafian et al., 2010; D. L. Miller & Dou, 2009; Zhong et al., 2011). Although FUS-induced cavitation was proved to induce sonoporation in prostate cancer cell line PC-3 and head and neck cancer cell line Fadu in our study, the subsequent anti-proliferative effects (e.g. cancer cell apoptosis, cell-cycle arrest or prolong of DNA-synthesis) are still required to be clarified in future research and validated in animal models.

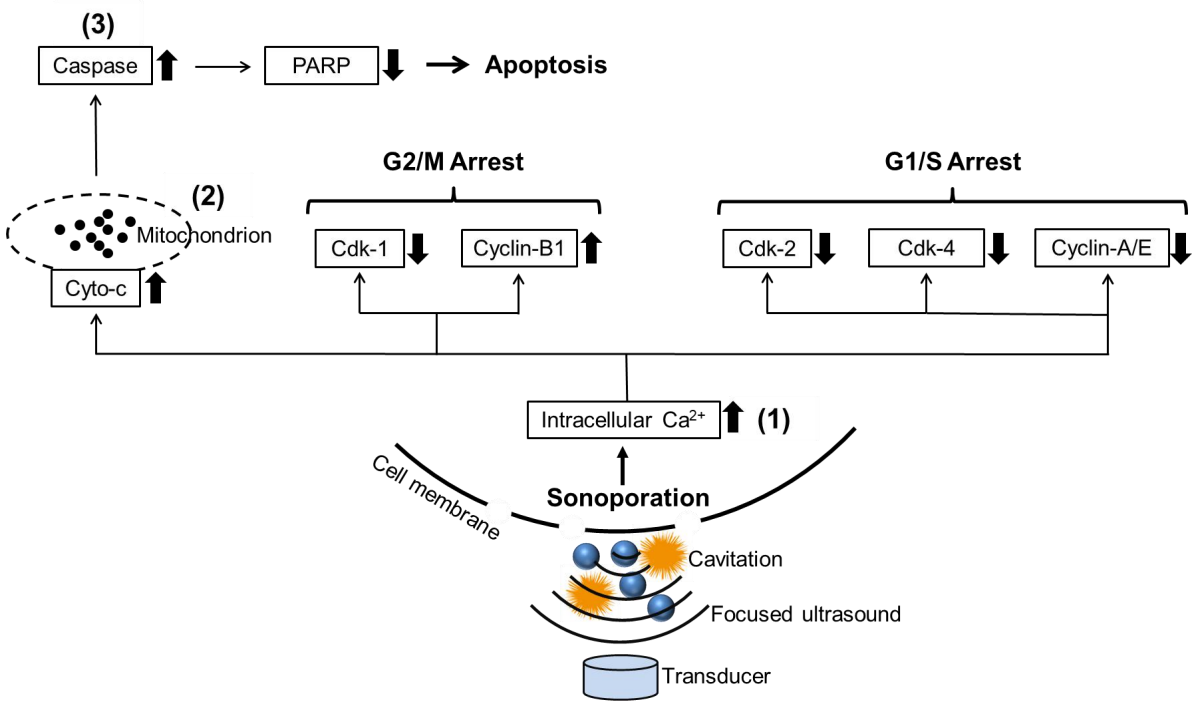

Figure 33: Schematic diagram reveals the possible mechanism of sonoporation-induced cell apoptosis and cell-cycle arrest. The transduction of intracellular signaling molecules involves (1) intracellular Ca^{2+} signaling system, (2) mitochondrion biology and (3) apoptosis signaling pathway. Cyto-c: cytochrome c, PARP: polyadenosine diphosphate ribose polymerase, Cdk: Cyclin-dependent kinases. Adapted from (Zhong et al., 2011).

5α-reductase (SRD5A) proteins were discovered to be associated with DHT generation and activation of AR signaling pathway in the prostate, and suppression of SRD5A3 protein level was reported to be a promising alternative therapy to block the AR signaling pathway and inhibit the growth of malignant prostate tumors (Godoy et al., 2011; Uemura et al., 2008). In our experiment, single FUS-Cav treatment demonstrated a minor inhibitory effect on the expression of SRD5A1 and SRD5A3 in PC-3 cells, whereas the combination treatment of FUS-Cav and water bath HT led to a significant reduction of SRD5A3 protein compared to single HT, revealing a dramatic suppressive effect on the expression of SRD5A3

protein induced by FUS-Cav + HT. Thus, a huge reduction of SRD5A3 protein in PC-3 cells might result in the inactivation of AR signaling pathway, leading to the inhibition of cell survival (Figure 34). In addition, the combination treatment of FUS-Cav + HT demonstrated more reduction of SRD5A3 protein level in PC-3 cells compared to FUS + HT, showing the greater additive effects of FUS-Cav to water bath HT on suppressing the SRD5A3 protein expression than FUS, which might be the underlying reason at the molecular level that PC-3 cells are more sensitive to FUS-induced cavitation than FUS without cavitation in the combination treatments. In another prostate cancer cell line LNCap, the combination treatment showed different inhibitory effects on SRD5A level. As an adjuvant therapy, FUS with cavitation supported HT to reduce SRD5A1 level but had no impact on SRD5A3, and FUS without cavitation could support HT to decrease both SRD5A1 and SRD5A3 level, suggesting that the suppressive effects of combination treatment for SRD5A proteins are cell-type dependent.

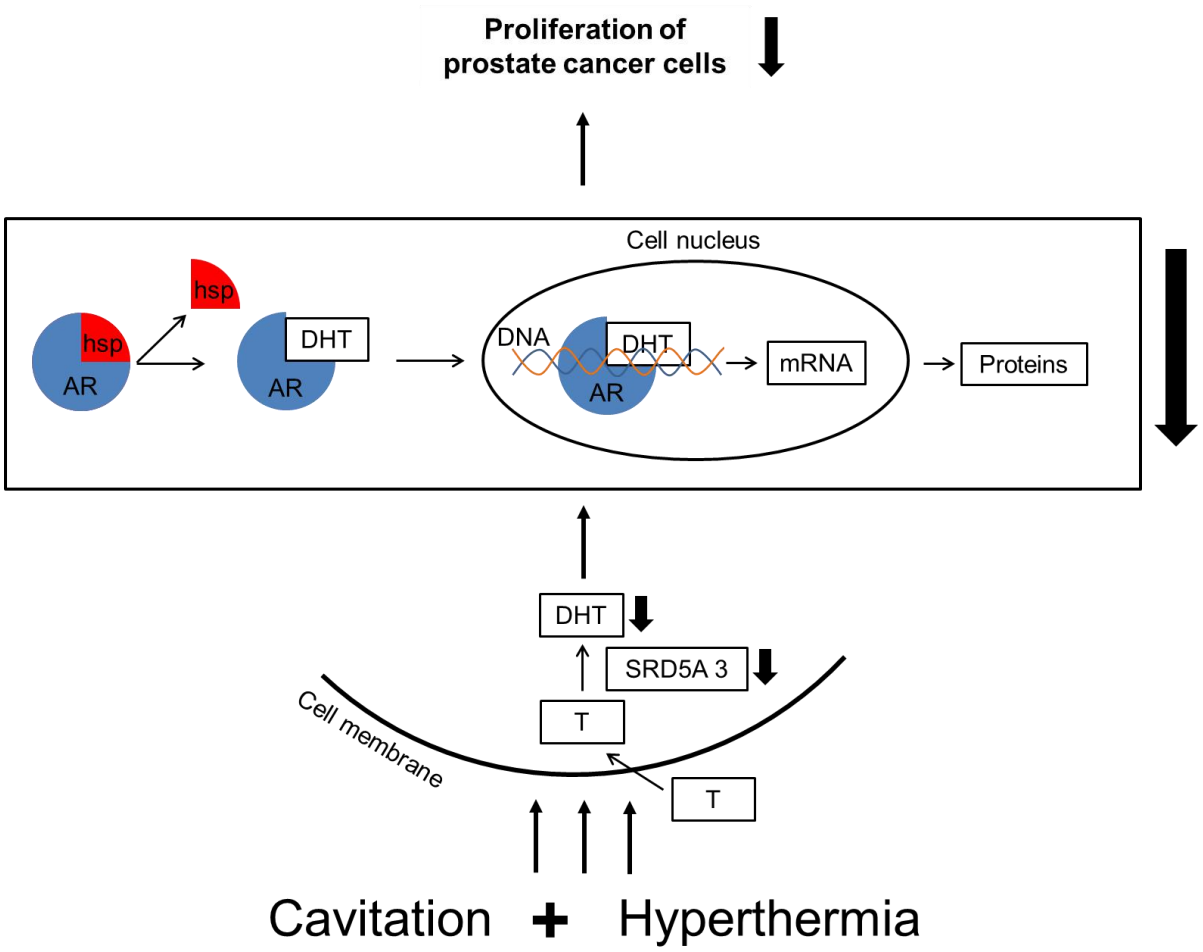

Figure 34: Changes in AR signaling pathway may lead to the suppression of proliferation of prostate cancer cells. The dramatic decline of SRD5A3 protein by the combination treatment of FUS-induced cavitation and HT results in the reduction of DHT generation, thus inactivating the AR signaling pathway and inhibiting the proliferation of prostate cancer cells. T: testosterone, DHT: dihydrotestosterone, AR: androgen receptor. This diagram was adapted from our findings and other published studies (Godoy et al., 2011; Meehan & Sadar, 2003; Uemura et al., 2008).

Radiotherapy resistance is the foremost reason for the clinical treatment failure after radiotherapy in localized prostate cancer and glioblastoma. Head and neck cancer is even characterized by high radiotherapy resistance (Ganci et al., 2015). The toxicity of high-dose radiotherapy may induce various adverse effects. Therefore, it is urgently required to reduce systemic toxicity and improve radiotherapy efficacy by overcoming radiotherapy resistance for the above tumors. Our findings demonstrate that 40 s high-intensity FUS shots with cavitation can generate comparable radio-additive effects to water bath HT at 37 °C for 30 min, which has guiding significance in the clinical radiation oncology, especially the RT

treatment for prostate cancer. Firstly, the shortening of the treatment duration in clinical practice could dramatically reduce the probability and degree of injury to the healthy tissues surrounding the tumor and simultaneously minimize treatment costs. Secondly, compared to the thermal effects of HT, the damaged tumor tissue residue caused by cavitation can be reabsorbed by neighboring tissue or excreted out by body orifices (Schade et al., 2012), allowing a faster recovery in the lesion after treatments, which might be of great benefits to the clinical prognosis in the patients. Finally, the radio-sensitization effect of short FUS shots with cavitation on certain cancer cells is even more significant than that of HT (e.g. the prostate cancer PC-3 in our study), which makes short high-intensity FUS shots possess great potential to become the first choice of adjuvant radio-sensitization methods in the clinic. Our findings also indicate that cavitation can sensitize cancer cells not only to RT but also to HT. FUS itself is a means to generate HT, thus the combination of FUS-induced HT combined with controlled cavitation would expand the anti-proliferative effects on tumors. Both the single treatment of cavitation and HT own radio-sensitization effects, thus the triple therapy of FUS-induced cavitation + HT + RT is supposed to maximize the anti-proliferative effect on tumors and might be a promising clinical tumor treatment strategy, which is required to be confirmed in future researches. The commercialized HIFU device TULSA (TULSA-PRO, Profound Medical, Toronto, Canada) is used for thermal ablation of prostate tumors in the clinic. However, the clinically used PCD technology can only detect the occurrence of cavitation. The precisely targeted characterization and control of cavitation cannot be achieved inside the solid tumors in patients yet. Moreover, the influence of cavitation on thermometry and the harm of uncontrollable cavitation to healthy tissues can lead to the interruption of HIFU running. Future work demands to focus on two aspects: i) the PCD technique need to be further developed to precisely quantify and control the cavitation events that occurred in the patients' tumors; ii) all the additive effects generated by cavitation to other treatment modalities require to be confirmed *in vivo* and in the clinic.

8.3 Inhibitory effects of FUS-cav in the potential of prostate cancer cells to invade

In our experiment, either the X-ray radiation therapy (RT) of 10 Gy or the treatment of water bath HT at 45 °C for 30 min led to a significant reduction of cell invasion of prostate cancer cells PC-3 compared to untreated control. Short FUS shots with cavitation (FUS-Cav) demonstrated a certain suppressive effect for the invasion of PC-3 cells, the pre-treatment to PC-3 cells with FUS-Cav significantly expanded the impact

of the subsequent RT or HT to inhibit cell invasion, exhibiting the additive effects of FUS-Cav to RT or HT on the suppression of PC-3 cell potential to invade in our study. In some other researches, the activation of phosphatidylinositol-3-kinase/AKT (PI3K/AKT) signaling pathway was discovered to be responsible for the migration and invasion of prostate cancer cells (Zhou et al., 2017). Ogata et al. (Ogata et al., 2011; Ogata et al., 2005) described that RT could inhibit the invasiveness of small cell lung cancer cell line A594 by the down-regulation of the matrix metalloproteinase (MMP)-2, which was attributed to the inactivation of the PI3K/AKT signaling pathway. However, this is not applied for all cancer cell lines because several *in vitro* and *in vivo* researches have published that RT might subsequently change tumor metastasis by reducing or raising the invasiveness of the residual cancer cells after radiation, which appeared to vary depending on the radiation pattern and dose, as well as the studied cell lines (Fujita, Yamada, & Imai, 2015). HT was previously shown to inhibit cancer cell invasion via the down-regulation of metastatic-related proteins, MMP-2 and MMP-9 (Xie et al., 2011). In numerous studies, the expression of MMP-2/9 is usually associated with the PI3K/AKT signaling pathway (Adya, Tan, Punn, Chen, & Randeva, 2008; J. S. Chen et al., 2009; Guo et al., 2014; Ogata et al., 2005; W. Zhu et al., 2019), the suppression of the PI3K/AKT signaling pathway in PC-3 cells could result in the down-regulation of MMP-2/9 (Chien, Shen, Huang, Ko, & Shih, 2010). It has been previously reported that the cavitation effects were able to hinder the invasion and migration of PC-3 cells via down-regulation of the MMP-2/9 (Wei, Bai, Wang, & Hu, 2014). Based on the literature reports, all RT, HT, and cavitation could inhibit the invasion of cancer cells in varying degrees by hindering cancer metastatic-related proteins MMPs. We assume that the combination of cavitation with RT or HT carries the potential to reduce the expression of MMPs compared to single treatments, which is supposed to be the underlying mechanism of cavitation-induced additive effects to RT or HT on the inhibition of the PC-3 cell potential to invade. The inhibition of MMPs might be associated with the inactivation of the PI3K/AKT signaling pathway. However, the association between combination treatment of FUS-induced cavitation and RT or HT and the down-regulation of MMPs in prostate cancer cells has so far not been clarified in our study. It is necessary to validate these assumptions regarding the changes at the molecular level to clarify the mechanism of cavitation-induced inhibitory effects on cancer cell invasion in future research.

In clinical practice, the leading cause of prostate cancer-related death is cancer metastasis (Li et al., 2014). Patients with metastatic prostate cancer have a poor quality of life and usually suffer from urinary retention

and bone pain (Kiljunen et al., 2015). Cancer cell migration is the crucial step for the cancer progression to metastatic state (Dirat et al., 2015). It is necessary to find an approach to reduce the potential of cancer cells to invade for slowing the progression of prostate cancer. From our studies, short FUS shots with cavitation sensitize prostate cancer PC-3 cells to RT or HT, inhibiting not only the short- and long-term survival as mentioned above but also the cell potential to invade, which provides a novel strategy to reduce the potential to spread cancer cells through the body leading to cancer metastasis. However, the additive effects of FUS-induced cavitation to RT or HT still require to be validated *in vivo* and in the clinic.

8.4 The reduction of the long-term metabolic activity of androgen-dependent prostate cancer cells by the combination treatment of FUS-Cav and testosterone

Our experimental results showed that the combination treatment of FUS-Cav and testosterone resulted in a significant reduction of long-term cell metabolic activity in LNCap cells compared to the single treatments with testosterone, suggesting the additive effects of FUS-induced cavitation to testosterone treatment. Testosterone suppressed the long-term metabolic activity of androgen-dependent prostate cancer cell line LNCap *in vitro*, whereas it had no impact on the androgen-independent prostate cancer PC-3 cells. This is consistent with the study reported by Song et al. (Song & Khera, 2014) that the normal physiological concentrations of testosterone in serum (2.4 – 9.5 ng/mL) suppressed the proliferation of androgen-dependent prostate cancer cells *in vitro*. Cavitation was reported to induce cell membrane permeability enhancement, which was typically used for the targeted delivery of therapeutic molecules into cancer cells (Qin, Wang, & Willmann, 2016; Zhou et al., 2012). We assume that the enhancement of cancer cell membrane permeability caused by FUS-induced cavitation increases the sensitivity of cancer cells to testosterone, thereby causing more inhibitory effects of combination treatments.

The complexity and duality of testosterone in prostate cancer development were reported in fundamental and clinical researches in recent years. Whether to promote or inhibit the growth and development of prostate cancer depends on the concentration of testosterone (Barqawi & Crawford, 2006; Hoffman, DeWolf, & Morgentaler, 2000; Lane, Stephenson, Magi-Galluzzi, Lakin, & Klein, 2008; Song & Khera, 2014). In the *in vitro* study of Song et al. (Song & Khera, 2014), prostate cancer cells will not proliferate without testosterone, and the proliferation will be slowed when testosterone concentration is extremely low (e.g. castration levels of testosterone). Prostate cancer cells will grow normally at low testosterone levels,

and the growth will be suppressed by normal physiological concentrations of testosterone (i.e. 2.4 – 9.5 ng/mL), demonstrating that the growth of prostate cancer cells requires a low level of testosterone and normal physiological level of testosterone will inhibit the proliferation *in vitro*. Testosterone replacement therapy enables the serum testosterone of men to return to normal physiological levels. In clinical practice, testosterone replacement therapy may not enhance prostate cancer risk, and it even reduces the risk of highly aggressive prostate cancer (Barqawi & Crawford, 2006). According to our experimental results, FUS-induced cavitation enhanced the inhibitory effects of treatment with testosterone at normal physiological levels for prostate cancer cells *in vitro*. We may provide a new strategy for prostate cancer therapy in the clinic for the patients whose serum testosterone levels have been restored by testosterone replacement therapy. However, all the additive effects induced by cavitation to the testosterone treatment require to be validated *in vivo* and in the clinic in future researches.

9 Conclusion

In this thesis, the bio-effects of FUS-induced cavitation were investigated as a single or adjuvant therapy in the treatment of various cancer types. Using a customized *in vitro* FUS system, effects of FUS-induced cavitation were assessed via a series of biological experiments at the cellular and molecular level. The major conclusions we have drawn validate our hypothesis that FUS-induced cavitation may increase the effects of radiation therapy, hyperthermia and testosterone treatment by interrupting the cancer cell membrane and changing the AR signaling pathway of the prostate cancer cells, with the potential to be a promising adjuvant therapy in cancer treatment: (1) Detailed characterization of the *in vitro* FUS system and definition of the acoustic parameters to generate cavitation reveal that either stable or inertial cavitation occurs at and above 337 W/cm^2 for 0.487 MHz, 213 W/cm^2 for 1.142 MHz and 344 W/ cm^2 for 1.467 MHz in special ultrasound penetrable 96-well μ-clear cell culture plates and the cavitation dose increases nonlinearly with the enhancement of the acoustic intensity. (2) As a single treatment, FUS (short FUS shots with or without cavitation) alone exhibits limited impact on the long-term clonogenic survival of cancer cells and has slight short-term suppressive effects on the potential to invade and metabolic activity of prostate cancer cells. (3) As an adjuvant therapy, FUS demonstrates significant long-term additive effects to RT or HT at the cellular level showing the reduction of cell clonogenic survival. The long-term radio-additive effects caused by FUS-induced cavitation are comparable with HT at 45 °C for 30 min while the treatment duration is reduced dramatically to 2 min, especially for prostate cancer cells. Besides, FUS can also significantly increase the sensitivity of prostate cancer cells to RT or HT by decreasing short-term cell potential to invade and metabolic activity. The short-term additive effects of FUS with cavitation to RT or HT are over FUS without cavitation. (4) FUS-induced cavitation causes sonoporation immediately generating pores on cancer cell membrane temporarily, which is supposed to be the cellular underlying mechanism of FUS-induced additive effects to other therapies. The occurrence of sonoporation is cell type-dependent. (5) The combination of FUS as adjuvant therapy and other therapies leads to the reduction of the SRD5A3 protein level in prostate cancer cells and thus may promote the inactivation of the androgen signaling pathway, which might be the molecular underlying mechanism of FUS-induced additive effects to other therapies. (6) FUS-induced cavitation combined with the normal physiological level of testosterone shows dramatically *in vitro* suppressive effects for long-term metabolic

activity of androgen-dependent prostate cancer cells compared to single testosterone treatment, whereas the combination treatment has no impact on the androgen-independent prostate cancer cells.

Short FUS treatment with cavitation demonstrated great potential as an efficient approach to accurately and less-invasively enhance the effects of RT, HT or testosterone treatment and may provide opportunities for less-invasive adjuvant therapy in the future. The FUS-induced cavitation provides an extended potential to overcome the radiation resistance of cancer cells compared to HT as the conventional adjuvant therapy to RT. The next essential steps to drive research and application of FUS-induced cavitation forward would be the investigation in animals and in the clinic. In addition, at the technical level, the standard procedures for clinically accurate quantification of cavitation events and the controlling of different cavitation doses that can accurately cover the target histological lesion area of the patient require to be implemented in future research.

10 References

Adya, R., Tan, B. K., Punn, A., Chen, J., & Randeva, H. S. (2008). Visfatin induces human endothelial VEGF and MMP-2/9 production via MAPK and PI3K/Akt signalling pathways: novel insights into visfatin-induced angiogenesis. *Cardiovasc Res, 78*(2), 356-365. doi:10.1093/cvr/cvm111

Afadzi, M., Davies Cde, L., Hansen, Y. H., Johansen, T., Standal, O. K., Hansen, R., . . . Angelsen, B. (2012). Effect of ultrasound parameters on the release of liposomal calcein. *Ultrasound Med Biol, 38*(3), 476-486. doi:10.1016/j.ultrasmedbio.2011.11.017

Algan, O., Fosmire, H., Hynynen, K., Dalkin, B., Cui, H., Drach, G., . . . Cassady, J. R. (2000). External beam radiotherapy and hyperthermia in the treatment of patients with locally advanced prostate carcinoma. *Cancer, 89*(2), 399-403. Retrieved from http://www.ncbi.nlm.nih.gov/pubmed/10918172

Alvarez, A., Preston, C., Trujillo, T., Wilhite, C., Burton, A., Vohnout, S., & Witte, R. S. (2020). In vivo acoustoelectric imaging for high-resolution visualization of cardiac electric spatiotemporal dynamics. *Appl Opt, 59*(36), 11292-11300. doi:10.1364/AO.410172

Anassi, E., & Ndefo, U. A. (2011). Sipuleucel-T (provenge) injection: the first immunotherapy agent (vaccine) for hormone-refractory prostate cancer. *P T, 36*(4), 197-202. Retrieved from http://www.ncbi.nlm.nih.gov/pubmed/21572775

Atchley, A. A., Frizzell, L. A., Apfel, R. E., Holland, C. K., Madanshetty, S., & Roy, R. A. (1988). Thresholds for cavitation produced in water by pulsed ultrasound. *Ultrasonics, 26*(5), 280-285. doi:10.1016/0041-624x(88)90018-2

Aus, G. (2006). Current status of HIFU and cryotherapy in prostate cancer--a review. *Eur Urol, 50*(5), 927-934; discussion 934. doi:10.1016/j.eururo.2006.07.011

Azuma, T., Matayoshi, Y., Sato, Y., & Nagase, Y. (2018). Effect of dutasteride on castration-resistant prostate cancer. *Mol Clin Oncol, 8*(1), 133-136. doi:10.3892/mco.2017.1480

Barati, A. H., Mokhtari-Dizaji, M., Mozdarani, H., Bathaie, Z., & Hassan, Z. M. (2007). Effect of exposure parameters on cavitation induced by low-level dual-frequency ultrasound. *Ultrason Sonochem, 14*(6), 783-789. doi:10.1016/j.ultsonch.2006.12.016

Barnett, S. B., & Kossoff, G. (1984). Temporal peak intensity as a critical parameter in ultrasound dosimetry. *J Ultrasound Med, 3*(9), 385-389. doi:10.7863/jum.1984.3.9.385

Barqawi, A., & Crawford, E. D. (2006). Testosterone replacement therapy and the risk of prostate cancer. Is there a link? *Int J Impot Res, 18*(4), 323-328. doi:10.1038/sj.ijir.3901418

Beerlage, H. P., van Leenders, G. J., Oosterhof, G. O., Witjes, J. A., Ruijter, E. T., van de Kaa, C. A., . . . de la Rosette, J. J. (1999). High-intensity focused ultrasound (HIFU) followed after one to two weeks by radical retropubic prostatectomy: results of a prospective study. *Prostate, 39*(1), 41-46. doi:10.1002/(sici)1097-0045(19990401)39:1<41::aid-pros7>3.0.co;2-5

Bianco, F. J., Jr., Scardino, P. T., & Eastham, J. A. (2005). Radical prostatectomy: long-term cancer control and recovery of sexual and urinary function ("trifecta"). *Urology, 66*(5 Suppl), 83-94. doi:10.1016/j.urology.2005.06.116

Brüningk, S. C., Rivens, I., Mouratidis, P., & Ter Haar, G. (2019). Focused Ultrasound-Mediated Hyperthermia in Vitro: An Experimental Arrangement for Treating Cells under Tissue-Mimicking Conditions. Ultrasound Med Biol, 45(12), 3290-3297. doi:10.1016/j.ultrasmedbio.2019.06.410

References

Bull, V., Civale, J., Rivens, I., & ter Haar, G. (2011). Cavitation Detection Using a Fibre-Optic Hydrophone: A Pilot Study. Paper presented at the AIP Conference Proceedings.

Bull, V., Civale, J., Rivens, I., & Ter Haar, G. (2013). A comparison of acoustic cavitation detection thresholds measured with piezo-electric and fiber-optic hydrophone sensors. *Ultrasound Med Biol, 39*(12), 2406-2421. doi:10.1016/j.ultrasmedbio.2013.06.010

Burdin, F., Tsochatzidis, N. A., Guiraud, P., Wilhelm, A. M., & Delmas, H. (1999). Characterisation of the acoustic cavitation cloud by two laser techniques. *Ultrason Sonochem, 6*(1-2), 43-51. doi:10.1016/s1350-4177(98)00035-2

Bustamante, M. C., & Cronin, D. S. (2019). Cavitation threshold evaluation of porcine cerebrospinal fluid using a Polymeric Split Hopkinson Pressure Bar-Confinement chamber apparatus. *J Mech Behav Biomed Mater, 100*, 103400. doi:10.1016/j.jmbbm.2019.103400

Cafarelli, A., Chanel, L. A., Di Bartolo, F., Locteau, H., Tognarelli, S., Dumont, E., & Menciassi, A. (2018). Ultrasound Acoustic Radiation Force Impulse imaging for High Intensity Focused Ultrasound focal spot localization. Annu Int Conf IEEE Eng Med Biol Soc, 2018, 5713-5716. doi:10.1109/EMBC.2018.8513591

Canney, M. S., Bailey, M. R., Crum, L. A., Khokhlova, V. A., & Sapozhnikov, O. A. (2008). Acoustic characterization of high intensity focused ultrasound fields: a combined measurement and modeling approach. *J Acoust Soc Am, 124*(4), 2406-2420. doi:10.1121/1.2967836

Chaussy, C. G., & Thüroff, S. (2017). *Radical HIFU in localized prostate cancer.* Paper presented at the AIP Conference Proceedings.

Chen, H. (2011). *Ultra-high speed optical imaging of ultrasound-activated microbubbles in mesenteric microvessels.* Washington, DC: University of Washington.

Chen, J. S., Wang, Q., Fu, X. H., Huang, X. H., Chen, X. L., Cao, L. Q., . . . Zhang, L. J. (2009). Involvement of PI3K/PTEN/AKT/mTOR pathway in invasion and metastasis in hepatocellular carcinoma: Association with MMP-9. Hepatol Res, 39(2), 177-186. doi:10.1111/j.1872-034X.2008.00449.x

Chen, W., Zouboulis, C. C., Fritsch, M., Blume-Peytavi, U., Kodelja, V., Goerdt, S., . . . Orfanos, C. E. (1998). Evidence of heterogeneity and quantitative differences of the type 1 5alpha-reductase expression in cultured human skin cells--evidence of its presence in melanocytes. *J Invest Dermatol, 110*(1), 84-89. doi:10.1046/j.1523-1747.1998.00080.x

Chen, X., Wan, J. M., & Yu, A. C. (2013). Sonoporation as a cellular stress: induction of morphological repression and developmental delays. *Ultrasound Med Biol, 39*(6), 1075-1086. doi:10.1016/j.ultrasmedbio.2013.01.008

Chien, C. S., Shen, K. H., Huang, J. S., Ko, S. C., & Shih, Y. W. (2010). Antimetastatic potential of fisetin involves inactivation of the PI3K/Akt and JNK signaling pathways with downregulation of MMP-2/9 expressions in prostate cancer PC-3 cells. *Mol Cell Biochem, 333*(1-2), 169-180. doi:10.1007/s11010-009-0217-z

Cihoric, N., Tsikkinis, A., van Rhoon, G., Crezee, H., Aebersold, D. M., Bodis, S., . . . Ghadjar, P. (2015). Hyperthermia-related clinical trials on cancer treatment within the ClinicalTrials.gov registry. *Int J Hyperthermia, 31*(6), 609-614. doi:10.3109/02656736.2015.1040471

Cleveland, R. O., Sapozhnikov, O. A., Bailey, M. R., & Crum, L. A. (2000). A dual passive cavitation detector for localized detection of lithotripsy-induced cavitation in vitro. *J Acoust Soc Am, 107*(3), 1745-1758. doi:10.1121/1.428572

Cochran, S. A., & Prausnitz, M. R. (2001). Sonoluminescence as an indicator of cell membrane disruption by acoustic cavitation. *Ultrasound Med Biol, 27*(6), 841-850. doi:10.1016/s0301-5629(01)00382-9

Crea, F., Watahiki, A., Quagliata, L., Xue, H., Pikor, L., Parolia, A., . . . Helgason, C. D. (2014). Identification of a long non-coding RNA as a novel biomarker and potential therapeutic target for metastatic prostate cancer. *Oncotarget, 5*(3), 764-774. doi:10.18632/oncotarget.1769

Daecher, A., Stanczak, M., Liu, J. B., Zhang, J., Du, S., Forsberg, F., . . . Eisenbrey, J. R. (2017). Localized microbubble cavitation-based antivascular therapy for improving HCC treatment response to radiotherapy. *Cancer Lett, 411*, 100-105. doi:10.1016/j.canlet.2017.09.037

Dirat, B., Ader, I., Golzio, M., Massa, F., Mettouchi, A., Laurent, K., . . . Bost, F. (2015). Inhibition of the GTPase Rac1 mediates the antimigratory effects of metformin in prostate cancer cells. Mol Cancer Ther, 14(2), 586-596. doi:10.1158/1535-7163.MCT-14-0102

Dromi, S., Frenkel, V., Luk, A., Traughber, B., Angstadt, M., Bur, M., . . . Wood, B. J. (2007). Pulsed-high intensity focused ultrasound and low temperature-sensitive liposomes for enhanced targeted drug delivery and antitumor effect. *Clin Cancer Res, 13*(9), 2722-2727. doi:10.1158/1078-0432.CCR-06-2443

Duck, F. A. (1999). Acoustic saturation and output regulation. Ultrasound Med Biol, 25(6), 1009-1018.

Elbes, D., Denost, Q., Robert, B., Kohler, M. O., Tanter, M., & Bruno, Q. (2014). Magnetic resonance imaging for the exploitation of bubble-enhanced heating by high-intensity focused ultrasound: a feasibility study in ex vivo liver. Ultrasound Med Biol, 40(5), 956-964. doi:10.1016/j.ultrasmedbio.2013.11.019

El Kaffas, A., Gangeh, M. J., Farhat, G., Tran, W. T., Hashim, A., Giles, A., & Czarnota, G. J. (2018). Tumour Vascular Shutdown and Cell Death Following Ultrasound-Microbubble Enhanced Radiation Therapy. *Theranostics, 8*(2), 314-327. doi:10.7150/thno.19010

Engel, J., Bastian, P. J., Baur, H., Beer, V., Chaussy, C., Gschwend, J. E., . . . Holzel, D. (2010). Survival benefit of radical prostatectomy in lymph node-positive patients with prostate cancer. *Eur Urol, 57*(5), 754-761. doi:10.1016/j.eururo.2009.12.034

Feril, L. B., Jr., & Kondo, T. (2004). Biological effects of low intensity ultrasound: the mechanism involved, and its implications on therapy and on biosafety of ultrasound. *J Radiat Res, 45*(4), 479-489. doi:10.1269/jrr.45.479

Franken, N. A., Rodermond, H. M., Stap, J., Haveman, J., & van Bree, C. (2006). Clonogenic assay of cells in vitro. *Nat Protoc, 1*(5), 2315-2319. doi:10.1038/nprot.2006.339

Frisbie, R. (2020). HistoSonics Initiates First Liver Tumor Clinical Trial in the US. *2020 meeting of the Society of Interventional Oncology*.

Fujita, M., Yamada, S., & Imai, T. (2015). Irradiation induces diverse changes in invasive potential in cancer cell lines. *Semin Cancer Biol, 35*, 45-52. doi:10.1016/j.semcancer.2015.09.003

Ganci, F., Sacconi, A., Manciocco, V., Spriano, G., Fontemaggi, G., Carlini, P., & Blandino, G. (2015). Radioresistance in head and neck squamous cell carcinoma—possible molecular markers for local recurrence and new putative therapeutic strategies. *Contemporary Issues in Head and Neck Cancer Management*, 3-34

Godoy, A., Kawinski, E., Li, Y., Oka, D., Alexiev, B., Azzouni, F., . . . Mohler, J. L. (2011). 5alpha-reductase type 3 expression in human benign and malignant tissues: a comparative analysis during prostate cancer progression. *Prostate, 71*(10), 1033-1046. doi:10.1002/pros.21318

Goldenberg, L., So, A., Fleshner, N., Rendon, R., Drachenberg, D., & Elhilali, M. (2009). The role of

5-alpha reductase inhibitors in prostate pathophysiology: Is there an additional advantage to inhibition of type 1 isoenzyme? *Can Urol Assoc J, 3*(3 Suppl 2), S109-114. doi:10.5489/cuaj.1114

Gorchakov, A. A., Kulemzin, S. V., Kochneva, G. V., & Taranin, A. V. (2020). Challenges and Prospects of Chimeric Antigen Receptor T-cell Therapy for Metastatic Prostate Cancer. *Eur Urol, 77*(3), 299-308. doi:10.1016/j.eururo.2019.08.014

Gourevich, D., Dogadkin, O., Volovick, A., Wang, L., Gnaim, J., Cochran, S., & Melzer, A. (2013). Ultrasound-mediated targeted drug delivery with a novel cyclodextrin-based drug carrier by mechanical and thermal mechanisms. *J Control Release, 170*(3), 316-324. doi:10.1016/j.jconrel.2013.05.038

Gravis, G., Audenet, F., Irani, J., Timsit, M. O., Barthelemy, P., Beuzeboc, P., . . . Rozet, F. (2017). Chemotherapy in hormone-sensitive metastatic prostate cancer: Evidences and uncertainties from the literature. *Cancer Treat Rev, 55*, 211-217. doi:10.1016/j.ctrv.2016.09.008

Guo, J., Jie, W., Shen, Z., Li, M., Lan, Y., Kong, Y., . . . Zheng, S. (2014). SCF increases cardiac stem cell migration through PI3K/AKT and MMP2/9 signaling. *Int J Mol Med, 34*(1), 112-118. doi:10.3892/ijmm.2014.1773

Guo, X., Zhang, C., Guo, Q., Xu, Y., Feng, G., Li, L., . . . Wang, G. (2018). The homogeneous and heterogeneous risk factors for the morbidity and prognosis of bone metastasis in patients with prostate cancer. *Cancer Manag Res, 10*, 1639-1646. doi:10.2147/CMAR.S168579

Gyongy, M., & Coussios, C. C. (2010). Passive cavitation mapping for localization and tracking of bubble dynamics. *J Acoust Soc Am, 128*(4), EL175-180. doi:10.1121/1.3467491

Hashimoto, K., Tabata, H., Shindo, T., Tanaka, T., Hashimoto, J., Inoue, R., . . . Sapporo Medical University Urologic Oncology, C. (2019). Serum testosterone level is a useful biomarker for determining the optimal treatment for castration-resistant prostate cancer. *Urol Oncol, 37*(7), 485-491. doi:10.1016/j.urolonc.2019.04.026

Hassan, M. A., Campbell, P., & Kondo, T. (2010). The role of Ca(2+) in ultrasound-elicited bioeffects: progress, perspectives and prospects. *Drug Discov Today, 15*(21-22), 892-906. doi:10.1016/j.drudis.2010.08.005

Hirshburg, J. M., Kelsey, P. A., Therrien, C. A., Gavino, A. C., & Reichenberg, J. S. (2016). Adverse Effects and Safety of 5-alpha Reductase Inhibitors (Finasteride, Dutasteride): A Systematic Review. *J Clin Aesthet Dermatol, 9*(7), 56-62. Retrieved from http://www.ncbi.nlm.nih.gov/pubmed/27672412

Hoerig, C. L., Serrone, J. C., Burgess, M. T., Zuccarello, M., & Mast, T. D. (2014). Prediction and suppression of HIFU-induced vessel rupture using passive cavitation detection in an ex vivo model. *J Ther Ultrasound, 2*, 14. doi:10.1186/2050-5736-2-14

Hoffman, M. A., DeWolf, W. C., & Morgentaler, A. (2000). Is low serum free testosterone a marker for high grade prostate cancer? *J Urol, 163*(3), 824-827. Retrieved from http://www.ncbi.nlm.nih.gov/pubmed/10687985

Holland, C. K., Deng, C. X., Apfel, R. E., Alderman, J. L., Fernandez, L. A., & Taylor, K. J. (1996). Direct evidence of cavitation in vivo from diagnostic ultrasound. *Ultrasound Med Biol, 22*(7), 917-925. doi:10.1016/0301-5629(96)00083-x

Hong, Z., Pan, X., Chen, P., Su, X., Wang, N., & Lu, W. (2018). A Topology Control with Energy Balance in Underwater Wireless Sensor Networks for IoT-Based Application. *Sensors (Basel), 18*(7). doi:10.3390/s18072306

Huber, P., Debus, J., Peschke, P., Hahn, E. W., & Lorenz, W. J. (1994). In vivo detection of ultrasonically induced cavitation by a fibre-optic technique. *Ultrasound Med Biol, 20*(8), 811-825. doi:10.1016/0301-5629(94)90038-8

Huggins, C., & Hodges, C. V. (1941). Studies on prostatic cancer. I. The effect of castration, of estrogen and androgen injection on serum phosphatases in metastatic carcinoma of the prostate. *CA Cancer J Clin, 22*(4), 232-240. doi:10.3322/canjclin.22.4.232

Hurwitz, M., & Stauffer, P. (2014). Hyperthermia, radiation and chemotherapy: the role of heat in multidisciplinary cancer care. *Semin Oncol, 41*(6), 714-729. doi:10.1053/j.seminoncol.2014.09.014

Hurwitz, M. D., Kaplan, I. D., Hansen, J. L., Prokopios-Davos, S., Topulos, G. P., Wishnow, K., . . . Hynynen, K. (2005). Hyperthermia combined with radiation in treatment of locally advanced prostate cancer is associated with a favourable toxicity profile. *Int J Hyperthermia, 21*(7), 649-656. doi:10.1080/02656730500331967

Husseini, G. A., & Pitt, W. G. (2008). Micelles and nanoparticles for ultrasonic drug and gene delivery. *Adv Drug Deliv Rev, 60*(10), 1137-1152. doi:10.1016/j.addr.2008.03.008

Hwang, J. H., Tu, J., Brayman, A. A., Matula, T. J., & Crum, L. A. (2006). Correlation between inertial cavitation dose and endothelial cell damage in vivo. *Ultrasound Med Biol, 32*(10), 1611-1619. doi:10.1016/j.ultrasmedbio.2006.07.016

Ibsen, S., Benchimol, M., Simberg, D., Schutt, C., Steiner, J., & Esener, S. (2011). A novel nested liposome drug delivery vehicle capable of ultrasound triggered release of its payload. *J Control Release, 155*(3), 358-366. doi:10.1016/j.jconrel.2011.06.032

Izadifar, Z., Babyn, P., & Chapman, D. (2019). Ultrasound cavitation/microbubble detection and medical applications. *Journal of Medical and Biological Engineering, 39*(3), 259-27

Izadifar, Z., Babyn, P., & Chapman, D. (2017). Mechanical and Biological Effects of Ultrasound: A Review of Present Knowledge. *Ultrasound Med Biol, 43*(6), 1085-1104. doi:10.1016/j.ultrasmedbio.2017.01.023

Izadifar, Z., Belev, G., Izadifar, M., Izadifar, Z., & Chapman, D. (2014). Visualization of ultrasound induced cavitation bubbles using the synchrotron x-ray Analyzer Based Imaging technique. *Phys Med Biol, 59*(23), 7541-7555. doi:10.1088/0031-9155/59/23/7541

Kang, J. K., Kim, J. C., Shin, Y., Han, S. M., Won, W. R., Her, J., . . . Oh, K. T. (2020). Principles and applications of nanomaterial-based hyperthermia in cancer therapy. *Arch Pharm Res, 43*(1), 46-57. doi:10.1007/s12272-020-01206-5

Karshafian, R., Samac, S., Bevan, P. D., & Burns, P. N. (2010). Microbubble mediated sonoporation of cells in suspension: clonogenic viability and influence of molecular size on uptake. *Ultrasonics, 50*(7), 691-697. doi:10.1016/j.ultras.2010.01.009

Kiljunen, T., Kangasmaki, A., Aaltonen, A., Kairemo, K., Partanen, K., Joensuu, G., . . . Joensuu, T. (2015). VMAT technique enables concomitant radiotherapy of prostate cancer and pelvic bone metastases. *Acta Oncol, 54*(6), 847-853. doi:10.3109/0284186X.2014.962665

Klap, J., Schmid, M., & Loughlin, K. R. (2015). The relationship between total testosterone levels and prostate cancer: a review of the continuing controversy. *J Urol, 193*(2), 403-413. doi:10.1016/j.juro.2014.07.123

Kopechek, J. A., Park, E. J., Zhang, Y. Z., Vykhodtseva, N. I., McDannold, N. J., & Porter, T. M. (2014). Cavitation-enhanced MR-guided focused ultrasound ablation of rabbit tumors in vivo using phase

shift nanoemulsions. Phys Med Biol, 59(13), 3465-3481. doi:10.1088/0031-9155/59/13/3465

Krasnow, R. E., Rodriguez, D., Nagle, R. T., Mossanen, M., Kibel, A. S., & Chang, S. L. (2018). The impact of age at the time of radiotherapy for localized prostate cancer on the development of second primary malignancies. *Urol Oncol, 36*(11), 500 e511-500 e519. doi:10.1016/j.urolonc.2018.06.007

Kwok, S. J., El Kaffas, A., Lai, P., Al Mahrouki, A., Lee, J., Iradji, S., . . . Czarnota, G. J. (2013). Ultrasound-mediated microbubble enhancement of radiation therapy studied using three-dimensional high-frequency power Doppler ultrasound. *Ultrasound Med Biol, 39*(11), 1983-1990. doi:10.1016/j.ultrasmedbio.2013.03.025

Lai, C. Y., Wu, C. H., Chen, C. C., & Li, P. C. (2006). Quantitative relations of acoustic inertial cavitation with sonoporation and cell viability. *Ultrasound Med Biol, 32*(12), 1931-1941. doi:10.1016/j.ultrasmedbio.2006.06.020

Lane, B. R., Stephenson, A. J., Magi-Galluzzi, C., Lakin, M. M., & Klein, E. A. (2008). Low testosterone and risk of biochemical recurrence and poorly differentiated prostate cancer at radical prostatectomy. *Urology, 72*(6), 1240-1245. doi:10.1016/j.urology.2008.06.001

Li, D., Zhao, L. N., Zheng, X. L., Lin, P., Lin, F., Li, Y., . . . Yu, X. G. (2014). Sox2 is involved in paclitaxel resistance of the prostate cancer cell line PC-3 via the PI3K/Akt pathway. *Mol Med Rep, 10*(6), 3169-3176. doi:10.3892/mmr.2014.2630

Li, J., Ding, Z., Wang, Z., Lu, J. F., Maity, S. N., Navone, N. M., . . . Kim, J. (2011). Androgen regulation of 5alpha-reductase isoenzymes in prostate cancer: implications for prostate cancer prevention. *PLoS One, 6*(12), e28840. doi:10.1371/journal.pone.0028840

Li, J., Mills, G., Huang, M., Lin, S.-H., Logothetis, C., & Kim, J. (2009). *Differential and cell type-dependent transcriptional regulation of SRD5A1, SRD5A2, and SRD5A3 in the androgen receptor pathway in prostate cancer.* Paper presented at the Cancer Res.

Li, T., Chen, H., Khokhlova, T., Wang, Y. N., Kreider, W., He, X., & Hwang, J. H. (2014). Passive cavitation detection during pulsed HIFU exposures of ex vivo tissues and in vivo mouse pancreatic tumors. *Ultrasound Med Biol, 40*(7), 1523-1534. doi:10.1016/j.ultrasmedbio.2014.01.007Li, P., Takahashi, M., & Chiba, K. (2009). Enhanced free-radical generation by shrinking microbubbles using a copper catalyst. *Chemosphere, 77*(8), 1157-1160. doi:10.1016/j.chemosphere.2009.07.062

Lin, Y., Lin, L., Cheng, M., Jin, L., Du, L., Han, T., . . . Qin, P. (2017). Effect of acoustic parameters on the cavitation behavior of SonoVue microbubbles induced by pulsed ultrasound. *Ultrason Sonochem, 35*(Pt A), 176-184. doi:10.1016/j.ultsonch.2016.09.016

Liu, S., & Yamauchi, H. (2008). Different patterns of 5alpha-reductase expression, cellular distribution, and testosterone metabolism in human follicular dermal papilla cells. Biochem Biophys Res Commun, 368(4), 858-864. doi:10.1016/j.bbrc.2008.01.130

Lo, C. W., Desjouy, C., Chen, S. R., Lee, J. L., Inserra, C., Bera, J. C., & Chen, W. S. (2014). Stabilizing in vitro ultrasound-mediated gene transfection by regulating cavitation. *Ultrason Sonochem, 21*(2), 833-839. doi:10.1016/j.ultsonch.2013.10.017

Lonergan, P. E., & Tindall, D. J. (2011). Androgen receptor signaling in prostate cancer development and progression. *J Carcinog, 10*, 20. doi:10.4103/1477-3163.83937

Maeda, K., & Colonius, T. (2019). Bubble cloud dynamics in an ultrasound field. *J Fluid Mech, 862*, 1105-1134. doi:10.1017/jfm.2018.968

Mariappan, Y. K., Glaser, K. J., & Ehman, R. L. (2010). Magnetic resonance elastography: a review. Clin

Anat, 23(5), 497-511. doi:10.1002/ca.21006

Marien, A., Gill, I., Ukimura, O., Betrouni, N., & Villers, A. (2014). Target ablation--image-guided therapy in prostate cancer. *Urol Oncol, 32*(6), 912-923. doi:10.1016/j.urolonc.2013.10.014

Matsui, T., Nuryadi, E., Komatsu, S., Hirota, Y., Shibata, A., Oike, T., & Nakano, T. (2019). Robustness of Clonogenic Assays as a Biomarker for Cancer Cell Radiosensitivity. *Int J Mol Sci, 20*(17). doi:10.3390/ijms20174148

Matula, T. J., Hilmo, P. R., Bailey, M. R., & Crum, L. A. (2002). In vitro sonoluminescence and sonochemistry studies with an electrohydraulic shock-wave lithotripter. *Ultrasound Med Biol, 28*(9), 1199-1207. doi:10.1016/s0301-5629(02)00568-9

Maxwell, A. D., Cain, C. A., Hall, T. L., Fowlkes, J. B., & Xu, Z. (2013). Probability of cavitation for single ultrasound pulses applied to tissues and tissue-mimicking materials. *Ultrasound Med Biol, 39*(3), 449-465. doi:10.1016/j.ultrasmedbio.2012.09.004

McNabb, E., Al-Mahrouki, A., Law, N., McKay, S., Tarapacki, C., Hussein, F., & Czarnota, G. J. (2020). Ultrasound-stimulated microbubble radiation enhancement of tumors: Single-dose and fractionated treatment evaluation. *PLoS One, 15*(9), e0239456. doi:10.1371/journal.pone.0239456

Meehan, K. L., & Sadar, M. D. (2003). Androgens and androgen receptor in prostate and ovarian malignancies. *Front Biosci, 8*, d780-800. doi:10.2741/1063

Michaud, J. E., Billups, K. L., & Partin, A. W. (2015). Testosterone and prostate cancer: an evidence-based review of pathogenesis and oncologic risk. *Ther Adv Urol, 7*(6), 378-387. doi:10.1177/1756287215597633

Miller, D. L., & Dou, C. (2009). Induction of apoptosis in sonoporation and ultrasonic gene transfer. *Ultrasound Med Biol, 35*(1), 144-154. doi:10.1016/j.ultrasmedbio.2008.06.007

Morris, P., Hurrell, A., Shaw, A., Zhang, E., & Beard, P. (2009). A Fabry-Perot fiber-optic ultrasonic hydrophone for the simultaneous measurement of temperature and acoustic pressure. *J Acoust Soc Am, 125*(6), 3611-3622. doi:10.1121/1.3117437

Murray, J., & Tree, A. C. (2019). Prostate cancer - Advantages and disadvantages of MR-guided RT. *Clin Transl Radiat Oncol, 18*, 68-73. doi:10.1016/j.ctro.2019.03.006

Negussie, A. H., Yarmolenko, P. S., Partanen, A., Ranjan, A., Jacobs, G., Woods, D., . . . Dreher, M. R. (2011). Formulation and characterisation of magnetic resonance imageable thermally sensitive liposomes for use with magnetic resonance-guided high intensity focused ultrasound. *Int J Hyperthermia, 27*(2), 140-155. doi:10.3109/02656736.2010.528140

Nightingale, K., Soo, M. S., Nightingale, R., & Trahey, G. (2002). Acoustic radiation force impulse imaging: in vivo demonstration of clinical feasibility. Ultrasound Med Biol, 28(2), 227-235. doi:10.1016/s0301-5629(01)00499-9

Ogata, T., Teshima, T., Inaoka, M., Minami, K., Tsuchiya, T., Isono, M., . . . Matsuura, N. (2011). Carbon ion irradiation suppresses metastatic potential of human non-small cell lung cancer A549 cells through the phosphatidylinositol-3-kinase/Akt signaling pathway. *J Radiat Res, 52*(3), 374-379. doi:10.1269/jrr.10102

Ogata, T., Teshima, T., Kagawa, K., Hishikawa, Y., Takahashi, Y., Kawaguchi, A., . . . Matsuura, N. (2005). Particle irradiation suppresses metastatic potential of cancer cells. *Cancer Res, 65*(1), 113-120. Retrieved from http://www.ncbi.nlm.nih.gov/pubmed/15665286

Peeken, J. C., Vaupel, P., & Combs, S. E. (2017). Integrating Hyperthermia into Modern Radiation Oncology: What Evidence Is Necessary? *Front Oncol, 7*, 132. doi:10.3389/fonc.2017.00132

H. H., Wu, C. H., Kang, S. T., Zhang, J. W., Liu, H. L., Chen, W. S., . . . Yeh, C. K. (2017). Real-time monitoring of inertial cavitation effects of microbubbles by using MRI: In vitro experiments. Magn Reson Med, 77(1), 102-111. doi:10.1002/mrm.26082

Perri, F., Pacelli, R., Della Vittoria Scarpati, G., Cella, L., Giuliano, M., Caponigro, F., & Pepe, S. (2015). Radioresistance in head and neck squamous cell carcinoma: Biological bases and therapeutic implications. *Head Neck, 37*(5), 763-770. doi:10.1002/hed.23837

Petrova, E. V., Brecht, H. P., Motamedi, M., Oraevsky, A. A., & Ermilov, S. A. (2018). In vivo optoacoustic temperature imaging for image-guided cryotherapy of prostate cancer. *Phys Med Biol, 63*(6), 064002. doi:10.1088/1361-6560/aab241

Pignot, G., Maillet, D., Gross, E., Barthelemy, P., Beauval, J. B., Constans-Schlurmann, F., . . . Borchiellini, D. (2018). Systemic treatments for high-risk localized prostate cancer. *Nat Rev Urol, 15*(8), 498-510. doi:10.1038/s41585-018-0017-x

Punnen, S., Cooperberg, M. R., D'Amico, A. V., Karakiewicz, P. I., Moul, J. W., Scher, H. I., . . . Freedland, S. J. (2013). Management of biochemical recurrence after primary treatment of prostate cancer: a systematic review of the literature. *Eur Urol, 64*(6), 905-915. doi:10.1016/j.eururo.2013.05.025

Qin, J., Wang, T. Y., & Willmann, J. K. (2016). Sonoporation: Applications for Cancer Therapy. *Adv Exp Med Biol, 880*, 263-291. doi:10.1007/978-3-319-22536-4_15

Quinn, D. I., Sandler, H. M., Horvath, L. G., Goldkorn, A., & Eastham, J. A. (2017). The evolution of chemotherapy for the treatment of prostate cancer. *Ann Oncol, 28*(11), 2658-2669. doi:10.1093/annonc/mdx348

Rawla, P. (2019). Epidemiology of Prostate Cancer. *World J Oncol, 10*(2), 63-89. doi:10.14740/wjon1191

Rieke, V., & Butts Pauly, K. (2008). MR thermometry. J Magn Reson Imaging, 27(2), 376-390. doi:10.1002/jmri.21265

Robertson, J., & Becker, S. (2018). Influence of Acoustic Reflection on the Inertial Cavitation Dose in a Franz Diffusion Cell. *Ultrasound Med Biol, 44*(5), 1100-1109. doi:10.1016/j.ultrasmedbio.2018.01.021

Salgaonkar, V. A., Datta, S., Holland, C. K., & Mast, T. D. (2009). Passive cavitation imaging with ultrasound arrays. *J Acoust Soc Am, 126*(6), 3071-3083. doi:10.1121/1.3238260

Saliev, T., Feril, L. B., Jr., Nabi, G., & Melzer, A. (2013). Targeted manipulation of apoptotic pathways by using High Intensity Focused Ultrasound in cancer treatment. Cancer Lett, 338(2), 204-208. doi:10.1016/j.canlet.2013.04.016

Salvesen, K. A. (2002). EFSUMB: safety tutorial: epidemiology of diagnostic ultrasound exposure during pregnancy-European committee for medical ultrasound safety (ECMUS). *Eur J Ultrasound, 15*(3), 165-171. doi:10.1016/s0929-8266(02)00038-1

Santos, M. A., Wu, S. K., Li, Z., Goertz, D. E., & Hynynen, K. (2018). Microbubble-assisted MRI-guided focused ultrasound for hyperthermia at reduced power levels. *Int J Hyperthermia, 35*(1), 599-611. doi:10.1080/02656736.2018.1514468

Schade, G. R., Keller, J., Ives, K., Cheng, X., Rosol, T. J., Keller, E., & Roberts, W. W. (2012). Histotripsy focal ablation of implanted prostate tumor in an ACE-1 canine cancer model. *J Urol, 188*(5), 1957-1964. doi:10.1016/j.juro.2012.07.006

Shanei, A., & Shanei, M. M. (2017). Effect of gold nanoparticle size on acoustic cavitation using chemical dosimetry method. *Ultrason Sonochem, 34*, 45-50. doi:10.1016/j.ultsonch.2016.05.010

Shelley, M. D., Kumar, S., Wilt, T., Staffurth, J., Coles, B., & Mason, M. D. (2009). A systematic review

and meta-analysis of randomised trials of neo-adjuvant hormone therapy for localised and locally advanced prostate carcinoma. *Cancer Treat Rev, 35*(1), 9-17. doi:10.1016/j.ctrv.2008.08.002

Somaglino, L., Bouchoux, G., Mestas, J. L., & Lafon, C. (2011). Validation of an acoustic cavitation dose with hydroxyl radical production generated by inertial cavitation in pulsed mode: application to in vitro drug release from liposomes. *Ultrason Sonochem, 18*(2), 577-588. doi:10.1016/j.ultsonch.2010.07.009

Song, W., & Khera, M. (2014). Physiological normal levels of androgen inhibit proliferation of prostate cancer cells in vitro. *Asian J Androl, 16*(6), 864-868. doi:10.4103/1008-682X.129132

Thanou, M., & Gedroyc, W. (2013). MRI-Guided Focused Ultrasound as a New Method of Drug Delivery. *J Drug Deliv, 2013*, 616197. doi:10.1155/2013/616197

Thigpen, A. E., Silver, R. I., Guileyardo, J. M., Casey, M. L., McConnell, J. D., & Russell, D. W. (1993). Tissue distribution and ontogeny of steroid 5 alpha-reductase isozyme expression. *J Clin Invest, 92*(2), 903-910. doi:10.1172/JCI116665

Tinne, N., Schumacher, S., Nuzzo, V., Arnold, C. L., Lubatschowski, H., & Ripken, T. (2010). Interaction dynamics of spatially separated cavitation bubbles in water. *J Biomed Opt, 15*(6), 068003. doi:10.1117/1.3526366

Tung, Y. S., Vlachos, F., Feshitan, J. A., Borden, M. A., & Konofagou, E. E. (2011). The mechanism of interaction between focused ultrasound and microbubbles in blood-brain barrier opening in mice. *J Acoust Soc Am, 130*(5), 3059-3067. doi:10.1121/1.3646905

Uemura, M., Tamura, K., Chung, S., Honma, S., Okuyama, A., Nakamura, Y., & Nakagawa, H. (2008). Novel 5 alpha-steroid reductase (SRD5A3, type-3) is overexpressed in hormone-refractory prostate cancer. *Cancer Sci, 99*(1), 81-86. doi:10.1111/j.1349-7006.2007.00656.x

van den Tempel, N., Laffeber, C., Odijk, H., van Cappellen, W. A., van Rhoon, G. C., Franckena, M., & Kanaar, R. (2017). The effect of thermal dose on hyperthermia-mediated inhibition of DNA repair through homologous recombination. *Oncotarget, 8*(27), 44593-44604. doi:10.18632/oncotarget.17861

van Velthoven, R., Aoun, F., Marcelis, Q., Albisinni, S., Zanaty, M., Lemort, M., . . . Limani, K. (2016). A prospective clinical trial of HIFU hemiablation for clinically localized prostate cancer. *Prostate Cancer Prostatic Dis, 19*(1), 79-83. doi:10.1038/pcan.2015.55

van Wamel, A., Kooiman, K., Harteveld, M., Emmer, M., ten Cate, F. J., Versluis, M., & de Jong, N. (2006). Vibrating microbubbles poking individual cells: drug transfer into cells via sonoporation. *J Control Release, 112*(2), 149-155. doi:10.1016/j.jconrel.2006.02.007

Vappou, J., Bour, P., Marquet, F., Ozenne, V., & Quesson, B. (2018). MR-ARFI-based method for the quantitative measurement of tissue elasticity: application for monitoring HIFU therapy. Phys Med Biol, 63(9), 095018. doi:10.1088/1361-6560/aabd0d

Viallon, M., Terraz, S., Roland, J., Dumont, E., Becker, C. D., & Salomir, R. (2010). Observation and correction of transient cavitation-induced PRFS thermometry artifacts during radiofrequency ablation, using simultaneous ultrasound/MR imaging. Med Phys, 37(4), 1491-1506. doi:10.1118/1.3309439

Villeneuve, L., Alberti, L., Steghens, J. P., Lancelin, J. M., & Mestas, J. L. (2009). Assay of hydroxyl radicals generated by focused ultrasound. *Ultrason Sonochem, 16*(3), 339-344. doi:10.1016/j.ultsonch.2008.09.007

Wang, Y., Bai, W. K., Shen, E., & Hu, B. (2013). Sonoporation by low-frequency and low-power

ultrasound enhances chemotherapeutic efficacy in prostate cancer cells in vitro. *Oncol Lett, 6*(2), 495-498. doi:10.3892/ol.2013.1389

Wei, C., Bai, W. K., Wang, Y., & Hu, B. (2014). Combined treatment of PC-3 cells with ultrasound and microbubbles suppresses invasion and migration. *Oncol Lett, 8*(3), 1372-1376. doi:10.3892/ol.2014.2310

Wiggins, S., & Ottino, J. M. (2004). Foundations of chaotic mixing. *Philos Trans A Math Phys Eng Sci, 362*(1818), 937-970. doi:10.1098/rsta.2003.1356

Wu, S. Y., Tung, Y. S., Marquet, F., Downs, M., Sanchez, C., Chen, C., . . . Konofagou, E. (2014). Transcranial cavitation detection in primates during blood-brain barrier opening--a performance assessment study. *IEEE Trans Ultrason Ferroelectr Freq Control, 61*(6), 966-978. doi:10.1109/TUFFC.2014.2992

Wu, Y., Godoy, A., Azzouni, F., Wilton, J. H., Ip, C., & Mohler, J. L. (2013). Prostate cancer cells differ in testosterone accumulation, dihydrotestosterone conversion, and androgen receptor signaling response to steroid 5alpha-reductase inhibitors. *Prostate, 73*(13), 1470-1482. doi:10.1002/pros.22694

Xie, X., Shao, X., Gao, F., Jin, H., Zhou, J., Du, L., . . . Tang, J. (2011). Effect of hyperthermia on invasion ability and TGF-beta1 expression of breast carcinoma MCF-7 cells. *Oncol Rep, 25*(6), 1573-1579. doi:10.3892/or.2011.1240

Xu, B., Liu, N., Chen, S. Q., Jiang, H., Zhang, L. J., Zhang, X. W., . . . Chen, M. (2016). [Expression of SRD5A1 and its prognostic role in prostate cancer: Analysis based on the data-mining of ONCOMINE]. *Zhonghua Nan Ke Xue, 22*(9), 771-776. Retrieved from http://www.ncbi.nlm.nih.gov/pubmed/29071871

Xu, Z., Owens, G., Gordon, D., Cain, C., & Ludomirsky, A. (2010). Noninvasive creation of an atrial septal defect by histotripsy in a canine model. *Circulation, 121*(6), 742-749. doi:10.1161/CIRCULATIONAHA.109.889071

Yildirim, A., Shi, D., Roy, S., Blum, N. T., Chattaraj, R., Cha, J. N., & Goodwin, A. P. (2018). Nanoparticle-Mediated Acoustic Cavitation Enables High Intensity Focused Ultrasound Ablation Without Tissue Heating. *ACS Appl Mater Interfaces, 10*(43), 36786-36795. doi:10.1021/acsami.8b15368

Young, A. G. H., & Bennewith, K. L. (2017). Ionizing Radiation Enhances Breast Tumor Cell Migration In Vitro. *Radiat Res, 188*(4), 381-391. doi:10.1667/RR14738.1

Yu, F. T., Chen, X., Wang, J., Qin, B., & Villanueva, F. S. (2016). Low Intensity Ultrasound Mediated Liposomal Doxorubicin Delivery Using Polymer Microbubbles. *Mol Pharm, 13*(1), 55-64. doi:10.1021/acs.molpharmaceut.5b00421

Yu, S., Xia, S., Yang, D., Wang, K., Yeh, S., Gao, Z., & Chang, C. (2013). Androgen receptor in human prostate cancer-associated fibroblasts promotes prostate cancer epithelial cell growth and invasion. *Med Oncol, 30*(3), 674. doi:10.1007/s12032-013-0674-9

Zhang, Y., Yong, L., Luo, Y., Ding, X., Xu, D., Gao, X., . . . Zou, J. (2019). Enhancement of HIFU ablation by sonosensitizer-loading liquid fluorocarbon nanoparticles with pre-targeting in a mouse model. *Sci Rep, 9*(1), 6982. doi:10.1038/s41598-019-43416-y

Zhong, W., Sit, W. H., Wan, J. M., & Yu, A. C. (2011). Sonoporation induces apoptosis and cell cycle arrest in human promyelocytic leukemia cells. *Ultrasound Med Biol, 37*(12), 2149-2159. doi:10.1016/j.ultrasmedbio.2011.09.012

References

Zhou, Y., Gu, P., Li, J., Li, F., Zhu, J., Gao, P., . . . Yang, D. (2017). Suppression of STIM1 inhibits the migration and invasion of human prostate cancer cells and is associated with PI3K/Akt signaling inactivation. *Oncol Rep, 38*(5), 2629-2636. doi:10.3892/or.2017.5961

Zhou, Y., Yang, K., Cui, J., Ye, J. Y., & Deng, C. X. (2012). Controlled permeation of cell membrane by single bubble acoustic cavitation. *J Control Release, 157*(1), 103-111. doi:10.1016/j.jconrel.2011.09.068

Zhou, Y., Zhai, L., Simmons, R., & Zhong, P. (2006). Measurement of high intensity focused ultrasound fields by a fiber optic probe hydrophone. *J Acoust Soc Am, 120*(2), 676-685. doi:10.1121/1.2214131

Zhu, L., Altman, M. B., Laszlo, A., Straube, W., Zoberi, I., Hallahan, D. E., & Chen, H. (2019). Ultrasound Hyperthermia Technology for Radiosensitization. *Ultrasound Med Biol, 45*(5), 1025-1043. doi:10.1016/j.ultrasmedbio.2018.12.007

Zhu, W., Wu, X., Yang, B., Yao, X., Cui, X., Xu, P., & Chen, X. (2019). miR-188-5p regulates proliferation and invasion via PI3K/Akt/MMP-2/9 signaling in keloids. *Acta Biochim Biophys Sin (Shanghai), 51*(2), 185-196. doi:10.1093/abbs/gmy165

Zijlstra, A., Janssens, T., Wostyn, K., Versluis, M., Mertens, P. W., & Lohse, D. (2009). High speed imaging of 1 MHz driven microbubbles in contact with a rigid wall. Paper presented at the Solid state phenomena.

Zilonova, E. M., Solovchuk, M., & Sheu, T. W. H. (2019). Simulation of cavitation enhanced temperature elevation in a soft tissue during high-intensity focused ultrasound thermal therapy. *Ultrason Sonochem, 53*, 11-24. doi:10.1016/j.ultsonch.2018.12.006

Zolochevska, O., Xia, X., Williams, B. J., Ramsay, A., Li, S., & Figueiredo, M. L. (2011). Sonoporation delivery of interleukin-27 gene therapy efficiently reduces prostate tumor cell growth in vivo. *Hum Gene Ther, 22*(12), 1537-1550. doi:10.1089/hum.2011

11 Appendix

11.1 Erklärung über die eigenständige Abfassung der Arbeit

Hiermit erkläre ich, dass ich die vorliegende Arbeit selbstständig und ohne unzulässige Hilfe oder Benutzung anderer als der angegebenen Hilfsmittel angefertigt habe. Ich versichere, dass Dritte von mir weder unmittelbar noch mittelbar eine Vergütung oder geldwerte Leistungen für Arbeiten erhalten haben, die im Zusammenhang mit dem Inhalt der vorgelegten Dissertation stehen, und dass die vorgelegte Arbeit weder im Inland noch im Ausland in gleicher oder ähnlicher Form einer anderen Prüfungsbehörde zum Zweck einer Promotion oder eines anderen Prüfungsverfahrens vorgelegt wurde. Alles aus anderen Quellen und von anderen Personen übernommene Material, das in der Arbeit verwendet wurde oder auf das direkt Bezug genommen wird, wurde als solches kenntlich gemacht. Insbesondere wurden alle Personen genannt, die direkt an der Entstehung der vorliegenden Arbeit beteiligt waren. Die aktuellen gesetzlichen Vorgaben in Bezug auf die Zulassung der klinischen Studien, die Bestimmungen des Tierschutzgesetzes, die Bestimmungen des Gentechnikgesetzes und die allgemeinen Datenschutzbestimmungen wurden eingehalten. Ich versichere, dass ich die Regelungen der Satzung der Universität Leipzig zur Sicherung guter wissenschaftlicher Praxis kenne und eingehalten habe.

.....	.....
Datum	Unterschrift

11.2 List of figures

11.3 List of tables

11.4 Curriculum vitae

Personal Information

Name: Shaonan Hu

Date of Birth: January 1st, 1988

Place of Birth: City of Yuncheng, Shanxi Province, P. R. China.

Nationality: Chinese

Language: Chinese, English.

Educational Background

➢ **Primary/Secondary school**

- 1994.09 – 1999.07 (primary school): West Street Experimental Primary School of Xinjiang County, Yuncheng City, Shanxi Province, China.
- 1999.09 – 2002.07 (junior secondary school): Chengzhen Middle School of Xinjiang County, Yuncheng City, Shanxi Province, China.
- 2002.09 – 2007.07 (senior secondary school): XinJiang Middle School, Yuncheng City, Shanxi Province, China.

➢ **University**

- 2007.09 – 2011.07 (bachelor study): Pharmaceutical Engineering, Chongqing University of Technology, Chongqing City, Chongqing Municipality, P. R. China.
- 2011.09 – 2014.07 (master study): Microbial and Biochemical Pharmacy, Chongqing University of Technology, Chongqing City, Chongqing Municipality, P. R. China.
- 2016.11 – 2019.07 (doctor study): Innovation Center Computer Assisted Surgery (ICCAS), Medical Faculty, University of Leipzig, Germany.

Publications

1. **Hu S,** Zhang X, Unger M, Patties I, Melzer A, Landgraf L (2020). Focused Ultrasound-Induced Cavitation Sensitizes Cancer Cells to Radiation Therapy and Hyperthermia. *Cells,* 9(12). doi:10.3390/cells9122595. (IF: 4.366)

   Contribution: methodology, experiment, formal analysis, investigation and data curation. The publication is part of this dissertation.

2. Ning W, Jiang X, Sun Z, Ogbuehi A, Gu W, Acharya A, Fang Z, Zhu X, Ou Q, Zeng M, Li C, Hua S, Mujagond P, Liu X, Deng Y, Pan H, **Hu S,** Hu X, Li S (2021). Identification of the Potential Biomarkers Involved in the Human Oral Mucosal Wound Healing: A Bioinformatic Study. *BioMed Research International,* Volume 2021, Article ID 6695245, https://doi.org/10.1155/2021/6695245. (IF: 2.276)

   Contribution: experimental design. The publication is not part of this dissertation.

3. Ning W, Li S, Tsering J, Ma Y, Li H, Ma Y, Ogbuehi A, Pan H, Li H, **Hu S,** Liu X, Deng Y, Zhang J, Hu X (2021). Protective Effect of Triphala against Oxidative Stress-Induced Neurotoxicity. *BioMed*

Research International, Volume 2021, Article ID 6674988, https://doi.org/10.1155/2021/6674988. (IF: 2.276)

Contribution: methodology. The publication is not part of this dissertation.

Presentations

- **Oral presentations**

- **Hu S,** Landgraf L, Unger M, Melzer A. Alternative treatment of prostate cancer: new strategies using focused ultrasound. Further Med Technologies (FMT) 2019, 18.06.2019, Leipzig, Germany.

- **Poster presentations**

- **Hu S,** Zhang X, Xu D, Landgraf L, Melzer A. Comparison of Thermal and Cavitation Effects of Ultrasound Treatment of Prostate Cancer. Research Festival of Life Science 2018, 19.01.2018, Leipzig, Germany.
- **Hu S,** Landgraf L, Unger M, Melzer A. Alternative treatment of prostate cancer: new strategies using focused ultrasound. Research Festival of Life Science 2019, 18.01.2019, Leipzig, Germany.
- **Hu S,** Landgraf L, Unger M, Melzer A. Alternative treatment of prostate cancer: new strategies using focused ultrasound. 53rd Conference of the German Society for Biomedical Engineering (BMT) 2019, 25.09.2019, Frankfurt/Main, Germany.
- **Hu S,** Unger M, Landgraf L, Melzer A. *In vitro* effects of cavitation induced by focused ultrasound in prostate cancer cells. Research Festival of Life Science 2020, 30.01.2020, Leipzig, Germany.

11.5 Acknowledgments

"A journey of a thousand mile they say begins with a footstep". To everyone who made this journey worthwhile, I would like to extend my heartfelt thanks to you all; without your assistance, this accomplishment would have been impossible.

First and foremost, I would like to avail myself the opportunity to express my gratitude to Prof. Dr. Andreas Melzer, my supervisor, who gave me the opportunity to work on this interesting and meaningful topic. I wish to thank him for taking the time out of his busy schedule to participate in every work-report meeting with me and for giving me such much-needed guidance. Every advice, instruction, and directive from him were instrumental to the success of this thesis.

Appendix

My heartfelt gratitude goes to Dr. Landgraf Lisa, my group leader, who led me into the world of biomedicine and walked me through all the stages of my Ph.D. career. I remember her patience with me, as she guided me through those rigorous experiments. I salute her for her professionalism and for the way and manner she corrected every mistake in my dissertation, as I was writing.

I cannot thank my wife enough, for her outstanding support throughout this process. I am greatly indebted to you my beloved wife, Xinrui Zhang. As my colleague in the same research group, and my wife, you supported me at work and at home, by always urging me to remain focused and never be distracted. Your encouragement is a great source of motivation for me to finish my Ph.D. I will continue to be grateful for the balance you brought into my life and my work. I am sure for us both, it will not only be about marriage, but it will also be about working together to make outstanding contributions to the scientific community in the future.

My deepest gratitude goes to my beloved family for their loving considerations and great confidence in me all through these years. Not forgetting my colleagues and friends, thank you all immensely for your support. I owe my sincere gratitude to Dr. Michael Unger and Dr. Ina Patties, who gave me support in ultrasound software and the operation of radiation therapy, respectively.

A special thanks to Chenghan Xie, Jingxia Wang, Junjie Wan, Minghui Cong, Hanluo Li, and Simin Li, I am proud and lucky to associate and to have you all as friends. Our journey together as friends in Germany and the friendship we have built together will forever be cherished. Thanks for the memories, you shared the good times and the bad times with me. Your encouragement and help in every problematic situation, and the happy laughter and cheerful voices at every of our gathering or conversations, will remain eternal.

Finally, I would like to specially thank the Chinese Government Scholarship (CSC) and SONO-RAY project from the Federal Ministry of Education and Research, who gave me the funding for my living cost during my Ph.D. study period and funding for scientific research, respectively. From the deepest part of my heart, I say a very big thank you to you all.

As I mark the end of this chapter, it is the beginning of the next and the first page of that next chapter will begin with gratitude, for all my life has been blessed with by you all.